Design, realization, and characterization of optical negative index metamaterials

Dissertation

zur Erlangung des akademischen Grades

doctor rerum naturalium (Dr. rer. nat.)

vorgelegt dem Rat der Physikalisch-Astronomischen Fakultät

der Friedrich-Schiller-Universität Jena

von Ms. Sc. Ekaterina Pshenay-Severin

geboren am 18.02.1981 in Leningrad.

Gutachter:

1. Prof. Dr. Thomas Pertsch, Friedrich-Schiller-Universität Jena

2. Prof. Dr. Ulf Peschel, Friedrich-Alexander-Universität Erlangen-Nürnberg

3. Prof. Dr. Vladimir M. Shalaev, Purdue University, USA

Tag der Disputation: 13.12.2011

Contents

Chapter 1

Introduction

1.1 Optical Metamaterials

Optical properties of natural materials are determined mainly by their atomic or molecular structure. In the classical electrodynamics the interaction of the electromagnetic (EM) radiation with a homogeneous material is described in terms of macroscopic material parameters, electric permittivity ϵ and magnetic permeability μ. These parameters can be introduced for a homogeneous material by averaging the responses of single atoms or molecules to the EM radiation over a finite volume with a size much smaller than the wavelength of light but still containing a large number of atoms or molecules.

To realize new materials with optical properties not available with natural materials, one of the possible ways is based on the structuring of materials on subwavelength dimensions forming new constitutive elements. These constitutive elements created from natural materials by combining and shaping them in a spatial way, while keeping their sizes smaller than the wavelength of EM radiation, can be considered as metaatoms or metamolecules. As a result, a metamaterial (MM) composed of metaatoms or metamolecules with dimensions much smaller than the wavelength of EM radiation can be treated as an effectively homogeneous material. The optical properties of MMs, in turn, can be described with ϵ_{eff} and μ_{eff} determined now by the EM response of the metaatoms and metamolecules. In the literature concerning MMs, the notation "metaatoms" became well established to define artificial inclusions of arbitrary complex shapes. Hereafter, for the sake of consistency, the notation "metaatom" is used to define the unit cell of a MM regardless of its complexity.

The approach based on the engineering of the EM response of metaatoms allows for the realization of metamaterials with extraordinary EM properties. One of

those is the optical magnetism. It is well known, that the magnetic permeability of naturally occurring materials is close to unity at optical frequencies. The dielectric function, in contrast, varies significantly for different materials.

Long before magnetic optical materials became a reality, theoretical considerations of the light propagation in such a medium were undertaken. The modern electromagnetic theory of media with simultaneously negative ϵ and μ was developed in 1968 by V. Veselago [1]. It should be noticed, however, that the first works on this issue are dated to the begining of the 20th century [2–4]. In the work of V. Veselago [1], it was shown that in a medium with $\epsilon < 0$ and $\mu < 0$ the phase velocity is negative, which means its direction is opposite to the direction of the energy flow determined by the pointing vector. As a result, the refractive index n attributed to this material is negative. Almost all phenomena related to light propagation in such materials have realizations different to those in materials with positive n. For example, the Doppler shift is reversed in such media and the Cherenkov radiation emitted from a charge passing through a material with $n < 0$ is emitted in the opposite direction to the charge's motion [1]. However, probably the most attractive feature of negative index materials (NIMs) for applications is the negative refraction.

Almost four decades separate the theoretical work of V. Veselago and the first realization of MMs with a negative effective refractive index. The starting point in the development of contemporary MMs was the work of J. Pendry published in 1999 [5], where an artificial medium possessing magnetic response was proposed. In Ref. [5] it was shown that a MM composed of nonmagnetic thin sheets of metal rolled in cylinders has a response to the microwave radiation as if it possesses an effective magnetic permeability. Furthermore, the planar split-ring resonators (SRRs) introduced likewise in Ref. [5] became the most prominent magnetic metaatom for MMs in the microwave range. A SRR is a metallic ring with a gap and can be understood as an L - C circuit. In the spectral ranges below and above the resonance frequency of the equivalent L - C circuit the SRR demonstrates para- and diamagnetic response, respectively. The first NIM in the microwave range was based on SRRs and metallic wires providing negative μ_{eff} and ϵ_{eff}, respectively [6]. Experimentally, a negative index of a MM composed of SRRs and metallic wires [7] was demonstrated by the registration of negative refraction on a wedge made of this material [8].

After the first NIMs were experimentally realized the field of MMs developed rapidly. Principally new devices based on NIMs were proposed, among those the perfect lens and the cloaking device. The perfect lens proposed by J. Pendry [9] allows for imaging with subwavelength resolution, due to the support of the evanescent fields by NIMs. After the limitations of the device were clarified [10, 11], the perfect lens was demonstrated first numerically [12] and finally experimentally [13].

At microwave frequencies, using a lens made of a NIM, imaging with a resolution better than 0.235λ was achieved. Later, the invisibility cloaking based on the engineering of ϵ and μ was proposed [14, 15] and experimentally realized for microwave frequencies [16].

After the demonstration of the perfect lens effect in the microwave range massive efforts were devoted to realize NIMs in the optical spectral range, where they promise a breakthrough for imaging devices. Here, for the sake of conciseness, with the notation optical spectral range the VIS and NIR spectral domains are meant.

The work on this thesis began in 2005, at the time when pioneering works on optical MMs had been conducted. At that time, to realize NIMs at the optical frequencies the strategy of the straight scaling of the structures developed for microwave frequencies was pursued. However, very soon the limitations of this approach became obvious.

Firstly, to satisfy the condition of an effective medium at high operation frequencies, the size of the metaatoms had to be reduced to the scale of several hundreds of nanometers. As the fabrication of MMs composed of such metaatoms became a challenging technological problem, the design of the metatoms had to be simplified to correspond to the state-of-the-art technology. It should be noticed that only a few groups in the world had technological facilities for NIM fabrication at that time.

Secondly, a fundamental difference between optical and microwave MMs was recognized. At optical frequencies the metals used to construct the magnetic atoms can not be considered as perfect conductors as the ratio between the real and imaginary parts of their dielectric functions drops dramatically. As a result, the magnetic response of a SRR experiences resonance frequency saturation with decreasing its dimensions [17–20]. Furthermore, in the optical domain the interaction of the EM radiation with nanostructured metallic inclusions is determined by the physics of localized surface plasmon polaritons. Thus, the development of an appropriate physical model providing the theoretical description of metaatoms was required. It should be emphasized, that until now the final theory has not yet been developed.

To realize NIMs in the optical range, alternative geometries accounting for the new physical conditions and the limitations imposed by the technology were developed. A double cut-wire structure became a prominent magnetic metaatom for the optical spectral range [21–24]. This magnetic metaatom consists of two metallic nanowires separated by a dielectric. The excitation of the antiparallel effective currents in the metallic wires provided the magnetic response of the system. In 2005 and 2006 so-called fishnet NIMs, where cut-wires and continuous wires are merged in one element, were realized in the NIR [25, 26]. Later, a low-loss NIM based on silver for the telecommunication wavelength was demonstrated [27].

Over a period of several years, the major efforts were focused on the development of the technological facilities to push the operation frequency of NIMs from the NIR to the VIS spectral range [28, 29]. Further, due to technological progress the realization of "bulk" metamaterials consisting of several metaatomic layers became possible [30–32]. However, due to the high absorption even in a single metaatomic layer the transparency of a NIM consisting of several layers drops dramatically with increasing their number. Hence, the majority of the experimentally realized NIMs still consist of a single metaatomic layer. This makes the experimental characterization of the optical properties of such NIMs a challenging task. It should be noticed that there are only a few works addressing direct experimental characterization of the effective optical parameters of MMs [25, 26, 29, 33]. Though these experiments successfully demonstrated the negative refractive index of MMs, they can be hardly used as a routine technique.

After the concept of metamaterials based on metaatoms was experimentally established in the optical range, a revision of their theoretical description became unavoidable. Initially, the material properties of MMs were described with effective electric permittivity ϵ_{eff} and effective magnetic permeability μ_{eff}, as well as an effective refractive index n_{eff} and impedance z_{eff}, assuming the validity of their introduction for the MMs in the same manner as for natural optical materials. However, due to technological reasons and the plasmonic origin of the effects in metaatoms, the sizes of metaatoms turned out to be only a few times smaller than the wavelength of light. In this regime the EM response of MMs becomes nonlocal and, as a result, the effective permittivity and permeability of MMs depend on the wavevector $\boldsymbol{k}$ [34–36]. The recognition of the fact that spatial dispersion is an inherent property of metamaterials provoked wider debates about the validity of the introduction of the effective material parameters for MMs [37–43]. It should be noticed that until now the final approach to describe EM properties of optical MMs has not yet been developed. In the experiments, however, this problem could be tolerated until now, because only metaatoms with simple geometries could be realized providing the desired EM response solely for normal incidence. Accordingly, experimentally available optical MMs are commonly described with effective ϵ_{eff} and μ_{eff}, valid only for normal incidence.

Besides the lacking theoretical description of NIMs, the main limitation of contemporary NIMs lies in the high rate of losses, which are caused by the absorption of gold and silver commonly used as materials for metaatoms. Nowadays, one of the promising approaches to overcome this drawback is the compensation of the losses by implementation of gain materials [44, 45]. Moreover, research is ongoing to find plasmonic materials with low losses which could replace the metals [46] in the

metaatoms.

1.2 Motivation and scope of this thesis

This thesis is devoted to the design, experimental realization, and characterization of NIMs in the optical domain. When the work on this thesis was started the realization of NIMs for the optical range was a challenging technological task. Hence, in the beginning the establishment of the technological process based on electron-beam lithography and the development of realizable designs of metaatoms were in the focus of the research. The prime aim was the elaboration of guidelines for the design of NIMs based on double cut-wires and continuous wires accounting for limitations of the accessible fabrication technology. Though a negative refractive index of double element NIMs had been demonstrated in the THz and microwave regions [47–50], the challenge was to design and realize them in the optical range.

Alongside the progress in the realization of NIMs the development of a routine experimental method for the characterization of their optical properties became urgent. Though a few experimental methods [25, 26, 29, 33] were developed to demonstrate a negative refractive index, they either required a certain configuration of the samples [25] or had limitations regarding the width of the accessible spectral range [26, 29, 33]. Therefore, the second aim of the work was the development of an experimental interferometric setup providing a routine technique for the measurements of MM optical properties in a broad spectral range.

The progress of fabrication techniques enabled the realization of metaatoms with advanced geometries and, thus, opened new possibilities to engineer their EM response. The asymmetry of the metaatoms was recognized as a powerful tool to design their EM properties. Numerous numerical and experimental investigations on the tailoring of the magnetic properties of MMs by breaking the symmetry of their constitutive elements have been undertaken in the microwave [51–54] and optical [55–57] frequency ranges. Different types of structures, in particular split ring resonators [52–55, 58] and double cut-wire structures [51] were investigated. Experiments on different configurations and combinations of these elements have shown that breaking the symmetry of the structures enables tuning of their EM response in a broad range and provides access to additional modes. Nevertheless, there was a lack of simple theoretical models providing qualitative understanding of the mechanisms behind the observed effects and, that is important, enabling to predict them. To fill this gap, an expansion of the theoretical multipole model presented in Ref. [59] for the case of asymmetric double cut-wire structures was undertaken in this thesis. The extended model was employed to investigate the magnetic response of double

cut-wire structures with broken symmetry.

It should be noticed that in the present work the EM properties of MMs were investigated only for the case of normal incidence.

This thesis is structured as follows. In chapter 2 the fundamental concept of NIMs composed of plasmonic metaatoms is presented. After a brief introduction of the condition for a negative refractive index the concept of magnetic metaatoms based on plasmonic nanostructures is discussed. The basics of plasmonics, essential for the understanding of the functionality of metaatoms, are considered in the second section of the chapter. Further, the problem of the introduction of effective material parameters for MMs is discussed and the multipole approach [60] used to introduce the effective parameters is presented. At the end of the chapter a computational method used for numerical studies of metamaterials is briefly introduced.

Chapter 3 is devoted to the design and the realization of NIMs based on double cut-wires and continuous wires. In this chapter the engineering of the EM response of a cut-wire structure by tuning its geometry is investigated. It is shown how ϵ_{eff} and μ_{eff} of a MM can be designed employing the plasmon polariton resonances supported by the cut-wires. Further, the main steps and limitations of the used technological process are presented and its influence on the design of NIMs is considered. The chapter is closed with the demonstration of a double element NIM at $\lambda = 2.1\ \mu\mathrm{m}$.

In chapter 4 the experimental method developed for the characterization of the optical properties of MMs is presented. In the beginning of the chapter the theoretical background of the white-light spectral interferometry and the realized experimental setup are introduced. Further, the evaluation of the developed experimental method and a method based on the combination of the simulated and the experimental data, commonly used to determine the refractive index of MMs, are conducted. The accuracies of the two methods are compared considering a simple plasmonic structure and a fishnet NIM.

In chapter 5 the investigations of the magnetic properties of asymmetric double cut-wires are presented. The magnetic response of the asymmetric cut-wires, controlled by the variation of the length of the wires, was studied experimentally and theoretically using numerical simulations and the multipole model [59]. In the first section of the chapter, the extension of the multipole model [59] towards the case of asymmetric cut-wires is introduced. Further, using the extended multipole model the dynamics of the currents in the system, giving rise to the magnetic moment, is analyzed. Using the results of this analysis, the dependence of the magnetic moment on the asymmetry of the structures could be explained. The chapter is closed with experimental investigations of asymmetric cut-wire structures.

Some further remarks should be made regarding the general conventions accepted

in this thesis. As it has been mentioned above, for the sake of conciseness, the notation optical range will be used for the spectral range from VIS to NIR (wavelength from $0.5\,\mu m$ to $3\,\mu m$). Spectral information will be presented in wavelengths λ or, in the cases when the energy representation of the spectral data is important, in wavenumbers $\tilde{\nu} = 1/\lambda$. The wavenumber representation was preferred in most figures to facilitate the easy conversion to the wavelength domain. The circular frequencies $\omega = 2\pi c/\lambda$, however, are kept in the analytical calculations.

The present work is the result of a close collaboration with Dr. Uwe Hübner from the Institute of Photonic Technology Jena who performed the fabrication of almost all samples used in this work. The investigations of technological aspects of electron-beam lithography and thin films evaporation processes required for MM's fabrication belong to the scope of this own scientific research. My personal contribution to the establishment of the technological process was made by designing MM samples, performing optical characterization of fabricated structures and providing analysis of their optical properties.

I also appreciate the contribution of Matthias Falkner in the development of the experimental setup for phase measurements, which he made during his Diploma thesis under my supervision.

Chapter 2

Fundamental concepts and basic methods

In the first section of this chapter the condition for a negative refraction index material will be introduced according to the works of V.G. Veselago and R. Depine [1,61]. MMs with ϵ_{eff} and μ_{eff} satisfying the condition of a negative index material can be realized following the concept of artificial effective media composed of metaatoms with subwavelength dimensions. Up to now, the majority of metaatom designs providing a magnetic response of MMs employ the excitation of localized or surface plasmon polaritons in metallic nanostructures [62]. Hence, in the second section of the chapter the basics of plasmonics essential for the understanding of the concept and functionality of metaatoms are introduced. Additionally, the issue of the dielectric function of metals in the case of nanoparticles is discussed.

Further, in Sec. 2.3 the problem of the introduction of effective material parameters for the MMs is considered. Though the development of a theory for the description of optical properties of MMs is beyond the scope of this thesis, the concept of effective parameters, essential for experimental studies, is presented in this chapter. The effective material parameters of MMs in the present thesis are introduced according to the multipole model proposed by A. Chipouline and published in the work of J. Petschulat, C. Menzel, and A. Chipouline [59]. The concept of the multipole approach presented in Ref. [59] and in the thesis of J. Petschulat [60] is summarized in Sec. 2.3.

The chapter is closed with a brief introduction of a computational method used for numerical studies of metamaterials.

2.1 The condition for a negative index material

Theoretical investigations on hypothetic homogeneous media possessing a negative electric permittivity ϵ and permeability μ [1] have shown that the phase velocity of light in such media given by the wave vector $\boldsymbol{k}$ is directed opposite to the energy flow given by the Poynting vector $\boldsymbol{S}$

$$\boldsymbol{S} = \boldsymbol{E} \times \boldsymbol{H}. \tag{2.1}$$

Indeed, considering Maxwell's equations in frequency space for plane waves in a homogeneous medium

$$\boldsymbol{k} \times \boldsymbol{E} = \omega \mu \mu_0 \boldsymbol{H}, \tag{2.2}$$

$$\boldsymbol{k} \times \boldsymbol{H} = -\omega \epsilon \epsilon_0 \boldsymbol{E} \tag{2.3}$$

one can see that the simultaneous change of the sign of ϵ and μ leads to the transformation of the right handed triplet formed by $\boldsymbol{k}$, $\boldsymbol{E}$, and $\boldsymbol{H}$ to a left handed one. Since the vectors $\boldsymbol{E}$, $\boldsymbol{H}$, and $\boldsymbol{S}$ always form a right handed triplet this means that if $\epsilon < 0$ and $\mu < 0$ then $\boldsymbol{k}$ is directed opposite to $\boldsymbol{S}$. Introducing the refractive index n, as $\boldsymbol{k} = n\boldsymbol{k_0}$, where $\boldsymbol{k_0}$ is the wave vector in vacuum, materials with a negative phase velocity can be characterized with a negative refractive index. In a negative index material a number of fundamental electromagnetic phenomena such as light refraction, reflection, and transmission expressed with the Snell's law and Fresnel formulas, Doppler effect and Fermat principle are realized in an uncommon way [1]. Probably the most attractive application of a negative index material, which initially forced the rapid development of the field, was the super lens, enabling imaging with subwavelength resolution [9, 63].

A generalized condition for a medium with negative phase velocity was introduced in Ref. [61]. Assuming a dissipative electric permittivity $\epsilon = \epsilon' + i\epsilon'' = |\epsilon| \exp[i\phi_\epsilon]$ and permeability $\mu = \mu' + i\mu'' = |\mu| \exp[i\phi_\mu]$ the refractive index can be written as $n = \pm\sqrt{\epsilon\mu} = \sqrt{|\epsilon||\mu|} \exp[i(\phi_\epsilon + \phi_\mu)/2]$. Obviously, the real part of the refractive index n' is negative if $\pi \leq (\phi_\epsilon + \phi_\mu)/2 < \pi/2$. Thus, the double-negative condition $\epsilon' < 0$, $\mu' < 0$ is sufficient but not necessary to achieve a negative refractive index. Necessary is, that at least one of ϵ and μ has a negative real part ($\pi \leq \phi_{\epsilon/\mu} < \pi/2$) and the other has nonzero imaginary part ($\pi \leq \phi_{\mu/\epsilon} < 0$). Negative index materials with simultaneously negative ϵ' and μ' are usually called double-negative materials. Accordingly, single-negative materials have either negative ϵ' or negative μ'. According to Ref. [61] the condition of a negative index material can be written

as

$$|\mu|\epsilon' + |\epsilon|\mu' < 0. \tag{2.4}$$

To evaluate the efficiency of a negative index material the figure of merit (FOM) is commonly introduced as the relation of the real to the imaginary part of the refractive index of a NIM

$$\text{FOM} = \left|\frac{n'}{n''}\right| = \frac{|\mu|\epsilon' + |\epsilon|\mu'}{|\mu|\epsilon'' + |\epsilon|\mu''}. \tag{2.5}$$

From Eq. (2.5) it follows that a double-negative material with a real part of the refractive index n' will have a higher FOM than a single-negative material with the same n'. Indeed, using $\epsilon = |\epsilon|\exp[i\phi_\epsilon]$ and $\mu = |\mu|\exp[i\phi_\mu]$, FOM and n'' can be expressed as

$$\text{FOM} = |\cot\left[(\phi_\epsilon + \phi_\mu)/2\right]| = |\cot\phi_{\text{i}}|, \tag{2.6}$$

$$n'' = \frac{n'}{\cot\left[(\phi_\epsilon + \phi_\mu)/2\right]} = \frac{n'}{\cot\phi_{\text{i}}}. \tag{2.7}$$

The argument of the cotangent function for a double-negative material ($\phi_{\text{i}} = \phi_{\text{DN}}$) lies between $\pi/2$ and π and its absolute value is larger than the one for a single-negative material $\phi_{\text{i}} = \phi_{\text{SN}}$. Thus, as expected, $n''_{\text{DN}} < n''_{\text{SN}}$ and the FOM for a double-negative material is larger than the FOM of a single-negative material.

In short, in an isotropic, homogeneous material the phase velocity of light is directed opposite to the power flow, if the material parameters ϵ and μ satisfy the condition expressed with Eq. (2.4). The refractive index of such a material is negative.

2.2 Metaatoms based on plasmonic nanostructures

In the optical spectral range the common approach to create a NIM is based on the combination of two elements in its unit cell. Using a noble metal in the unit cell of a MM a negative real part of the effective permittivity $\epsilon'_{\text{eff}}(\omega) < 0$ of the MM can be easily achieved. The realization of the required $\mu_{\text{eff}}(\omega)$, in turn, is connected with the creation of a metaatom providing the desired magnetic response. The vast majority of metaatom designs providing a magnetic response to NIMs utilize the localized or surface plasmon polaritons supported by the metallic nanostructures [62].

2.2.1 Localized plasmon polaritons

Localized plasmon polaritons are non-propagating excitations of the conducting electrons in metallic nanostructures coupled to the electromagnetic field [64]. In a metallic nanoparticle, electrons driven by the electric field shift as a whole relative to the positively charged host. As a result, a restoring force occurs and a resonance can arise. This resonance is called localized surface plasmon resonance or in short: plasmon resonance.

Analytical expressions for the polarizability of a nanoparticle can be derived in the quasi-static approximation [65] for particles of simple forms only, i.e. spheres or ellipsoids. Nevertheless, the analysis of the polarizabilities of spherical and elliptical particles provide inside into the dynamics of metaatoms, even if they have a more complex form.

For a sub-wavelength metallic particle of ellipsoidal form with the semiaxes a_1, a_2, and a_3, whose surface is given as

$$\frac{x^2}{a_1^2} + \frac{y^2}{a_2^2} + \frac{z^2}{a_3^2} = 1 \tag{2.8}$$

the polarizabilities α_i along the principal axes ($i = 1, 2, 3$) according to Ref. [66] are

$$\alpha_i = 4\pi a_1 a_2 a_3 \frac{\epsilon(\omega) - \epsilon_h}{3\epsilon_h + 3L_i\left[\epsilon(\omega) - \epsilon_h\right]}, \tag{2.9}$$

where the permittivity of the material of the particle is $\epsilon(\omega)$ and the permittivity of the host medium is ϵ_h. L_i is a geometrical factor given by

$$L_i = \frac{a_1 a_2 a_3}{2} \int_0^\infty \frac{dq}{\left(a_i^2 + q\right)\sqrt{\left(q + a_1^2\right)\left(q + a_2^2\right)\left(q + a_3^2\right)}}. \tag{2.10}$$

For a spherical particle of the radius a the geometrical factor is $L = \frac{1}{3}$ and the polarizability is

$$\alpha_{\text{sphere}} = 4\pi a^3 \frac{\epsilon(\omega) - \epsilon_h}{2\epsilon_h + \epsilon(\omega)}. \tag{2.11}$$

In this case, the condition for an extremum of the polarizability is a minimum of the denominator $2\epsilon_h + \epsilon(\omega)$. In a non absorbing host medium this gives the condition

$$Re[\epsilon(\omega)] = -2\epsilon_h. \tag{2.12}$$

Thus, the position of the plasmon resonance can be controlled by changing the material parameter of the host medium or the particle. Furthermore, deviations of

the particle shape from a sphere cause a shift of the resonance frequencies, according to Eq. (2.9). Thus, for a gold nanowire which can be approximated with a prolate spheroid with $a_1 = a_2 \ll a_3$ tuning of the resonance frequency from the VIS to the NIR region is possible by changing its geometry and the host medium.

2.2.2 Hybridization scheme for complex plasmonic systems

Metallic nano-particles support localized surface plasmons, whose excitation results in the resonant increase of the polarizability of the particles. A complex response including the rise of a magnetic moment can be achieved by shaping and/or by grouping nanoparticles into complex geometries. Insight into the behaviour of complex nanostuctures is provided by a hybridization model proposed in Ref. [67]. The model is in a sense an analog of molecular orbital theory and describes interaction of elementary plasmonic elements forming a complex structure. Developed for metallic dimers [67, 68] and nanoshells [69], the model was employed for the description of various complex nanostructures used as a constitutive elements of MMs [62, 70–74].

Using the hybridization scheme the origin of the magnetic response of the double cut-wire structure (Fig. 2.1(a)), which consists of two metallic wires separated by a spacer, can be explained as follows. Each wire supports a plasmon mode with the eigenfrequency ω_0. A system of two wires possesses two eigenmodes of different symmetry, whose frequencies are degenerate if the distance between them is large enough to prevent any interaction between the wires. In a system of two closely spaced cut-wires the interaction between the plasmons of each wire lifts the degeneracy of the eigenmodes. The mode with a spatially symmetric field distribution, hereafter called symmetric mode, has a higher eigenfrequency $\omega_{0,+}$ than the anti-symmetric mode with antisymmetric field distribution and the eigenfrequency $\omega_{0,-}$ (see the hybridization diagram in Fig. 2.1(a)). The eigenfrequency splitting in a system of two cut-wires can be observed in the transmittance spectra of a layer of such cut-wires where two minima correspond to the excitation of the symmetric (2) and antisymmetric (3) modes (see Fig. 2.1(b) blue line). In contrast, the spectrum of a layer of single cut-wires shown in Fig. 2.1(b) with a red line has only one minimum (1).

The spatial distributions of the electric and magnetic fields at the frequencies of the symmetric and antisymmetric resonances for a gold double cut-wire structure infinite in one direction and with a length of 300 nm, a thickness of 10 nm, and a separation distance of 40 nm are shown in Fig. 2.1(c)-(f). In the symmetric resonance the electric field distribution (see Fig. 2.1(c)) corresponds to two dipoles oscillating in phase. Thus, the symmetric mode is associated with a strong dipole moment,
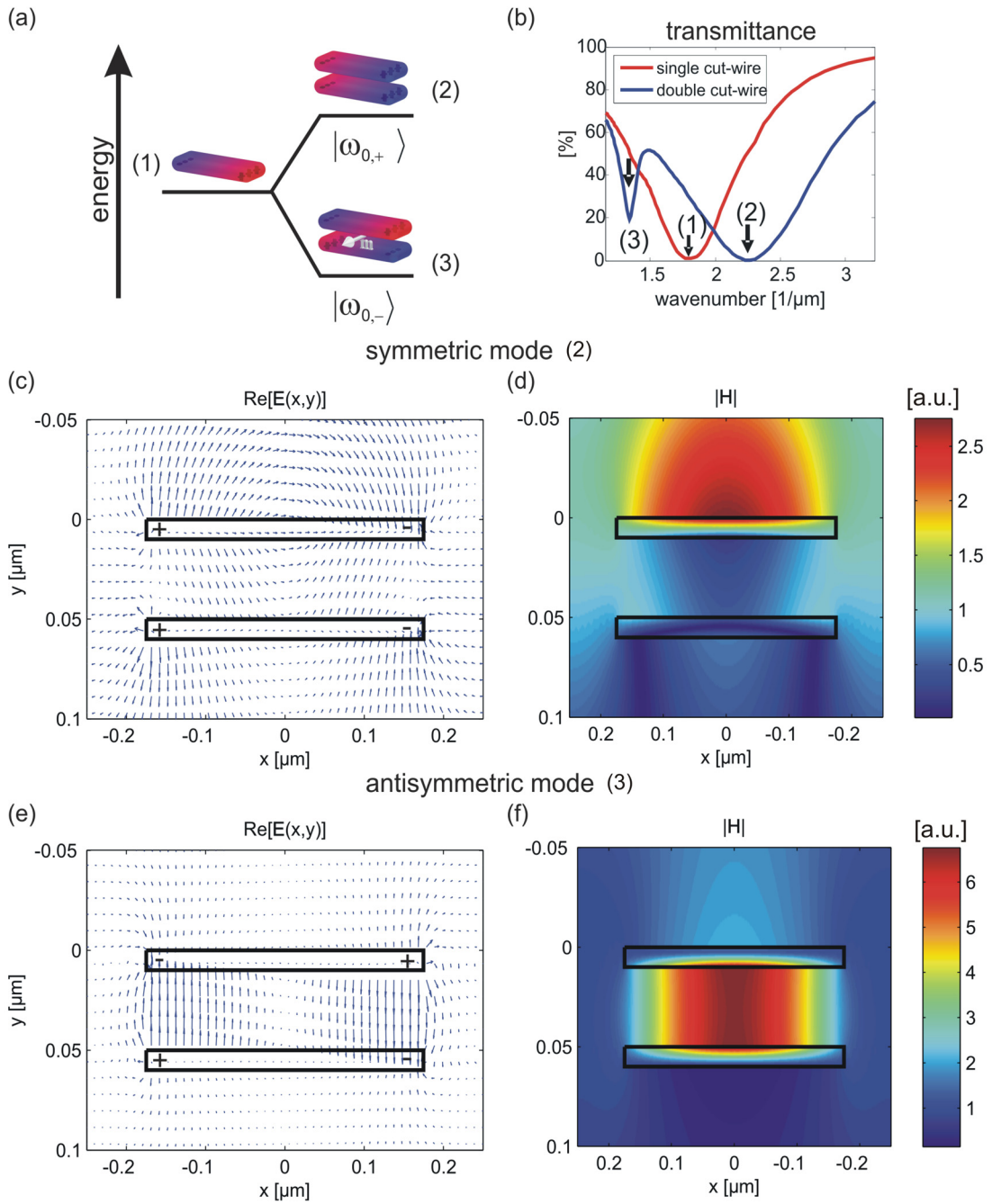
Figure 2.1: (a) - Transmittance of single (red curve) and double (blue curve) cut-wire structures. (b) - Eigenfrequency splitting diagram for a double cut-wire structure. (c), (e) and (d), (f) - electric and magnetic field distributions at the symmetric and antisymmetric resonances, respectively. As it is seen from the vector diagrams for the electric fields the charge distribution in the system in the symmetric resonance corresponds to the one of a dipole. The electric field distribution in the antisymmetric resonance corresponds to the one of two dipoles oscillating out of phase. From the diagrams for the magnetic field, one can see that the magnetic field in the center of the system in the antisymmetric resonance increases.

while the magnetic moment in the center of the system is zero (see Fig. 2.1 (d)).

In the antisymmetric resonance, in contrast, the plasmon oscillations in the two wires are out of phase, see the electric field distribution in Fig. 2.1(e). The corresponding charge dynamics in the system can be associated with an equivalent loop current giving rise to a magnetic moment. The increase of the magnetic field between the wires is clearly seen in Fig. 2.1(f).

It has been demonstrated that a double cut-wire structure owes its magnetic response to the excitation of the antisymmetric mode. As a result, it can be used as a magnetic metaatom of a MM to manipulate its effective magnetic permeability.

It should be emphasized that the excitation of the plasmonic modes is a result of the interaction of the electrons of the metal with the electric field. As a result, the magnetic moment of the system is induced dominantly by the electric field of an exciting electromagnetic wave.

The excitation of a mode of a double cut-wire system is possible if the overlap integral of the mode profile and the exciting field is nonzero. Hence, the excitation of the antisymmetric mode requires either the asymmetry of the exciting field or the system itself. Due to the retardation effect, the exciting electric field commonly includes some asymmetry on the dimensions of the metaatom. Thus, the antisymmetric mode can be excited even in a symmetric structure. The fact that the wave "recognizes" the structure of metaatoms, in turn, means that the EM response of MMs is nonlocal and spatial dispersion has to be accounted for in the introduction of their material properties. A possible approach for the introduction of the material parameters of MMs in the framework of the multipole approach was developed in Ref. [59] and is considered in Sec. 2.3.

2.2.3   Optical properties of metals

In the previous sections the localized plasmon polaritons supported by metallic nanoparticles of basic and complex forms were discussed. Besides the form of a nanoparticle, the important parameter determining the eigenfrequency of the plasmon resonance (for a spherical particle see Eq. (2.12)) and the polarizability of the particle (Eq. (2.11)) is the dielectric function of the metal forming the nanoparticle. In this section, the issue of the evaluation of the dielectric function of metals in the case of nanoparticles is discussed.

To describe the optical properties of metals, a model of free electrons moving in a fixed background frame of positive ions is commonly used. The displacement of the negative carriers defining the polarization of the material can be described with a model of a linear harmonic oscillator without a returning force. As a result, the

electric permittivity of a metal is expressed with the well-known Drude-Sommerfeld formula

$$\epsilon_{\mathrm{m}}(\omega) = 1 - \frac{\omega_{\mathrm{p}}}{\omega^2 + i\gamma\omega}, \tag{2.13}$$

where γ is the damping constant and the plasma frequency is

$$\omega_{\mathrm{p}} = \frac{1}{\epsilon_0} \frac{e^2 N}{m}, \tag{2.14}$$

with m - the mass of the electron, e - the electron charge , N - the concentration of the electrons.

For noble metals, the free-electron model is valid in a broad spectral range up to optical frequencies, where interband transitions first occur. At high optical frequencies the electrons from the filled band below the Fermi surface can be excited to the higher bands by the photons. For example, for gold the interband transitions occur in the optical spectral region and the free-electron model fails at wavelengths less than 1 µm [75]. Nevertheless, the effects connected with interband transitions can be accounted for in the Drude-Sommerfeld formula, using the model of bounded electrons referenced with the resonance frequency ω_{0i}, damping γ_i, and amplitude f_i. Accordingly, resonant Lorentz-oscillator terms of the form $\frac{f_i}{\omega_{0i}^2 - \omega^2 + i\gamma_i\omega}$ are introduced into the Drude-Sommerfeld formula.

There are different sources providing the dielectric function of noble metals measured on thin films in the literature [75–77]. However, the published dielectric functions vary significantly. As an example, in Fig. 2.2 the real and imaginary parts of $\epsilon(\lambda)$ for gold from the "Handbook of Optical Constants of Solids", ed. Palik Ref. [76] (originally measured in Ref. [78]) and from the work of Johnson and Christy Ref. [75] are presented. The difference between the published data demonstrates that the dielectric function of a thin metallic film depends significantly on the fabrication process, which determines the cluster building and as a result the quality of the crystallographic structure of the metal.

Moreover, studies conducted on plasmonic particles of small sizes (2 nm - 20 nm) have shown that the dielectric function of a metal depends on the size of the particles (Ref. [79–81] and references in Ref. [82]). Experimental investigations on particles of different sizes have shown that the bandwidth of the plasmon resonance strongly depends on the size of the particle. However, the absorption cross section σ_{abs} of a
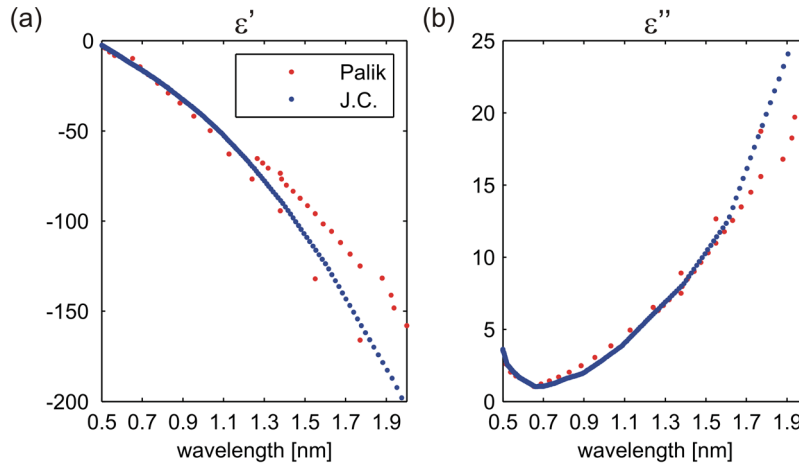
Figure 2.2: (a) - real part and (b) - imaginary part of the electric permittivity $\epsilon(\lambda)$ of gold according to Palik Ref. [76] and Johnson and Christy Ref. [75] data.

small spherical particle within the long wave approximation is

$$\sigma_{\mathrm{abs}} = \omega\sqrt{\epsilon_{\mathrm{h}}}\alpha''_{\mathrm{sphere}}/c \tag{2.15}$$
$$= 9\frac{\omega}{c}\epsilon_{\mathrm{h}}^{3/2}V\frac{\epsilon''(\omega)}{\left(\epsilon'(\omega) + 2\epsilon_{\mathrm{h}}\right)^2 + \left(\epsilon''(\omega)\right)^2},$$

where $\alpha''_{\mathrm{sphere}}$ is the imaginary part of the polarizability of the sphere α_{sphere} (see Eq. (2.11)), ϵ_{h} is the dielectric function of the host medium, and V is the volume of the particle [66]. One can see that σ_{abs} contains the size of the particle only in the volume factor V, which does not influence the position and bandwidth of the resonance (the denominator in Eq. (2.15) does not depend on V). Thus, for small particles the experimentally observed broadening of the plasmon bandwidth with decreasing particle size must be related to the increase of the damping constant γ in the Drude-Sommerfeld formula for $\epsilon_{\mathrm{m}}(\omega)$ of a metal (Eq. (2.13)). The damping constant γ in bulk is related to the lifetimes of the electron scattering processes defined by the scattering of the electron on other electrons, phonons, and lattice defects. Since the free path of the conducting electron in noble metals is in the order of tens of nanometers, electron-surface scattering due to the particle's boundaries becomes important for small particles. According to Ref. [83, 84], the damping coefficient γ in the Drude-Sommerfeld model for $\epsilon_{\mathrm{m}}(\omega)$ of a small particle can be redefined as

$$\gamma(r) = \gamma_0 + \frac{Av_{\mathrm{F}}}{r}. \tag{2.16}$$

Here γ_0 is the bulk damping constant, v_{F} is the velocity of the electrons at the Fermi energy, r is the radius of the particle, and A is a parameter including details of the

scattering process for electrons in a particle [85].

For large particles ($r > 25\,\mathrm{nm}$) the broadening of the plasmon bandwidth is caused mainly by radiation effects as the increased size of the particle becomes comparable to the wavelength of light [66]. It should be emphasized that there is a lack of studies on the dielectric function of metals in the case of large plasmonic particles. The existing studies on spherical particles with sizes up to $100\,\mathrm{nm}$ give inconsistent results regarding the dependence of the dielectric function on its size and surface quality (Ref. [86–88] and references in Ref. [82]).

A systematic study of the dielectric function of nanostructures used in metamaterials was conducted by V. P. Drachev et al. [89] for silver double wires of different thicknesses and surface qualities. The authors argued that, though the loss at the plasmon resonances of the coupled wires increases with increasing roughness, it does not affect the dielectric function. The imaginary part of dielectric function of silver for the double-wires, in turn, depends significantly on the geometry of the wires.

In short, the damping in $\epsilon_\mathrm{m}(\omega)$ depends significantly on the fabrication process, which determines the quality of the crystallographic structure of the metal. Additionally, the application of different etching processes during the fabrication of nanostructures results in the growth of the surface roughness, which can contribute to a stronger inelastic electron-surface scattering. These effects can be accounted for by increasing the damping constant γ in the Drude-Sommerfeld model for a metal. It can be shown that an increase of γ influences the imaginary part of dielectric function of a metal $\epsilon_\mathrm{m}''(\omega)$ stronger than its real part $\epsilon_\mathrm{m}'(\omega)$ [89]. Thus, in the case of nanostructures the dielectric function of metal is commonly obtained by the direct tuning of the imaginary part of published tabulated values of $\epsilon_\mathrm{m}(\omega)$, which were measured on unstructured thin films [25, 29, 90].

2.3 Effective material parameters of MMs

Using a mixture of materials is a well known method for advanced control of the dielectric function of an effective medium. The effective dielectric permittivity of such an effective material in the simplest case is calculated as the averaged value of the permittivities of the intrinsic components according to their concentrations. It is also known, that by shaping the constitutive phases, for example considering inclusions of different forms encapsulated into a host medium, a richer optical response than just the averaged one can be realized [66].

The problem of the definition of the average dielectric function of a composite material, in the general case, is complicated by the presence of interactions between the components. Hence, a number of formulas has been derived to approximate

the effective dielectric function. Among them are the Maxwell-Garnett and the Lorentz-Lorenz formulas (see references in [91]) and the Bruggeman [92] approach.

However, these theories were developed to treat cases where the polarization and magnetization of effective media are directly connected to the electric and magnetic fields, respectively. In the case of metamaterials, however, the mesoscopic particles of complex form provide a magnetic response induced by the electric field of the incoming wave. Thus, the development of an advanced effective medium theory for the metamaterials was required.

The concept of a metamaterial acting as an artificial effective medium imposes that it is structured on dimensions much smaller than the wavelength of light but larger than the atomic sizes. Under this assumption, electromagnetic wave interaction with the individual metaatom can be formulated in terms of the macroscopic material properties of its constitutive elements, i.e. its electric permittivity. For the definition of the macroscopic parameters of the metamaterial, in turn, a second averaging procedure of Maxwell's equations must be performed. An attempt to introduce the macroscopic properties of metamaterials through the second averaging procedure of the microscopic Maxwell's equations was undertaken in Ref. [59]. To account for the complex form of the metaatoms the authors of Ref. [59] used an approach based on the multipole expansion accepted in the classical electrodynamics of complex media [93–95]. Though the authors of Ref. [59] introduced the averaging procedure phenomenologically without a strict theoretical proof, the validity of the procedure was established by numerous numerical simulations (see the thesis of J. Petschulat [60]). As the multipole approach was used in this work for the description and optimization of the effective properties of double wire MMs, the main points of this theory will be presented here.

Firstly, the derivation of the macroscopic Maxwell's equations for a media consisting of complex atoms will be presented according to Ref. [96][1]. In the second step, the application of the multipole approach for MMs according to Ref. [59] will be discussed.

2.3.1 Macroscopic fields and material equations

The starting point for the derivation of the macroscopic Maxwell's equations is the formulation of the microscopic Maxwell's equations and the charge movement equation. The microscopic Maxwell's equations describing the electric field $e(R, t)$ and the magnetic field $b(R, t)$ at the point with the coordinates R and at the time t, generated by a group of point particles $i = 1, 2..n$ with charges q_i, positions $R_i(t)$

---

[1] The notations accepted in Ref. [96] are retained.

and velocities $\dot{\boldsymbol{R}}_i(t)$ are

$$\operatorname{rot} \boldsymbol{e} = -\frac{\partial \boldsymbol{b}}{\partial t}, \tag{2.17}$$

$$\operatorname{rot} \boldsymbol{b} = \frac{1}{c^2}\frac{\partial \boldsymbol{e}}{\partial t} + \mu_0 \sum_i q_i \dot{\boldsymbol{R}}_i \delta(\boldsymbol{R}_i - \boldsymbol{R}), \tag{2.18}$$

$$\operatorname{div} \boldsymbol{e} = \frac{1}{\epsilon_0} \sum_i q_i \delta(\boldsymbol{R}_i - \boldsymbol{R}), \tag{2.19}$$

$$\operatorname{div} \boldsymbol{b} = 0. \tag{2.20}$$

The microscopic Maxwell's equations together with the equations of motion for a set of charged particles

$$m\ddot{\boldsymbol{R}}_i = q_i \left[\boldsymbol{e}\left(\boldsymbol{R}_i, t\right) + \dot{\boldsymbol{R}}_i \times \boldsymbol{b}\left(\boldsymbol{R}_i, t\right) \right] \tag{2.21}$$

form a self consistent system describing all microscopic fields. The fields $\boldsymbol{e}\left(\boldsymbol{R}_i, t\right)$ and $\boldsymbol{b}\left(\boldsymbol{R}_i, t\right)$ affecting the particle i in Eq. (2.21) are the sums of the external field and the field generated by the other particles. The interaction of a particle with the magnetic field expressed with the second term in Eq. (2.21) can be neglected in the non-relativistic case.

In natural materials, charged point particles (electrons and nuclei) are often grouped into stable sets, like atoms or molecules. In this case, it is convenient to express the position of a point particle in a stable group as

$$\boldsymbol{R}_{ik} = \boldsymbol{R}_k + \boldsymbol{r}_{ki}, \tag{2.22}$$

where $\boldsymbol{R}_k$ is the position of some dedicated point of the stable group k, for instance the center of mass, while $\boldsymbol{r}_{ki}$ $(i = 1, 2, \ldots)$ are the internal coordinates, which define the offsets of the constituent particles ki from the dedicated point of the stable group k.

If the atomic dimension $|\boldsymbol{r}_{ki}|$ is much smaller than the distance $|\boldsymbol{R}_k - \boldsymbol{R}|$ from the observation point $\boldsymbol{R}$ of the fields to the central point $\boldsymbol{R}_k$ of the atom, the solutions $\boldsymbol{e}$ and $\boldsymbol{b}$ of the field equations can be considered as converging series of expansions in $|\boldsymbol{r}_{ki}| / |\boldsymbol{R}_k - \boldsymbol{R}|$. Accordingly, the coordinates and the velocities of the charged particles in Eqs. (2.18) and (2.19) can be developed in powers of $\boldsymbol{r}_{ki}$ around $|\boldsymbol{R}_k - \boldsymbol{R}|$. The number of terms in the expansion which have to be taken into account depends on the material. In diluted systems, the observation point $\boldsymbol{R}$ of the fields can easily be chosen at a distance $|\boldsymbol{R}_k - \boldsymbol{R}|$ from the atom which is large compared to the atomic dimension $|\boldsymbol{r}_{ki}|$. As a result, the expansion parameter $|\boldsymbol{r}_{ki}| / |\boldsymbol{R}_k - \boldsymbol{R}|$ is small compared to unity and only a few terms of the expansion

have to be taken into account. Hereafter, for the sake of clarity, the consideration will be restricted to the case of diluted systems only.

The system of equations obtained after the expansion of the fields (not presented here) can be simplified introducing physical quantities characterizing the internal atomic structure. Besides the total charge

$$q_k = \sum_i e_{ki}, \tag{2.23}$$

the stable group is characterized with the electromagnetic multipole moments, which are useful combinations of the internal atomic parameters. In the case of a diluted system, it is necessary to consider only the electric moments of the first and second orders and the magnetic moment of the first order [97]. The definitions of the multipoles are the following: the electric dipole moment is

$$\bar{\boldsymbol{\mu}}_k^{(el)} = \sum_i e_{ki} \boldsymbol{r}_{ki}, \tag{2.24}$$

the electric quadrupole moment is

$$\bar{\boldsymbol{q}}_k^{(el)} = \frac{1}{2} \sum_i e_{ki} \boldsymbol{r}_{ki} \boldsymbol{r}_{ki}, \tag{2.25}$$

and the magnetic dipole moment is

$$\bar{\boldsymbol{\nu}}_k^{(m)} = \frac{1}{2} \sum_i e_{ki} \boldsymbol{r}_{ki} \times \dot{\boldsymbol{r}}_{ki}. \tag{2.26}$$

Though the values of the multipole moments may depend on the choice of the privileged point $\boldsymbol{R}_k$, their forms will always be the same combinations of the internal coordinates $\boldsymbol{r}_{ki}$. Writing the charge and current densities as

$$\rho_0 = \sum_k q_k \delta (\boldsymbol{R}_k - \boldsymbol{R}), \tag{2.27}$$

$$\boldsymbol{j_0} = \sum_k q_k \dot{\boldsymbol{R}}_k \delta (\boldsymbol{R}_k - \boldsymbol{R}), \tag{2.28}$$

and introducing the atomic electric and magnetic polarization densities

$$\boldsymbol{p} = \sum_k \left(\bar{\boldsymbol{\mu}}_k^{(el)} - \nabla \bar{\boldsymbol{q}}_k^{(el)} \right), \tag{2.29}$$

$$\boldsymbol{m} = \sum_k \bar{\boldsymbol{\nu}}_k^{(m)}, \tag{2.30}$$

22

the field equations become

$$\operatorname{rot} \boldsymbol{e} = -\frac{\partial \boldsymbol{b}}{\partial t}, \tag{2.31}$$

$$\operatorname{rot} \boldsymbol{b} = \frac{1}{c^2} \frac{\partial \boldsymbol{e}}{\partial t} + \mu_0 \left(\boldsymbol{j_0} + \frac{\partial \boldsymbol{p}}{\partial t} + \operatorname{rot} \boldsymbol{m} \right), \tag{2.32}$$

$$\operatorname{div} \boldsymbol{e} = \rho_0 - \operatorname{div} \boldsymbol{p}, \tag{2.33}$$

$$\operatorname{div} \boldsymbol{b} = 0. \tag{2.34}$$

To derive the macroscopic Maxwell's equations from the atomic equations, an appropriate averaging procedure has to be applied. There are two approaches to conduct an averaging procedure: statistical averaging [96, 97] and spatial averaging over a volume [65, 98]. For solids, where the particles do not move much with respect to their averaged positions, the use of spatial averaging to smooth out rapid fluctuations is unavoidable [99]. With the notation for the macroscopic quantities, i.e. the macroscopic fields

$$\boldsymbol{E} = \langle \boldsymbol{e} \rangle, \qquad\qquad \boldsymbol{B} = \langle \boldsymbol{b} \rangle, \tag{2.35}$$

the macroscopic charge and current densities

$$\boldsymbol{\rho}_0 = \langle \rho_0 \rangle, \qquad\qquad \boldsymbol{J}_0 = \langle \boldsymbol{j}_0 \rangle, \tag{2.36}$$

and the macroscopic polarization vectors

$$\boldsymbol{P}_{\text{full}} = \langle \boldsymbol{p} \rangle, \qquad\qquad \boldsymbol{M} = \langle \boldsymbol{m} \rangle, \tag{2.37}$$

the macroscopic Maxwell's equations read as

$$\operatorname{rot} \boldsymbol{E} = -\frac{\partial \boldsymbol{B}}{\partial t}, \tag{2.38}$$

$$\operatorname{rot} \boldsymbol{B} = \frac{1}{c^2} \frac{\partial \boldsymbol{E}}{\partial t} + \mu_0 \left(\boldsymbol{J}_0 + \frac{\partial \boldsymbol{P}_{\text{full}}}{\partial t} + \operatorname{rot} \boldsymbol{M} \right), \tag{2.39}$$

$$\operatorname{div} \boldsymbol{E} = \boldsymbol{\rho}_0 - \operatorname{div} \boldsymbol{P}_{\text{full}}, \tag{2.40}$$

$$\operatorname{div} \boldsymbol{B} = 0. \tag{2.41}$$

In optics the displacement vectors ($\boldsymbol{D}$ and $\boldsymbol{H}$) are usually introduced as

$$\boldsymbol{D} = \epsilon_0 \boldsymbol{E} + \boldsymbol{P}_{\text{full}}, \qquad\qquad \boldsymbol{H} = \mu_0^{-1} \boldsymbol{B} - \boldsymbol{M}. \tag{2.42}$$

The introduction of the electric displacement $\boldsymbol{D}$ and the magnetic field $\boldsymbol{H}$ allows

23

one to make use of the traditional boundary conditions, that is the continuity of the tangential components of the fields $\boldsymbol{E}$ and $\boldsymbol{H}$ on the border between two media. As a result, the field equations take the form:

$$\text{rot } \boldsymbol{E} = -\frac{\partial \boldsymbol{B}}{\partial t}, \tag{2.43}$$

$$\text{rot } \boldsymbol{H} = \frac{\partial \boldsymbol{D}}{\partial t} + \boldsymbol{J}_0, \tag{2.44}$$

$$\text{div } \boldsymbol{D} = \boldsymbol{\rho}_0, \tag{2.45}$$

$$\text{div } \boldsymbol{B} = 0. \tag{2.46}$$

The macroscopic electric dipole and quadrupole moment densities for a material with a concentration of the atoms η are defined as

$$\boldsymbol{P} = \eta \sum_i e_i \boldsymbol{r}_i, \qquad\qquad Q_{i',j'} = \frac{\eta}{2} \sum_i e_i \boldsymbol{r}_{ii'} \boldsymbol{r}_{ij'}. \tag{2.47}$$

The density of macroscopic electric dipole $\boldsymbol{P}$ is a vector and the density of macroscopic electric quadrupole moment $\boldsymbol{Q}$ is a symmetric tensor. The magnetic dipole moment density, which is a vector, has the form

$$\boldsymbol{M} = \frac{\eta}{2} \sum_i e_i \boldsymbol{r}_i \times \dot{\boldsymbol{r}}_i. \tag{2.48}$$

Accordingly, the displacement vectors can be written as

$$\boldsymbol{D} = \epsilon_0 \boldsymbol{E} + \boldsymbol{P} - \nabla \boldsymbol{Q}, \qquad\qquad \boldsymbol{H} = \mu_0^{-1} \boldsymbol{B} - \boldsymbol{M}. \tag{2.49}$$

To introduce an explicit connection between the electromagnetic moments and the fields, an appropriate model to describe a medium should be chosen. If the model of a medium is known, the charge and current densities can be found using the equation of motion

$$m\ddot{\boldsymbol{r}}_i = q_i \left\{ \boldsymbol{E}\left(\boldsymbol{R}_i, t\right) + \dot{\boldsymbol{r}}_i \times \boldsymbol{B}\left(\boldsymbol{R}_i, t\right) \right\}, \tag{2.50}$$

where the $\boldsymbol{E}\left(\boldsymbol{R}, t\right)$ and $\boldsymbol{B}\left(\boldsymbol{R}, t\right)$ are macroscopic fields. The macroscopic field equations supplemented with the material equations Eq. (2.49) form a self consistent system for the description of light interaction with a material.

To connect the displacement vectors with the electric field and the magnetic induction additional characteristics (electric permittivity and magnetic permeability) of a material are introduced. In the general case, when spatial and time dispersion are present, by applying the Fourier transformation, the electric permittivity and

the magnetic permeability are defined as

$$D_i(\boldsymbol{k},\omega) = \epsilon_0\epsilon_{ij}(\boldsymbol{k},\omega)E_j(\boldsymbol{k},\omega), \qquad (2.51)$$

$$H_i(\boldsymbol{k},\omega) = \mu_0^{-1}\mu_{ij}^{-1}(\boldsymbol{k},\omega)B_j(\boldsymbol{k},\omega). \qquad (2.52)$$

Summarizing, a way to obtain the macroscopic Maxwell's equations and material equations for a medium consisting of complex molecules by introduction of the electromagnetic moment densities has been shown.

2.3.2 The multipole approach for metamaterials

In the preceding section it was shown how the macroscopic material equations for a material consisting of complex molecules can be introduced accounting for the electromagnetic multipoles.

According to the definition of MMs as materials consisting of complex metaatoms, a homogenization procedure has to be conducted for MMs to derive the macroscopic Maxwell's equations describing light interaction with a metamaterial. The idea to apply the averaging procedure to MMs using the multipole expansion for the charge dynamics in analogy to natural materials was proposed in Ref. [59]. Using this approach the material equations in the form expressed by Eq. (2.49) can be assigned to a MM and consequently the dispersion relation can be derived by solving the macroscopic Maxwell's equations.

An important step done by the authors of Ref. [59] was the introduction of a material model based on coupled linear harmonic oscillators. Using this model the complex plasmonic dynamics in a metaatom can be described in terms of the linear harmonic oscillators associated with the induced dipole moments in the system. In the case of a metaatom based on double cut-wires the material model can be introduced as follows. In the system of double cut-wires illuminated under a normal angle of incidence as it is shown in Fig. 2.3(a), electrons in the wires driven by the electric field shift relative to the positively charged ion frame. The induced charge distribution can be represented with a system of four charges as shown in Fig. 2.3(b), where the two upper and the two lower charges represent electric dipoles. The system for the amplitudes x_1 and x_2 corresponding to the elongation of the negatively charged carrier density driven by the electric field is

$$\ddot{x}_1(t) + \gamma\dot{x}_1(t) + \omega_0^2 x_1(t) - \sigma x_2(t) = \frac{q}{m}E_{1x}(y-y_1,t),$$
$$\ddot{x}_2(t) + \gamma\dot{x}_2(t) + \omega_0^2 x_2(t) - \sigma x_1(t) = \frac{q}{m}E_{2x}(y+y_1,t), \qquad (2.53)$$

where ω_0 is the eigenfrequency of the oscillators; γ is the damping constant; q is the
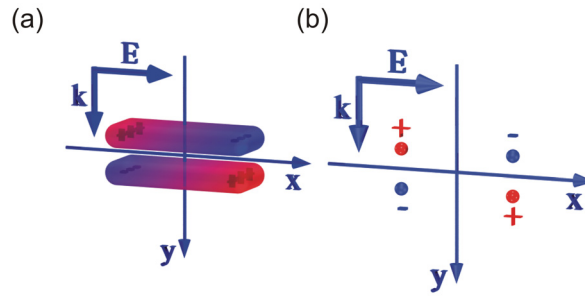
Figure 2.3: (a) - Illustration of a double cut-wire system with an excited antisymmetric mode and (b) - an oscillator model describing the dynamic of the system.

effective charge; m is the mass of the effective carrier; σ is the coupling constant describing the interaction between the cut-wires; $-y_1$ and y_1 are the positions of the carriers along the y coordinate. The solution of the equation system (2.53) gives the amplitudes x_1 and x_2 describing the coordinates of the charges as functions of the electric field. Using the derived coordinates the multipole moments ($\boldsymbol{P}$, $\boldsymbol{Q}$, and $\boldsymbol{M}$) can be analytically described according to Eqs. (2.47) and (2.48).

The dispersion relation for the wave vector $\boldsymbol{k}(\omega)$ in a metamaterial can be found in a common way by plugging the material equations Eq. (2.49) into the Maxwell's equations Eqs. (2.43) - (2.46) and solving the self consistent system. The parameters of the oscillator model, which can be used to describe the response of a real metaatom, are supposed to be found from the comparison of the analytically derived dispersion with the data obtained from rigorous simulations or experiments for the specific material.

It should be emphasized that for a bulk MM the dispersion relation completely describes the light propagation in the MM. Alternatively a MM can be characterized with the effective refractive index $\boldsymbol{k}(\omega) = n_{\text{eff}}(\omega)\boldsymbol{k_0}$. To solve a boundary problem, however, the effective material parameters $\epsilon_{\text{eff}}(\omega)$ and $\mu_{\text{eff}}(\omega)$ can be introduced using the electromagnetic multipoles (see Eqs. (2.51) and (2.49)).

There are two features of contemporary MMs that limit the generality of the multipole approach. Firstly, as the size of the metaatoms is only a few times smaller than the wavelength of light in the medium, the conduction of the second averaging procedure in its classical meaning is questionable. Furthermore, most contemporary MMs belong to the class of dense media, that is, the distance between metaatoms is comparable to their sizes. In this case, the consideration of the multipoles of the first order may be not sufficient to provide an accurate description of MMs. In chapter 5 of this thesis it is shown how the problem of densely packed metamaterials can be overcome without resorting to multipoles of higher orders.

Nevertheless, numerical and experimental works performed on different types of MMs [100–102] have shown that the multipole theory provides a qualitatively and quantitatively correct description of them. Moreover, it is probably the only theoretic model providing insight into the nature of the magnetic MMs and connecting the internal dynamics in the metaatoms with the macroscopic optical properties of MMs.

2.3.3 Retrieval of the effective parameters

In the preceding sections, it has been shown how the effective material parameters can be introduced for metamaterials using the electromagnetic moments. However, to access these parameters in the experiment, they have to be connected to quantities which can be physically measured.

Commonly, the concept of a homogeneous medium is used to access effective parameters from characteristics experimentally measured in the far field [103]. According to this concept, a MM layer of a thickness d is considered as a homogeneous layer described with a pair of effective parameters, the effective refractive index $n_\mathrm{eff}(\lambda)$ and the effective impedance $z_\mathrm{eff}(\lambda)$ or the effective permittivity $\epsilon_\mathrm{eff}(\lambda)$ and the effective permeability $\mu_\mathrm{eff}(\lambda)$. The effective parameters are derived by inverting the analytical expressions for the complex transmission $t(\lambda)$ and reflection coefficients $r(\lambda)$ obtained from the common matrix method [104]. For the case of normal incidence the corresponding equations for the effective refractive index and effective impedance according to Ref. [105] are

$$k = k_0 n_\mathrm{eff} = \pm \frac{1}{d} \left[\arccos \left(\frac{k_\mathrm{s}(1 - r^2) + k_\mathrm{c}\,(t/a)^2}{(t/a)\left[k_\mathrm{s}(1 - r) + k_\mathrm{c}(1 + r)\right]} + 2m\pi \right) \right], \qquad (2.54)$$

$$z_\mathrm{eff} = \pm \sqrt{\frac{k_\mathrm{s}^2\,(1 - r)^2 - k_\mathrm{s}^2\,(t/a)^2}{(r + 1)^2 - (t/a)^2}}. \qquad (2.55)$$

Here the coefficient a depends on the polarization: $a = 1$ for the TE polarization, $a = \sqrt{\epsilon_\mathrm{s}\mu_\mathrm{c}/\epsilon_\mathrm{c}\mu_\mathrm{s}}$ for the TM polarization. $k_0 = \frac{2\pi}{\lambda_0}$, $k_\mathrm{s} = \frac{2\pi}{\lambda_0}\sqrt{\epsilon_\mathrm{s}\mu_\mathrm{s}}$, and $k_\mathrm{c} = \frac{2\pi}{\lambda_0}\sqrt{\epsilon_\mathrm{c}\mu_\mathrm{c}}$ are the wave vectors in vacuum, in the input medium and output medium, respectively. λ_0 is the wavelength of light in vacuum. The signs of n_eff and z_eff are chosen to satisfy the condition of a passive medium. This is the simultaneous positivity of the imaginary part of n_eff and the real part of z_eff. The ambiguity related to the retrieval of the arccos function in n_eff (Eq. (2.54)) can be eliminated by starting the retrieval in the limit $\lambda \to \infty$ where $m = 0$. The effective electric permittivity and

permeability, in turn, are defined as

$$\epsilon_{\text{eff}} = n_{\text{eff}}/z_{\text{eff}}, \qquad\qquad \mu_{\text{eff}} = n_{\text{eff}} z_{\text{eff}}. \qquad (2.56)$$

However, the validity of the assignment of the parameters obtained for a single layer MM to a bulk MM has to be critically reviewed. Firstly, MMs available in experiments contain only a few functional layers [106, 107] and can not be considered as a bulk material by definition. Secondly, numerical investigations performed on bulk MMs [41, 108–110] obtained by stacking the functional layers, revealed higher-order Bloch modes in the dispersion relation. If the high-order Bloch modes prevail over the fundamental mode, the introduction of bulk effective parameters fails in general. Of course, in diluted MMs where the separation between the functional layers is enough to prevent the interaction between the layers, the fundamental Bloch mode predominates. Consequently, in this case the parameters retrieved for a single layer can be assigned to the corresponding bulk material [37, 110].

Nevertheless, even though the effective parameters obtained for a single layer with Eq. (2.56) are valid only for the normal angle of incidence and can be hardly considered as material parameters, they turn out to have significant practical importance as quantitative characteristics of structures in optimization problems.

Using Eqs. (2.54) and (2.55), the effective properties of MMs can be retrieved from the complex transmission coefficient $t(\lambda) = |t(\lambda)| \exp[i\phi_{\text{t}}(\lambda)]$ and reflection coefficient $r(\lambda) = |r(\lambda)| \exp[i\phi_{\text{r}}(\lambda)]$ measured in the experiment, for example, using a method presented in chapter 4. Since simultaneous measurements of complex $t(\lambda)$ and $r(\lambda)$ on thin films ($d < 100\,\text{nm}$) are a challenging experimental problem, a method based on the combination of experimental data and numerical simulations is commonly applied to define $n_{\text{eff}}(\lambda)$ and $z_{\text{eff}}(\lambda)$. This method, hereafter referred to as the combined method, requires measurements of the transmittance $T(\lambda) = |t(\lambda)|^2$ and reflectance $R(\lambda) = |r(\lambda)|^2$ only, while the phase information is taken from the numerical simulations. This is possible if the model used in the simulations provides sufficient correspondence of simulated and measured $T(\lambda)$ and $R(\lambda)$. However, in order to achieve a sufficient agreement between simulated and measured data, the adjustment of the parameters of the simulated model is required, which is a time-consuming procedure. Moreover computational requirements for some MMs such as amorphous structures [111] are extremely demanding due to the lack of periodicity. The accuracies of the two methods for the effective index definition are compared in chapter 4.

2.4 Numerical methods

The numerical methods most often used for the study of metamaterial structures are the Fourier Modal Method (FMM) [112–114] and the Finite Difference Time Domain (FDTD) method [115]. The FDTD method is based on the numerical solution of finite-difference equations obtained by discretizing Maxwell's equations in time and space. Though it gives the exact solution of Maxwell's equations without applying any approximation (except the ones occurring due to the discretization of the equations), this method is highly demanding on the computational resources. In the FMM, which is applicable to periodic structures, the solution of Maxwell's equations is reduced to the solution of an eigenvalue problem, which significantly relaxes requirements on the computational resources. In general, a structure under investigation is divided in layers where the dielectric function is periodic in the transverse directions (x and y)

$$\epsilon_i(x,y) = \epsilon_i(x + P_x, y + P_y) \tag{2.57}$$

and constant in the vertical (z) direction. Applying the Fourier expansion for the dielectric function of each layer

$$\epsilon_i(x,y) = \frac{1}{P_x P_y} \sum_n \sum_m \epsilon_i(n,m) e^{ik_x nx} e^{ik_y my} \tag{2.58}$$

and expanding the fields in Floquet-Fourier series [116]

$$\boldsymbol{A}(x,y) = \frac{1}{P_x P_y} \sum_n \sum_m \boldsymbol{A}(n,m) e^{i\alpha_x nx} e^{i\alpha_y my}, \tag{2.59}$$

where $k_x = \frac{2\pi}{P_x}$, $k_y = \frac{2\pi}{P_y}$, and $\alpha_x = k_{0x} + nk_x$, $\alpha_y = k_{0y} + mk_y$ translates the periodic boundary value problem in real space in an algebraic eigenvalue problem in the Fourier space [117]. By matching the electromagnetic boundary conditions at the boundaries of the layers the diffraction problem can be solved.

The accuracy of the FMM method is limited by the number of the Fourier orders taken for the expansion of the dielectric function. In most calculations the number of orders was 16, providing a good compromise between the time of calculations and the accuracy.

Two implementations of the FMM were used for numerical simulations presented in the thesis: a commercially available from RSOFT and a home-made Matlab code originally written by Jari Turunen and modernized for parallel computing by Thomas Paul.

Chapter summary

In this chapter it was shown that according to the condition of a NIM the magnetic response is necessary to realize a negative index material. In the optical spectral range, the required magnetic response can be realized in MMs based on plasmonic double-cut wires. The basics of the localized plasmon polaritons were introduced to explain the functionality of plasmonic metaatoms. Employing the hybridization model, it was shown that the double cut-wire system owes its magnetic response to the excitation of the antisymmetric plasmon mode associated with a nonzero magnetic moment.

In the third section of this chapter the introduction of the effective parameters for metamaterials based on the multipole approach from Ref. [59] was presented. In the framework of this theory, the derivation of the macroscopic Maxwell's equations and material equations for a MM is done in analogy to the classical electrodynamic theory of media consisting of complex molecules by introduction of electromagnetic moments [96].

For the experimental studies of MMs, a connection of the effective material parameters of MMs with measured quantities (transmission and reflection) is essential. This connection can be established using the approach of the equivalent homogeneous layer. However, the retrieved parameters have to be carefully treated. Firstly, the effective parameters can be derived for a MM only in the case of weak dispersion, when the Bloch mode of the zeroth order dominates the dispersion of the material. Secondly, the parameters derived for certain illumination conditions can be used to describe the optical response of the material only for the same conditions.

The last section of the chapter gave a short overview of the Fourier Modal Method applied in this thesis for the numerical analysis of MMs.

Chapter 3

Design and realization of a double element NIM

From the condition of a negative index material (see Sec. 2.1), it follows that the realization of a NIM requires either the real part of the effective permittivity or the real part of the effective permeability of the NIM to be negative. In Sec. 3.1 of this chapter it is demonstrated how the effective permittivity and permeability of a MM can be engineered to fulfill the NIM condition using continuous wires and double cut-wires. The design guidelines for the cut-wires are presented in Sec. 3.2. In this section the results of the numerical investigations of the dependence of the plasmon polariton resonances supported by the cut-wires on the geometry of the structure and the material used for its elements are discussed.

The fabrication technology based on the electron-beam lithography applied for the realization of NIMs is presented in Sec. 3.3 and is evaluated in Sec. 3.4. The results of the investigations of the sensitivity of the plasmon resonances to the fabrication errors are presented in Sec. 3.5.

In the last section of the chapter a double element NIM with a negative effective index at $\lambda = 2.1\,\mu\text{m}$ based on a combination of cut-wires and continuous wires is experimentally demonstrated.

3.1 Shaping the effective parameters of metamaterials

To realize a NIM (Eq. (2.4)), either the real part of the effective permittivity or the real part of the effective permeability has to be negative at the wavelength of interest. A metamaterial with a negative ϵ'_{eff} can be readily designed by introducing metal in its unit cell. Commonly, in the experiment, metal is introduced in the unit
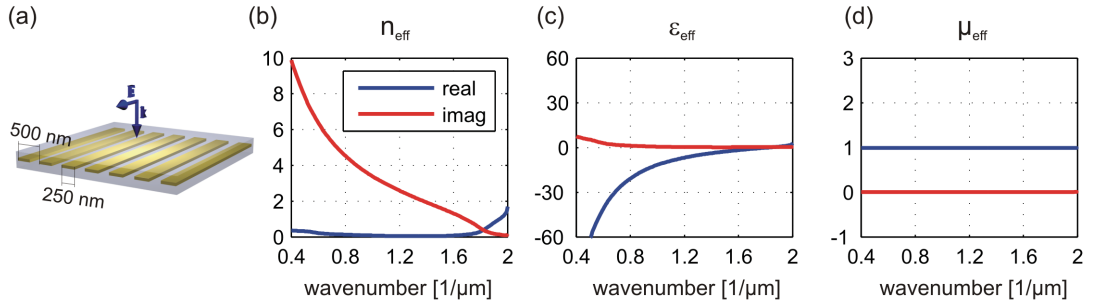
Figure 3.1: (a) - A metamaterial layer consisting of continuous gold wires placed in air (period of the structure is 500 nm, height and width of the wires are 20 nm and 250 nm, respectively); (b) - effective refractive index, (c) - effective permittivity and (d) - effective permeability of the corresponding effective layer.

cell in form of long wires [7], see Fig. 3.1(a). If the electric field of the incoming wave is parallel to the wires, whose volume fill factor is f_{me}, the effective permittivity of the metamaterial is

$$\epsilon_{\text{eff}} = f_{\text{me}}\epsilon_{\text{me}} + (1 - f_{\text{me}})\,\epsilon_{\text{h}}. \tag{3.1}$$

Here ϵ_{h} is the permittivity of the host medium. The effective material parameters of an equivalent homogeneous layer corresponding to the structure in Fig. 3.1(a) are presented in Figs. 3.1(b), (c), and (d). By varying the fill factor of the metal in the unit cell the effective permittivity can be tuned between the value corresponding to the permittivity of the host medium ϵ_{h} and the one of the metal ϵ_{me}. Hence, a metamaterial composed of continuous metallic wires has the optical properties of a diluted metal.

The control of the dielectric function of a composite material beyond the limits of the averaged permittivities (Eq. (3.1)) is possible by using metallic nanoparticles supporting localized plasmon polaritons discussed in Sec. 2.2.1. The excitation of a
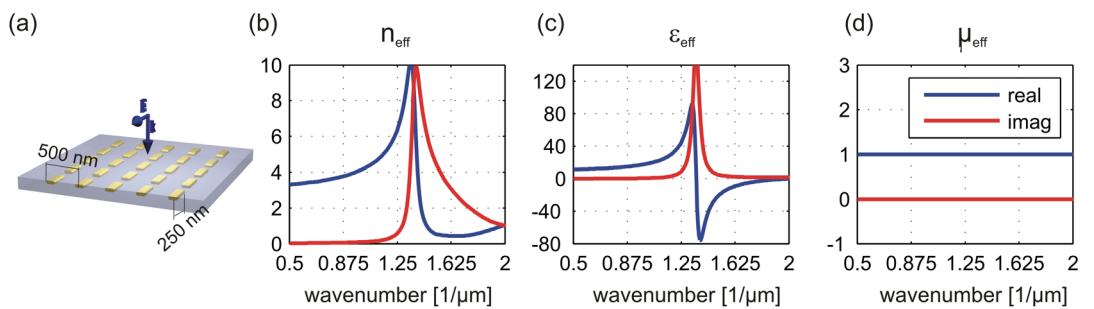

Figure 3.2: (a) - Cut-wire metamaterial made of gold with the a period of 500 nm, a height of 20 nm and a length of the wires of 250 nm. (b) - The corresponding effective refractive index (c) - the effective permittivity, and (d) - the effective permeability.
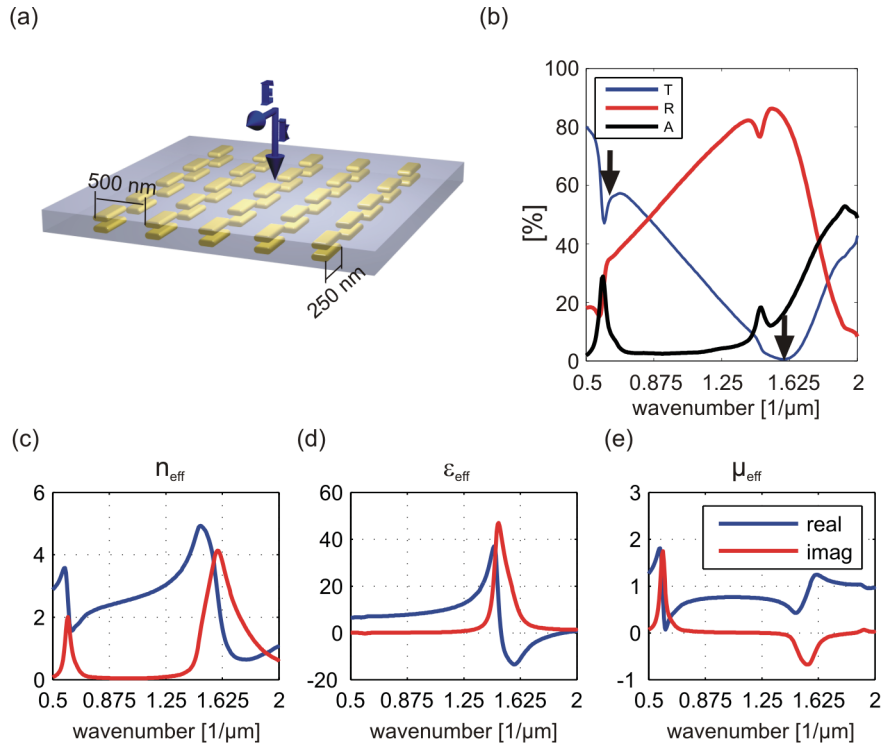
Figure 3.3: (a) - Double cut-wire metamaterial, (b) - corresponding transmittance (blue line), reflectance (red line) and absorbance (black line). (c) - Effective refractive index, (d) - effective permittivity and (e) - effective permeability of the double cut-wire structure made of gold with a period, height and length of the wires of 500 nm, 20 nm, and 250 nm, respectively.

plasmon resonance results in the rapid increase of the polarizability of the particle and causes the appearance of a Lorentz-form resonance in the effective permittivity. In Fig. 3.2(a) an example of a MM based on plasmonic cut-wires is presented. The effective refractive index, permittivity, and permeability of the MM are shown in Fig. 3.2. One can see that in the spectral range where the localized plasmon resonance is excited (wavenumbers around $1.3\,\mu m^{-1}$) the permittivity of the effective medium experiences a resonance, and the values of ϵ_{eff} deviate significantly from the simple averaged ones of the constitutive media. The magnetic permeability of the material, in turn, is not affected.

As it has been discussed in Sec. 2.2.2 a magnetic response in the optical spectral range can be realized with a metaatom consisting of double cut-wires. The spectral response of a layer consisting of double cut-wires is shown in Fig. 3.3(a). The excitation of the symmetric and antisymmetric modes corresponds to the appearance of two minima in the transmittance (marked by black arrows in Fig. 3.3(b)). The excitation of the symmetric mode (wavenumbers around $1.62\,\mu m^{-1}$), characterized by strong in-phase dipole moments induced in the cut-wires, influences the effec-
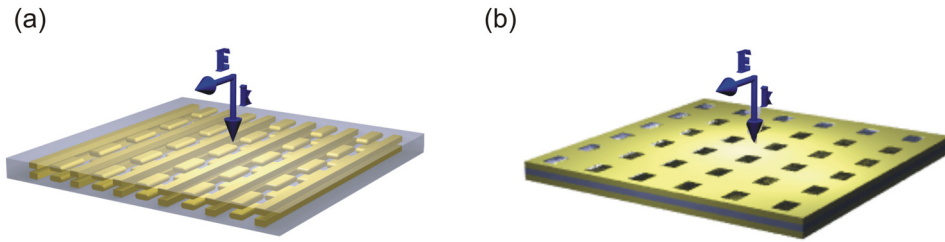
Figure 3.4: (a) - Double element NIM based on cut-wires and continuous wires, (b) - fishnet NIM, which can be obtain by merging cut-wires and continuous wires in the unit cell.

tive electric permittivity of the metamaterial (see Fig. 3.3(d)). The antisymmetric mode (wavenumbers around $0.6\,\mu m^{-1}$), associated with a strong magnetic moment induced in the cut-wires, causes a Lorentz-shaped resonance behavior of the effective magnetic permeability (see Fig. 3.3(e)). The antiresonances appearing in the permittivity at wavenumbers around $0.6\,\mu m^{-1}$ and permeability at wavenumbers around $1.62\,\mu m^{-1}$ corresponding to the frequencies of the antisymmetric and symmetric resonances, respectively, are artifacts of the retrieval algorithm [118, 119]. These artifacts originate in the assumption of the homogeneity of a metamaterial layer, which in the case of contemporary metamaterials holds in a weak sense only, as the size of the metaatoms is only a few times smaller than the wavelength of the incoming light. The appearance of the antiresonances can be considered as the evidence that the resonances of the system are not purely symmetric and antisymmetric. In the framework of the multipole model, this means that the charge dynamics in both resonances is characterized with nonzero dipole, quadrupole and magnetic moments.

From the previous discussion it follows that in order to realize a NIM based on the combination of continuous wires and cut-wires (see Fig. 3.4(a)), the parameters of the double cut-wires have to be optimized to provide the asymmetric resonance at the target frequency. The parameters of the continuous wires, in turn, have to assure negative values of the electric permittivity in the corresponding spectral range. The following sections of this chapter are devoted to the design and experimental realization of such double element NIMs. It should be noticed that the geometry based on separated continuous wires and cut-wires has also been experimentally and theoretically investigated in the microwave and far infrared domains [47–50]. In this thesis the design and realization of such a NIM in the near infrared spectral range are presented. In the works of other groups [25, 26] it has been shown that,

in terms of the figure of merit, the most effective combination of double cut-wires and continuous wires is the fishnet structure (Fig. 3.4(b)), where these two components merge into a single unit. Nevertheless, a structure with the double wires being separated from the continuous wires is of interest due to the possibility to control the geometry of both elements independently. This, together with a layer-by-layer fabrication technology, allows the control of the symmetry of the NIM's unit cell in longitudinal direction. In chapter 5 it is shown how the magnetic response of double wires can be controlled by breaking the symmetry of the cut-wires. Thus, the key point of the NIM's efficiency optimization is the technological ability to control the unit cell geometry.

3.2 Design guidelines for a double element NIM

3.2.1 Choice of the materials

Commonly, the design of a NIM starts with the choice of a metal, which is dictated by the targeted wavelength region of the negative refraction, the desired efficiency and the manufacturing facilities. The efficiency of NIMs is usually described by the FOM (see Eq. (2.5)), which is the absolute ratio of the real to the imaginary part of the refractive index. According to Eq. (2.5), a significant improvement of the efficiency of a NIM can be obtained by decreasing the imaginary part of the permittivity in the frequency range of interest. This can be achieved by the appropriate choice of the metal used in the unit cell of a NIM. In practice, gold and silver are the most commonly used metals for the realization of NIMs in the optical region. The parameters for the Drude model (see Eq. (2.13) in Sec. (2.2.3)) for gold and silver from Ref. [75] are given in Tab. 3.1. In Fig. 3.5 the electric permittivities of the metals are presented in the VIS and NIR spectral ranges. One can see that for silver,
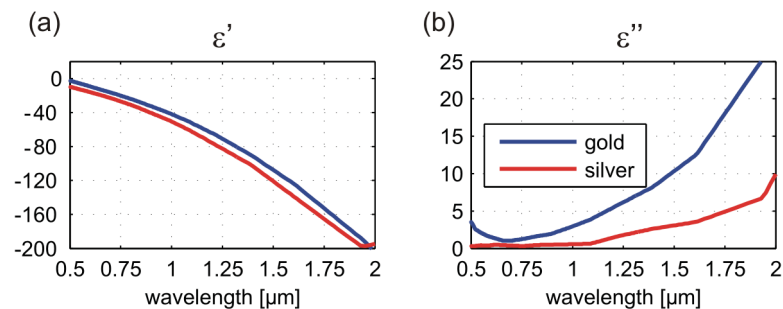

Figure 3.5: Johnson and Christy data [75] for gold and silver. (a) - Real and (b) - imaginary parts of the permittivities of gold (blue line) and silver (red line).

35

due to the higher plasma frequency in the spectral range of interest (wavelengths from 1 μm to 2 μm), the imaginary part of the permittivity is up to five times less than for gold. Thus, for the realization of NIMs with a high FOM, silver should be preferred. The fabrication of a low-loss silver-based NIM based on the fishnet design was demonstrated by G. Dolling et al. [27]. Nevertheless, in the research of this Thesis the preference was given to gold, because of its chemical stability facilitating the longterm usage of the samples in the laboratory.

Regarding the choice of the dielectric spacer, isolating the two cut-wires, there are no strict limitations, because the coupling between the cut-wires can be controlled either by the refractive index of the spacer or its thickness.

3.2.2 Tuning of the localized plasmon polariton resonances

The design process of a NIM can be optimized if the dependence of the frequency and the strength of the plasmon resonances on the geometry of the wires are known. Since these dependencies can be derived in an analytical form only for particles of spherical or ellipsoidal shapes (Eq. (2.9) and 2.11), resorting to numerical simulations is unavoidable to obtain an accurate parameter set. From the spectra simulated with FMM (see Sec. 2.4) for single layers of periodically arranged single cut-wires the required dependencies can be derived. In Fig. 3.6 the dependencies of the position of the plasmon resonance on the length L (Fig. 3.6(a)), width W (Fig. 3.6(b)), height h (Fig. 3.6(c)) of the wire, and the refractive index of the surrounding medium n (Fig. 3.6(d)) are demonstrated. While one parameter was varied, the others were held constant at $L = 250$ nm, $W = 150$ nm, $h = 40$ nm, and $n = 1$. The period of the structures was $P = 500$ nm. The positions of the plasmon resonances were assumed to correspond to the minima of the transmittance presented in the diagrams. According to the formula for a metallic ellipse, the resonance frequency increases with a decrease of the aspect ratios L/W or L/h and decreases by increasing the refractive index of the surrounding medium. Thus, the plasmon resonance of a cut-wire can be tuned in a broad spectral region by changing its geometry and the refractive index of the surrounding medium.

In the case of double cut-wires the critical parameter for the control of the reso-

metal	ϵ_{inf}	ω_p [eV]	γ [eV]
Gold	6.9	8.9	0.07
Silver	3.7	9.2	0.02

Table 3.1: Drude model parameters for gold and silver from Ref. [75]
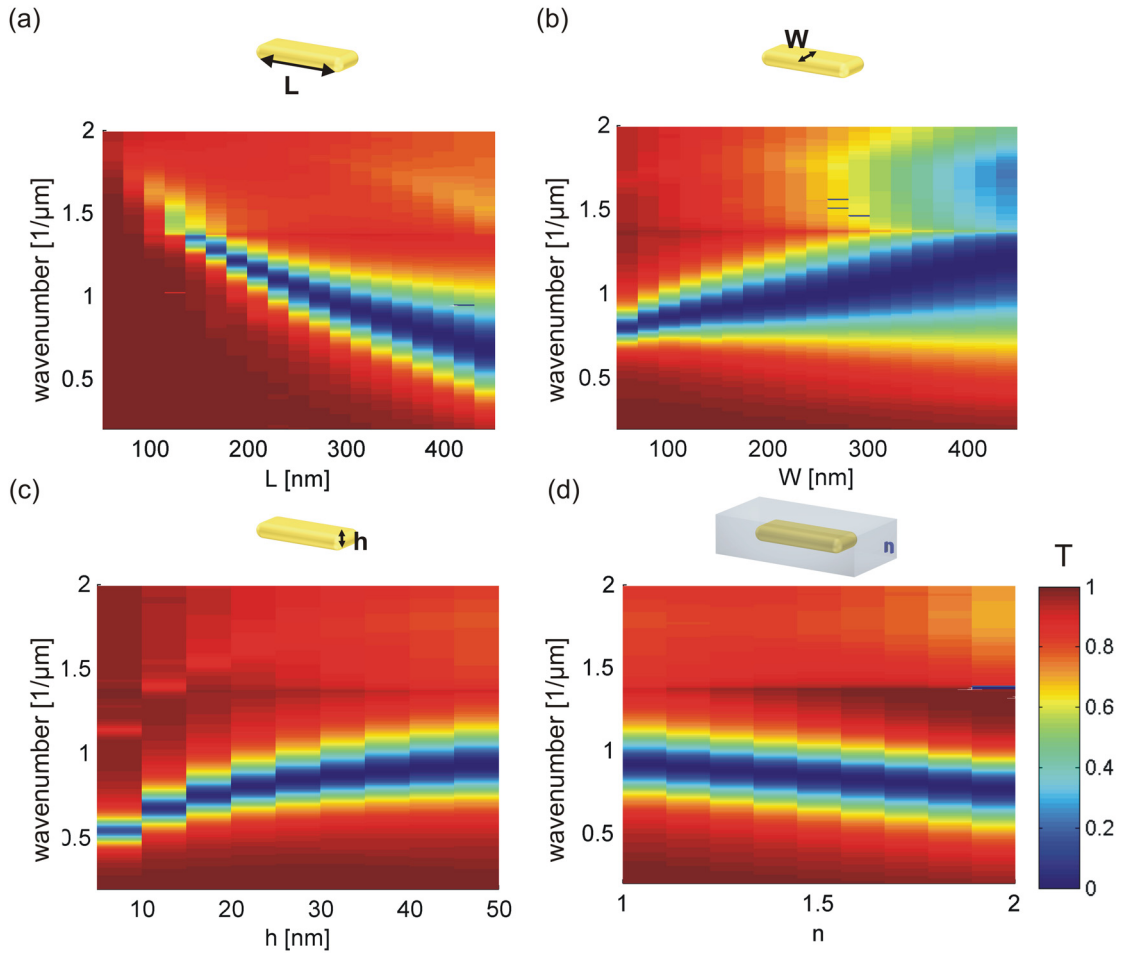
Figure 3.6: Transmittance of single layers of gold cut-wires as a function of the (a) - length , (b) - width, (c) - height of the wires, and (d) - refractive index of the surrounding medium. The electric filed of the exiting wave is parallel to the longest side of wires.

nance positions becomes the distance d between the cut-wires. This spacer thickness defines the strength of the coupling and hence the splitting of the symmetric and antisymmetric modes. The positions of the symmetric and antisymmetric resonances can be identified taking into account their radiation properties in the transmittance, reflectance, and absorbance spectra, which are shown in Fig. 3.7(a)-(c). The excitation of the symmetric resonance (wavenumbers 1.4 μm^{-1} - 1.6 μm^{-1}), associated with a charge distribution with a high dipole moment and as a result a high radiation ratio [65], causes increased reflection of the MM. The antisymmetric resonance, in turn, appears as the maximum in absorption (wavenumbers 0.2 μm^{-1} - 0.8 μm^{-1}) and the minimum in transmittance, which in this case results from the high quadrupole moment of the charge distribution having a low-radiating character [60, 65]. The positions of the symmetric and antisymmetric resonances are marked with white dots in the spectra in Fig. 3.7. One can see that the energy
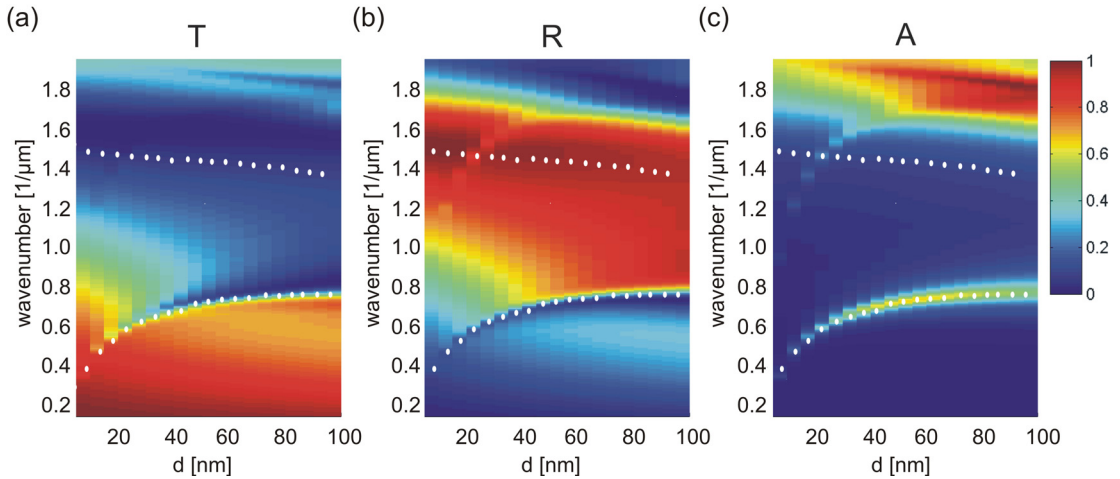
Figure 3.7: (a) - Transmittance, (b) - reflectance, and (c) - absorbance of the cut-wire structures as functions of frequency and spacer thickness d. Positions of the symmetric and antisymmetric resonances are marked with the white dots.

level splitting of the corresponding modes becomes smaller with the growth of the distance d. This means that the coupling between the cut-wires becomes weaker.

However, the high absorbance at the antisymmetric resonance for the structures with large d means that this resonance becomes stronger. Increasing the distance between the cut-wires intensifies the asymmetry of the electric field exciting the plasmon oscillations in the cut-wires and thus causes the improvement of the excitation condition for the antisymmetric mode.

The presented analysis of the resonance behavior of cut-wires has been done for the configurations including only one constitutive element (single or double cut-wire). Obviously, the combination of the elements (continuous wires and cut-wires) in a unit cell can lead to an interaction between them [110, 120]. The simulations show that for tightly packed unit cells the positions of the resonances slightly shift relative to the ones calculated for single element configurations. This shift can be explained by the change of the effective refractive index of the surrounding medium for a cut-wire embedded in the effective medium composed of continuous wires. Therefore, an additional tuning of the geometry of the constitutive elements is required for the final optimization of the unit cell of a NIM with continuous wires and cut-wires.

3.2.3 Design procedure

The general rules for the design of a double element NIM can be formulated as follows. The amount of metal in the unit cell has to provide a negative ϵ'_{eff} at the wavelength of interest. By tuning the height and the width of the continuous wires,

the required value of ϵ'_{eff} can be achieved. However, the more metal is present in the unit cell, the higher are the losses and the lower is the FOM of the NIM.

To increase the FOM of the NIM, μ'_{eff} should be possibly negative in the spectral range of interest. Therefore, the strength of the antisymmetric resonance should be maximized. This can be realized by improving the excitation condition for the resonance, that is increasing the distance d between the cut-wires. Additionally, as the host medium possesses $\mu = 1$, the concentration of the cut-wires should be high enough to provide $\mu'_{\text{eff}} < 0$.

The design of a double element NIM at a certain wavelength λ_{n} in the NIR spectral range begins with the configuration of an initial layout, which is further optimized using numerical simulations. The development of the initial design includes the following steps.

1. The choice of the metal for the continuous and cut-wires using the instructions summarized in Sec. 3.2.1.

2. The initial parameters of the cut-wires should be chosen according to the general considerations. Taking into account the quality of the thin metallic films, the start height h of the cut-wires can be taken to be about $20\,\text{nm}$. As the typical period of the structures for NIR range is several hundreds of nanometers, the start width W can be about $150\,\text{nm}$. The material of the dielectric spacer for the double cut-wires should be chosen according to the fabrication facilities. The thickness of the dielectric spacer d should be large enough to provide the excitation of the antisymmetric mode of the system. However, it should be small enough to ensure the fulfillment of the condition of the effective medium. For a dielectric with a refractive index of 1.5 the start value of d can be $30\,\text{nm}$ according to calculations presented in Sec. 3.2.2.

3. The length L of the cut-wires has to be estimated to provide the antisymmetric resonance at λ_{n}. This can be done using the results presented in Sec. 3.2.2.

4. The width of the long wires has to be enough to provide $\epsilon'_{\text{eff}} < 0$ at λ_{n}.

5. After the length of the cut-wires is fixed, the period of the structure can be determined. The smaller the period of the structure the higher the concentration of the double cut-wire elements can be. In the direction along the cut-wires, to prevent an interaction between the cut-wires of the neighboring cells, the distance between them should be kept at about $100\,\text{nm}$. This, in turn, determines the minimal period in this direction. The main criterion for the period in the other direction is the sufficient concentration of the metal in the form of continuous wires. The larger the period the wider the wires can

be, and a more negative ϵ_{eff} can be realized. However, the period should be small enough to prevent diffraction effects at λ_{n}.

6. After a preliminary configuration of the unit-cell is designed, the numerical optimization process can be started. Using a scan of all the parameters the optimal design providing the negative refractive index at λ_{n} with the maximal FOM can be realized.

The optimization of the geometry of the unit-cell of a NIM requires the knowledge of the facilities and limitations of the fabrication process, which is discussed in the following section.

3.3   MM sample fabrication

The process for MM fabrication involves electron-beam lithography, vacuum evaporation, a lift-off process, and ion-beam etching. The double element NIMs were produced using a layer-by-layer technology, where each layer of the structure was fabricated within one lithographic step[1] [121]. This technique allowed for the fabrication of structures with variable lateral geometries in each layer and therefore was used to realize the asymmetric double cut-wire structures discussed in Sec. 5. However, the fabrication of a metal-dielectric-metal stack in one run is free of alignment errors and a more efficient approach in the case of symmetric metamaterials. Such a "one-step" technique with one lithographic step [122] was employed for the realization of the symmetric fishnet NIMs [2] used for the verification of experimental technique presented in chapter 4.

In Fig. 3.8 the main steps of the layer-by-layer fabrication process are presented. All investigated samples were fabricated on 4" SiO_2 wafers with a typical sample size of 2 mm x 2 mm. The fabrication started with the spin-coating of a thin two layer lift-off resist (85 nm ARP671 on 85 nm ARP610). To avoid charging effects during the electron-beam exposure, a gold film (2 nm thick) was evaporated on the top of the resist. The exposure of the resist was done with the shaped electron beam writer SB350 OS (50 keV, Vistec Electron Beam GmbH). After exposure and removal of the thin gold layer the resist was chemically developed (30 s in MIBK: IPA = 1:1). A gold film with a thickness according to the design was evaporated on the resist mask. Performing the lift-off procedure, the first layer of a NIM was

---

[1]The sample fabrication using the layer-by-layer technology was conducted by Dr. Uwe Hübner from the Institute of Photonic Technology, Jena.

[2]The sample fabrication using the "one-step" technique was performed by Dr. Christian Helgert from the Institute of Applied Physics, FSU Jena.
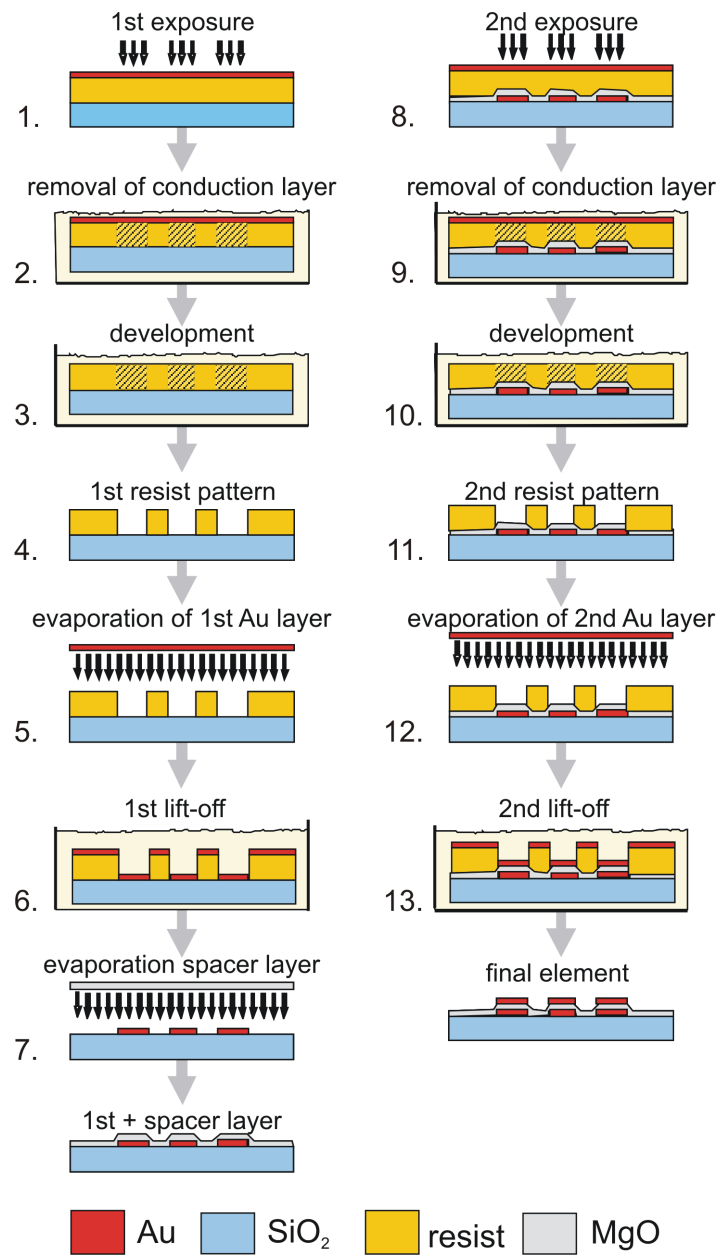
Figure 3.8: Fabrication of a double cut-wire based metamaterial with the layer-by-layer technology.

realized. To provide the lateral alignment of this layer relative to the ones deposited in the following processing steps, alignment marks were written in the first layer.

Further, a spacer layer made of MgO on top of the first structured Au layer was fabricated with a vacuum evaporation process. The second structural Au layer was fabricated in analogy with the first one using the alignment marks for the arrangement. The measured lateral alignment error between the first and second structural Au layers was less than 20 nm within the 2 mm x 2 mm area of the samples. The used manufacturing process imposed limitations of the lateral geometry of the structures. To provide the mechanical stability of the resist mask, the minimal distance between double wires and cut-wires was limited to 120 nm.

In contrast to the layer-by-layer technology, in the "one-step" approach the three layers of a structure (metal - dielectric - metal) were processed simultaneously in one lift-off process. The steps 1-4 were conducted in analogy to the previously described method. In step 5, the three layers were evaporated one by one and after the lift-off procedure the complete structure was realized. As a result the perfect alignment of both gold layers could be achieved. However, the anisotropy of the evaporation process caused a trapezoidal form of the walls of the mask. For the stack consisting of 20 nm gold, 40 nm MgO, and 20 nm gold, the resulting angle in the profile of the fishnet structure was about 11°.

3.4 Evaluation of the experimental technique

3.4.1 Topographical characterization of the fabricated structures

After the fabrication, the geometry of the samples was controlled by means of atomic force microscopy (AFM) and scanning electron microscopy (SEM). The SEM top view images (an example is shown in Fig. 3.9(a) and (b)) were used for the measurements of the lateral dimensions of structures. The accuracy of the lateral parameter definition was about 6 nm. The lateral alignment of the layers and their quality could be controlled by "cutting" the structure with a focused ion beam (FIB) and imaging of the profile with the SEM (see Fig. 3.9(c) and (d)).

The surface roughness and the thickness of the layers were controlled with AFM measurements with an accuracy of about 1 nm - 2 nm. An AFM image of the surface of a double element MM is shown in Fig. 3.10(a), the profile curves corresponding to the lines marked in Fig. 3.10(a) are shown in Fig. 3.10(c). Though AFM is the most precise method to measure the layer thickness, the profile scans obtained for the
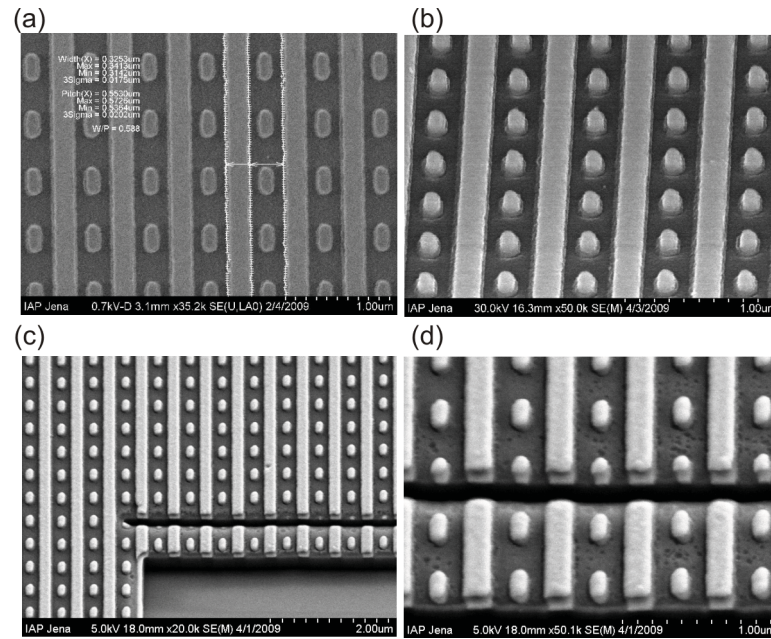
Figure 3.9: The SEM images of the double element metamaterials: (a) - top view, (b) - tilted view, (c) - tilted view of the focused ion beam cut, (d) - the same as in (c), zoomed.
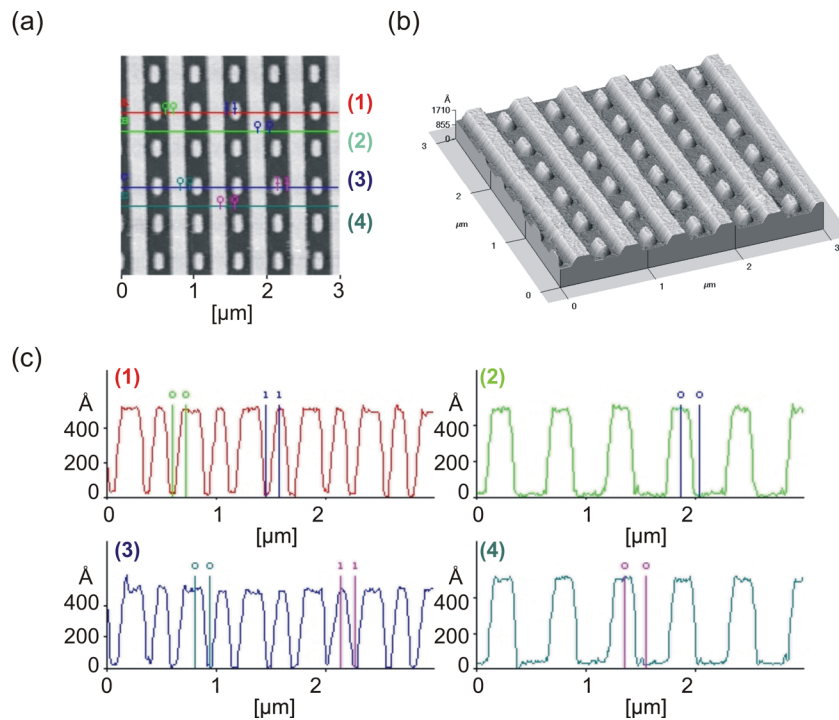

Figure 3.10: AFM images of a double element metamaterial: (a) - top view, (b) - 3D reconstruction of the surface, (c) - height profiles along the lines marked with (1), (2), (3), (4) in the top view.
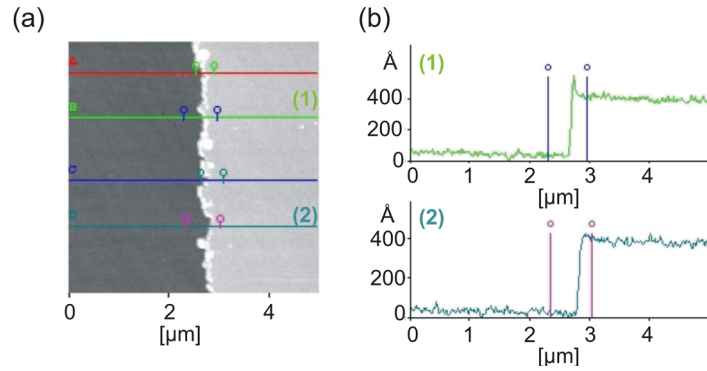
Figure 3.11: (a) - a top view of a reference field on a MM sample, (b) - step profile of the second gold layer.

double continuous and cut-wire structures required careful interpretation. A small period of the structure and nanoscale feature sizes prevented the AFM tip to resolve the profile. The measured height of the structure consisting of 40 nm gold, 40 nm MgO, and 40 nm gold layers was only 40 nm. Accounting for the MgO layer forming the ground level, the measured thickness had to be about 80 nm. Therefore, to ensure accurate measurements of the layer thicknesses, reference fields were created using spacial masks during the fabrication (see Fig. 3.11).

3.4.2   Characterization of the MgO layers

To investigate the homogeneity of the MgO layers fabricated with the electron beam evaporation process, a set of samples was produced. MgO layers with thicknesses of $d_{\mathrm{ini}} = 500\,\mathrm{nm}$, $400\,\mathrm{nm}$, $100\,\mathrm{nm}$, $50\,\mathrm{nm}$, $40\,\mathrm{nm}$, $30\,\mathrm{nm}$ were arranged on two wafers as it is shown in Fig. 3.12(a) and (b). The thicknesses of the layers (d_i) were measured with AFM at the edges formed by the MgO layers and the substrate in the points marked with the black strokes (see Fig. 3.12) separated by a distance of 2.5 mm.
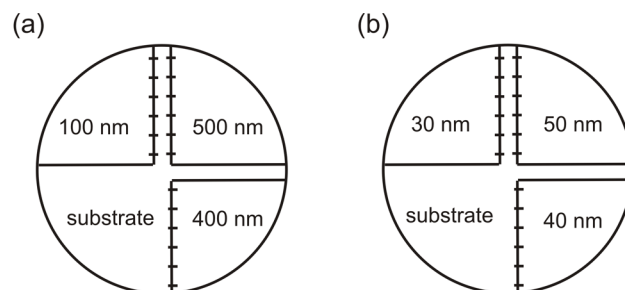

Figure 3.12: (a), (b) - layout of the test MgO layers.

The averaged thicknesses of the layers

$$d_{\text{avg}} = \frac{1}{6} \sum_{i=1}^{N=6} d_i \qquad (3.2)$$

are presented in the second column of Tab. 3.2. For thin layers the deviations $d_{\text{s}} = d_{\text{ini}} - d_{\text{avg}}$ were below 4 nm. The random deviation of the layer thicknesses from the average values along the measured direction

$$d_{\text{r}} = \frac{100}{d_{\text{avg}}} \sum_{i=1}^{N=6} |d_{\text{avg}} - d_i|/6 \qquad (3.3)$$

were below 5 % which is the state-of-the-art for the evaporation process.

In Fig. 3.13(a) and (b) the measured transmittance and reflectance for the MgO layer with $d_{\text{ini}} = 400$ nm are shown with the red curves. The spectra for the layer with $d_{\text{ini}} = 500$ nm are presented in Fig. 3.13(c) and (d). According to Ref. [123] the transmittance and reflectance through a thin film (n_2) on a substrate (n_3) in a homogeneous environment (n_1) (the arrangement is shown in Fig. 3.13(e)) are

$$T_{\text{th}} = \frac{|t_{123}|^2 |t_{31}|^2 \exp(-2Im[\delta_S])}{1 - |r_{321}|^2 |r_{31}|^2 \exp(-4Im[\delta_S])}, \qquad (3.4)$$

$$R_{\text{th}} = |r_{123}|^2 + \frac{|t_{123}|^2 |r_{31}|^2 |t_{321}|^2 \exp(-4Im[\delta_S])}{1 - |r_{321}|^2 |r_{31}|^2 \exp(-4Im[\delta_S])}, \qquad (3.5)$$

$$t_{123} = \frac{t_{12} t_{23} \exp(i\delta)}{1 + r_{12} r_{23} \exp(2i\delta)} \qquad (3.6)$$

$$r_{123} = \frac{r_{12} + r_{23} \exp(2i\delta)}{1 + r_{12} r_{23} \exp(2i\delta)} \qquad (3.7)$$

$$\delta_{(S)} = \frac{2\pi}{\lambda} d_{(S)} \sqrt{n_{(S)}^2 - sin^2\phi}, \qquad (3.8)$$

where t_{ij} and r_{ij} are Fresnel's coefficients for transmission and reflection on the

d_{ini}	d_{avg}	d_{s}	d_{r}
500 nm	561 nm	61 nm	8%
400 nm	460 nm	60 nm	9.3%
100 nm	109 nm	9 nm	7.5%
50 nm	47.6 nm	2.4 nm	4.8%
40 nm	37.5 nm	2.5 nm	3.2%
30 nm	31.5 nm	1.5 nm	2.8%

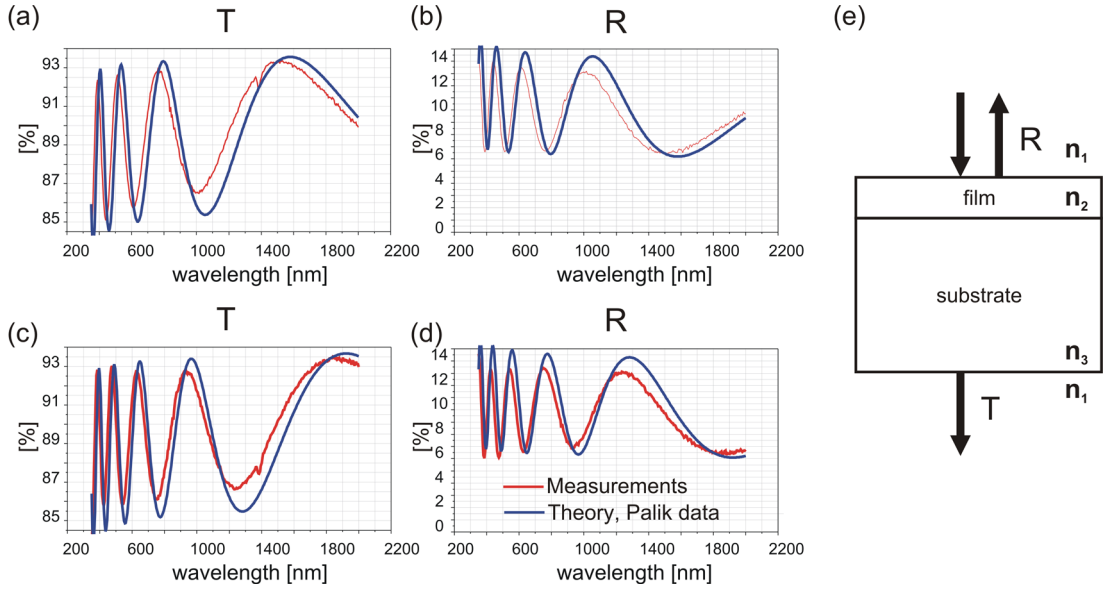Table 3.2: Systematic and random deviations of the thicknesses of MgO layers

Figure 3.13: (a),(b) - Transmittance and reflectance of the MgO layer with d_{ini}=400 nm. (c),(d) - Transmittance and reflectance of the MgO layer with d_{ini}=500 nm. The red curves show the measured data and the blue the simulated ones done using measured d_i and refractive index for MgO from [76]. (e) - An arrangement of a thin film on a substrate.

interface between media i and j and ϕ is the angle of incidence. The transmittance and reflectance spectra, calculated with Eqs. (3.5) and (3.6) using the refractive index of MgO from Ref. [76] and measured d_{i} are shown in Fig. 3.13 with blue lines. Comparison between the measured and calculated spectra leads to the conclusion that the refractive index of the fabricated layers differs from the one published in Ref. [76].

To assess the refractive index of the fabricated MgO layers, two methods were applied. The first method ("T method") is based on the measurements of the transmittance from thick MgO layers ($d_{\mathrm{ini}} = 500$ nm and $d_{\mathrm{ini}} = 400$ nm) placed on a thick substrate and the definition of the refractive index n_{MgO} by the wavelengths of the interference minima [124]. The basic equation for interference fringes occurring in a layer of thickness d and a refractive index n_2 is

$$2n_2d = m\lambda, \tag{3.9}$$

where λ is a wavelength and m is an integer number. The transmittance of the system at the wavelengths of the interference minima, under the assumption of coherent interaction of the light with the MgO film and incoherent interaction with the thick substrate, according to Ref. [124] is

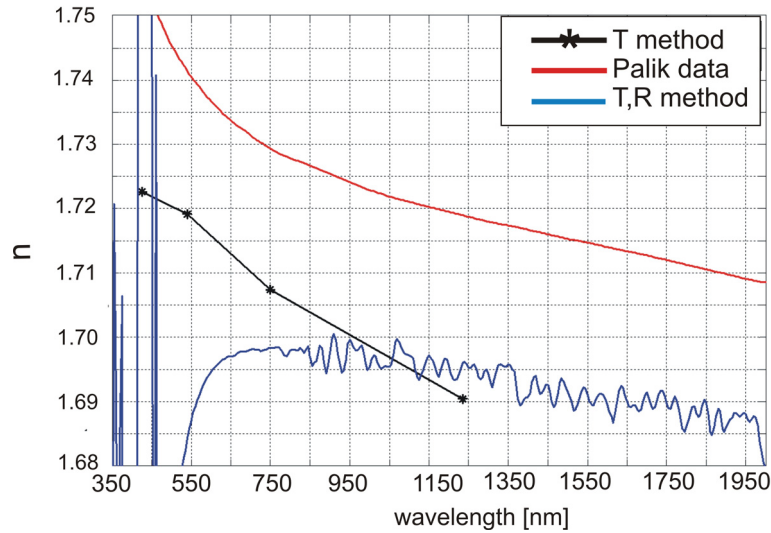$$T_m = \frac{4n_2^2 n_3}{n_2^4 + n_2^2(n_3^2 + 1) + n_3}. \tag{3.10}$$

46

Figure 3.14: Refractive index of MgO.

where n_3 is the refractive index of the substrate. The transmittance at the wavelengths of the interference maxima is

$$T_M = \frac{2n_3}{n_3^2 + 1} \tag{3.11}$$

and can be used to calculate the refractive index of the substrate. The refractive index n_2, in turn, can be found as

$$n_2 = [M + (M^2 - n_3^2)^{1/2}]^{1/2}, \tag{3.12}$$

where

$$M = \frac{2n_3}{T_m} - \frac{n_3^2 + 1}{2}. \tag{3.13}$$

The expression for the refractive index does not contain the thickness of the layer d. Thus, the advantage of the method lies in the fact that the accuracy of the refractive index definition depends only on the accuracy of the transmittance measurements, which was $\pm 0.3\%$. Correspondingly, the accuracy of the refractiv index definition for n_{MgO} shown in Fig. 3.14 with black stars was $\Delta n = \pm 0.005$. However, the refractive index of MgO could be defined only for a few discrete wavelengths corresponding to the interference minima. Measurements on thicker samples, in turn, would be inconsistent, due to the difference of the optical properties of thin and thick layers. The second method ("T,R method") [125,126] used for the refractive index definition is based on the measurements of the transmittance (T_{exp}) and reflectance (R_{exp})

of a MgO layer and calculation of the refractive index by solving the following optimization problem

$$T_{\mathrm{th}}(n, d, \lambda) - T_{\mathrm{exp}} = 0, \tag{3.14}$$

$$R_{\mathrm{th}}(n, d, \lambda) - R_{\mathrm{exp}} = 0, \tag{3.15}$$

where T_{th} and R_{th} are theoretically calculated transmittances and reflectances (Eqs. (3.5) and (3.6)) at the wavelengths λ and d is the thickness of the layer.

In the case of normal incidence ($\phi = 0$), simultaneous optimization of the refractive index n and the layer thickness d fails for a transparent material because these two parameters enter as the combination dn in all analytical formulas for T_{th} and R_{th} (see Eq. (3.5)). Using d_i measured with the AFM, the fitting of the refractive index could be conducted (see the blue curve in Fig. 3.14). Using the error calculation formula for n from Ref. [125] the accuracy of the refractive index measurements was ± 0.007. The comparison of the refractive indices obtained by the two presented methods with the one from Ref. [76] has shown that the refractive index of MgO is influenced by the fabrication process. The measured difference between the measured and literature data was about 2%. Therefore, in the design of NIMs the measured refractive index of MgO from the "T,R method" were used.

3.4.3   Characterization of the gold layers

The characterization of the dielectric functions of the thermally evaporated thin gold films was conducted firstly for unstructured thin gold films. A set of thin gold films with thicknesses $d_{\mathrm{Au}} = 10\,\mathrm{nm}$, $25\,\mathrm{nm}$, $35\,\mathrm{nm}$, and $45\,\mathrm{nm}$ was produced using a thermal evaporation process. Measurements with AFM have shown that the roughness of the layers was between $2\,\mathrm{nm}$ and $4\,\mathrm{nm}$ and the thickness of the films were met with an accuracy of $\pm 1\,\mathrm{nm}$. The comparison of the measured and simulated transmittance and reflectance spectra using ϵ_{Au} from Ref. [75] have shown an agreement within 2%. In Fig. 3.15 an example is presented where the measured spectra for a gold layer with the nominal thickness $d = 25\,\mathrm{nm}$ are shown with black lines and the spectra for a gold layer with a thickness of 26 nm (providing the best agreement of the spectra) calculated using $\epsilon_{\mathrm{Au}}(\omega)$ from Ref. [75] are presented by the red lines.

The material properties of the structured films were investigated on single layers of structures consisting of continuous wires and cut-wires. Such a single layer structure, on the one hand, is a rather simple object for the numerical and experimental characterizations. On the other hand, it bears all characteristic traits of the man-
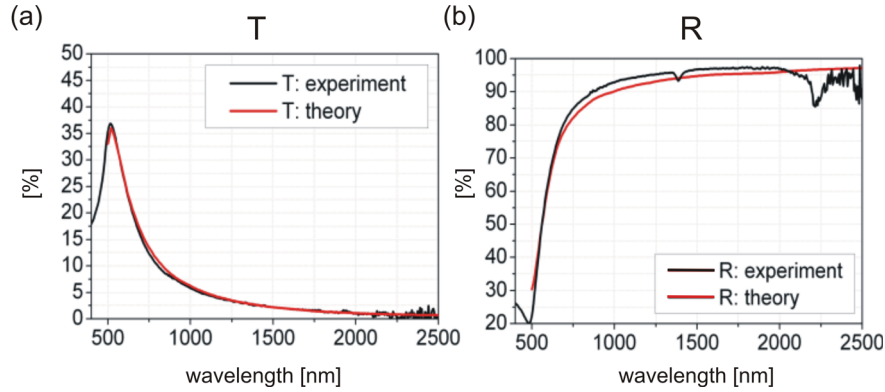
Figure 3.15: (a) - Transmittance and (b) - reflectance of a gold layer with $d = 25\,\text{nm}$. Black and red curves show the measured and simulated spectra, respectively.

ufacturing process which causes imperfectness of the crystallographic structure and the increase of the surface roughness. For the numerical simulations, the geometry of the manufactured structures was reconstructed using the SEM images.

As it was discussed in Sec. 2.2.3, the effects of the imperfectness of the structured surfaces can be taken into account by increasing the imaginary part of the dielectric function for an unstructured thin layer $\epsilon_{\text{Au}} = \epsilon'_{\text{Au}} + ig\epsilon''_{\text{Au}}$ from Ref. [75]. Simulated spectra of a single layer structure for different values of the multiplication factor ($g = 1, 3, 4$) for the imaginary part of the dielectric function ϵ''_{Au} are shown in Fig. 3.16(a),(b), and (c). The comparison between the measured and simulated spectra has shown that for wavelengths above the resonance the best agreement between measured and simulated spectra is achieved for the case of $g = 2$. In the resonance (wavelengths around $1\,\mu\text{m}$), in turn, simulated spectra done using $g = 4$ provide the best correspondence to the measured ones. The best fitting of the measured spectra achieved by a variation of g with the wavelength in the range from 1 to 4 is shown in Fig. 3.16(d),(e), and (f). Thus, the effect of the roughness and crystallographic structure imperfectness can be approximately accounted for by introducing a multiplying factor for ϵ''_{Au} which in general depends on the wavelength.

However, a fine tuning of the wavelength dependence of the imaginary part of the dielectric function ϵ_{Au} in the numerical simulations is time consuming. Additionally, the effects of geometry deviations are more pronounced, which was also demonstrated in investigations done by other groups [89, 90, 127, 128]. Hence, for the sake of simplicity, in the simulations the dielectric function for gold was taken from Ref. [75], while the imaginary part of gold was assumed to be $2\epsilon''_{Au}$.
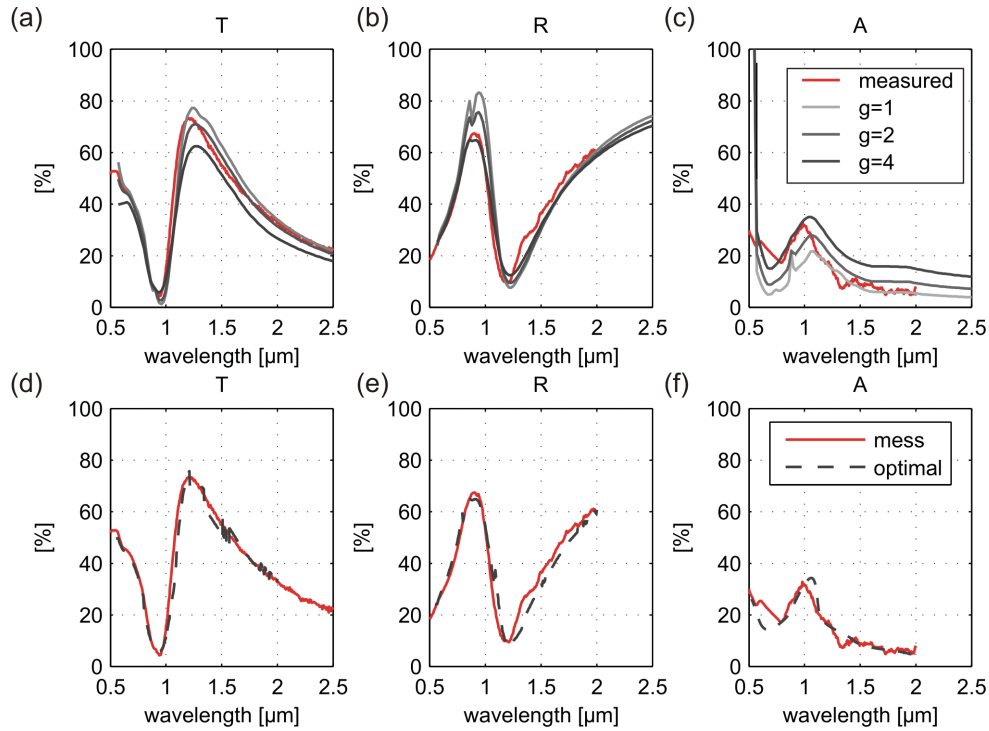
Figure 3.16: (a),(d) - Transmittance, (b),(e) - reflectance, and (c),(f) - absorbance of a layer of continuous and cut-wires. The measured spectra are shown with red lines. In (a)-(c) - simulated spectra obtained using different values of the multiplication factor g for the imaginary part of the electric permittivity are shown with gray lines. In (e)-(f) - the simulated spectra were obtained using $g(\lambda)$.

3.5 Influence of fabrication inaccuracies

Since the fabrication of nanostructures is still a challenging technological task, the investigation of the sensitivity of the MM's optical properties to distortions of the unit cell geometry is essential for the development of a realizable design. Additionally, as it was discussed in Sec. 2.3.3, the effective parameters of a produced MM can be obtained from the numerical simulations, if the simulated and measured far field spectra show a good agreement. The achievement of a good agreement, in turn, requires a fitting of the unit cell geometry, which can be facilitated by the investigation of the accuracy with which the geometry can be realized.

The most pronounced deformation of the structure occurring during the fabrication and revealed with SEM images is the rounding of the edges of the cut-wires. In Fig. 3.17 the effect of the rounding on the resonance position and the effective permittivity is demonstrated for a structure with a period $P = 500$ nm, a length $L = 250$ nm, a width $W = 150$ nm, and a height $h = 40$ nm. The rounding causes damping and a blue shift of the order of 150 nm of the resonance.

Further imperfections occurring due to the technological inaccuracy are devia-
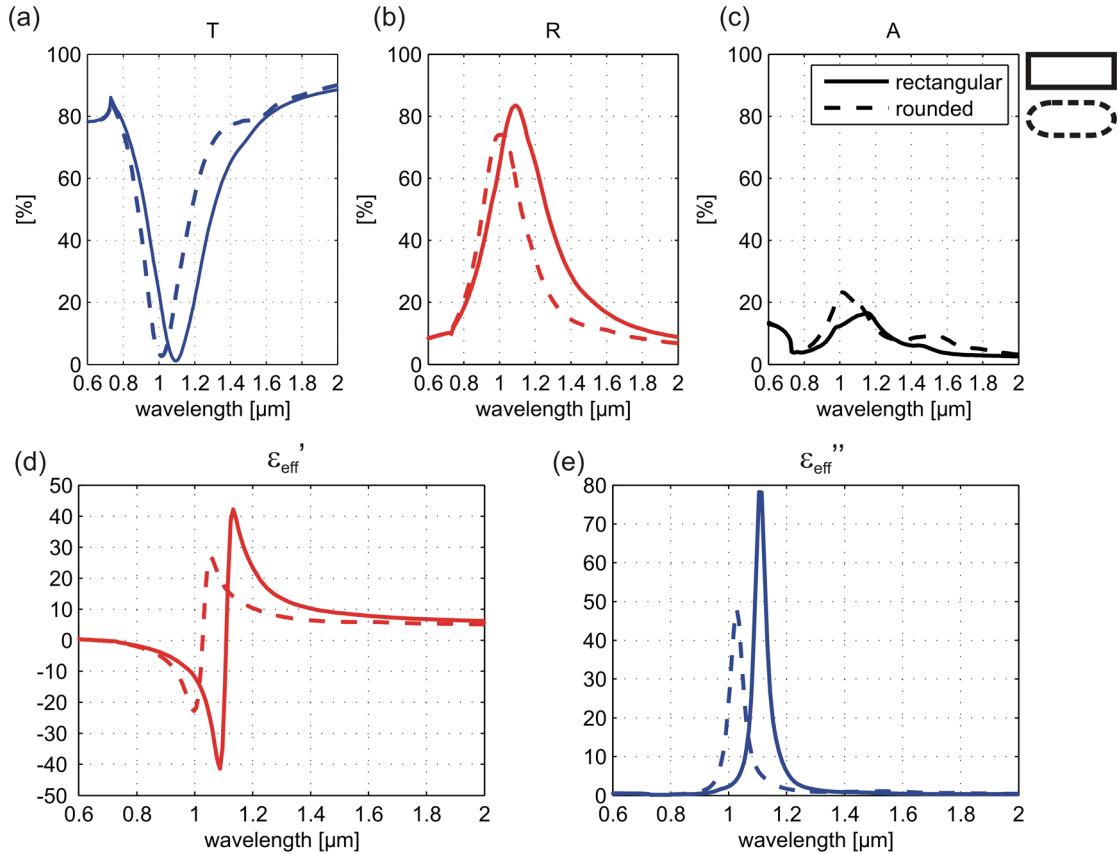
Figure 3.17: (a) - Transmittance, (b) - reflectance, (c) - absorbance of a layer of cut-wires of rectangular and rounded shapes. (d) - The real and (e) - the imaginary parts of the effective permittivity of the effective medium.

tions of the spacer thickness d, the lateral dimensions of the structures L and the misalignment of the layers s. Information on the technological tolerances were collected from SEM and AFM images of a series of structures and summarized in Tab. 3.3. The dependencies of the spectral positions of the symmetric and antisymmetric resonances on the slight deviations of d, s, and L are presented in Fig. 3.18. The positions of the symmetric and antisymmetric resonances were associated with the maximum of the reflectance and the absorbance, respectively. The symmetric resonance appears as a broad spectral feature, due to high radiation losses, which makes its localization ambiguous. Maximal deviations of the geometry, within the limits of the technological tolerances, result in a shift of the antisymmetric resonance of up to 100 nm. According to the data in Fig. 3.18, the symmetric resonance reacts

Δd	ΔS	ΔL
$\pm 2.5\,\text{nm}$	$\pm 20\,\text{nm}$	$\pm 10\,\text{nm}$

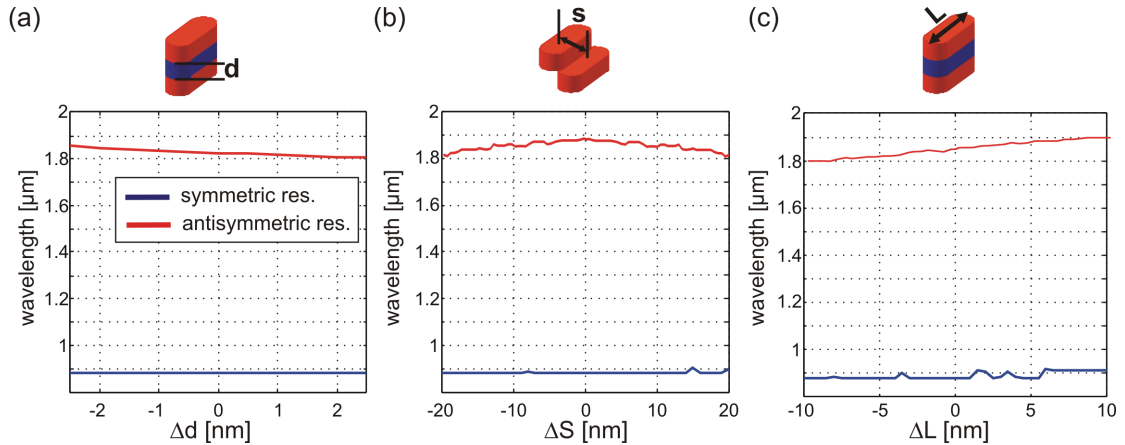Table 3.3: Tolerances of the fabrication process

51

Figure 3.18: Dependency of the spectral positions of the symmetric and antisymmetric resonances of a double cut-wire as a function of the technological tolerances of (a) - the spacer thickness, (b) - the lateral alignment, and (c) - the length of the wires.

less sensitive to the geometry variation. However, this is the consequence of the low accuracy of the definition of the resonance position.

The analysis of the influence of the refractive index of the dielectric spacer on the resonance position of the antisymmetric resonance λ_0 has shown that the refractive index has to be known with precision of 0.02 to provide localization of the resonance better than 10 nm.

In short, numerical simulations reveal that the spectral position of the antisymmetric resonance may experience a shift of up to 100 nm due to deformation of the geometry of the unit cell within the limits of the technological tolerances. It is important to note that variations of different parameters may result in the same spectral behavior of the resonances (see Fig. 3.18). This ambiguity complicates the appropriate fitting of the geometry of the unit cell in the numerical simulations.

3.6 Double-element metamaterial with negative index

Due to technological reasons, the NIM samples based on continuous wires and cut-wires were designed for the near infrared region. The technological limitations forced the minimal distance between the cut-wires and continuous wires to be about 120 nm. This distance corresponds to the mechanical stability limit of the resist mask defined by the minimal width of the corresponding elements of the mask. Taking into account the limitations on the period of the structure, in order to satisfy the effective medium condition for the target wavelength of about 2 μm, the following structure was designed. The periods of the structure were $P_{\mathrm{x}} = 500$ nm
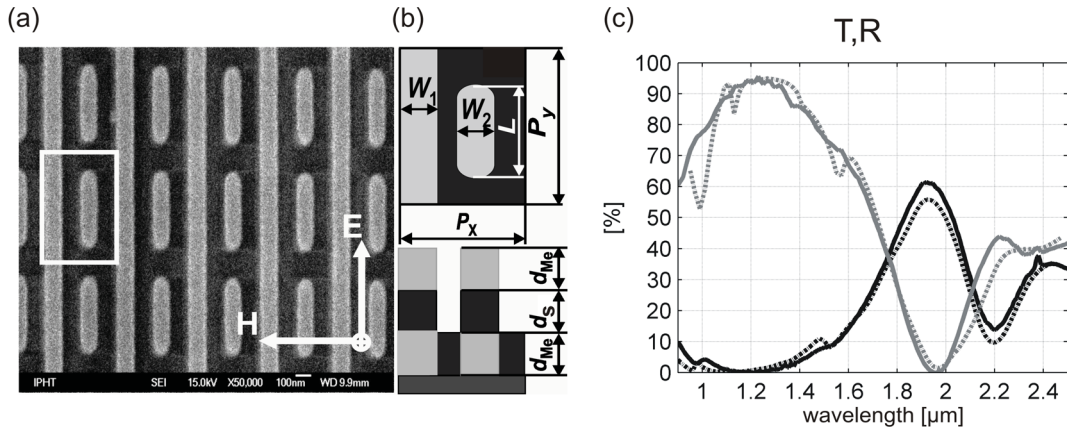
Figure 3.19: (a) - Top-view SEM image of the sample, the white rectangle shows the unit cell; (b) - unit cell geometry, top and side view in the upper and lower picture, respectively. (c) - Transmittance (black lines) and reflectance (gray lines) for the resonant polarization. Solid and dashed lines represent the measured and simulated spectra, respectively

and $P_y = 600$ nm. The width of the continuous wires was $W_1 = 130$ nm and of the cut-wires $W_2 = 100$ nm, the length of the cut-wires was $L = 430$ nm, the thickness of the metal layer $d_{Me} = 40$ nm and of the dielectric spacer $d_S = 40$ nm. The geometry of the unit cell with the respective parameters is shown in Fig. 3.19(a) and (b).

To a large extent the optical response of the double-element structures is determined by the plasmonic properties of the cut-wires. Resonances in the spectral domain of interest are only excited for an electric field polarization parallel to the cut-wires ("resonant" polarization).

In Fig. 3.19(c) the measured transmittance and reflectance of the realized structure are shown. The good quantitative agreement between simulated and measured spectra allowed us to calculate the effective material parameters of the fabricated samples using the combined method, taking advantage of the numerically simulated complex reflection and transmission coefficients. Resorting to the numerical simulations was required as the developed setup for the experimental measurements of the effective parameters of MMs was designed for the VIS and NIR spectral ranges (from $\lambda = 0.65$ μm to $\lambda = 1.7$ μm) and did not provide an access to the spectral range of interest. The retrieved effective parameters are presented in Fig. 3.20.

The main features of the transmission and reflection spectra for the resonant polarization can be interpreted using the calculated effective permittivity and effective permeability. In Fig. 3.19(c) it can be seen that the first minimum in transmission around $\lambda = 1.2$ μm is caused by the permittivity resonance (see Fig. 3.20(c)). In turn, a strong impedance mismatch causes a high reflection. The increase of transmission towards $\lambda = 1.9$ μm is caused by the fact that impedance and refractive
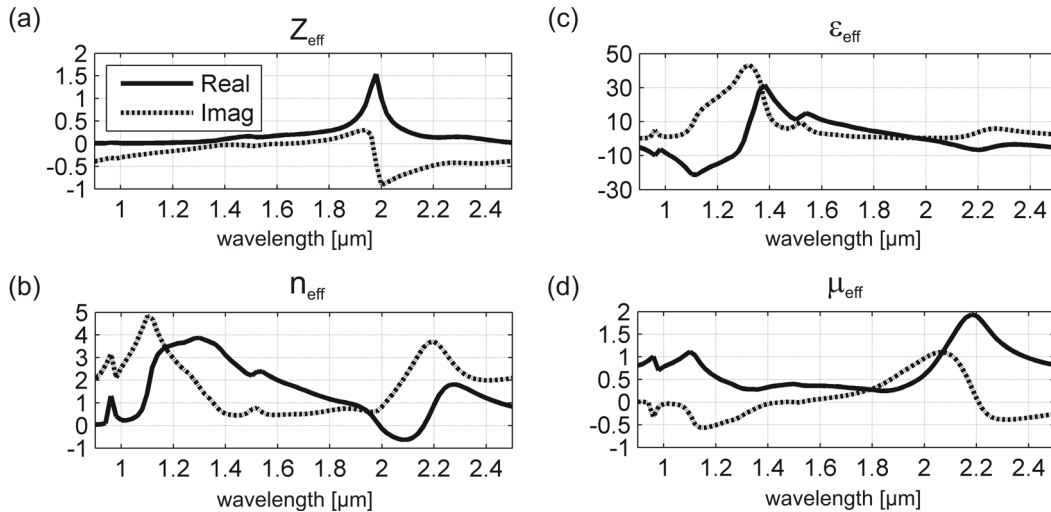
Figure 3.20: (a) - Impedance, (b) - refractive index, (c) - electric permittivity, (d) - magnetic permeability of the sample derived from the reflection and transmission spectra presented in Fig. 3.19(c).

index approach those of air. At $\lambda = 1.9\,\mu$m where the impedance is matched, the transmission reaches its maximum. The following decrease of transmission is caused by the excitation of the magnetic resonance. The transmission minimum near $\lambda = 2.2\,\mu$m corresponds to the maximum of the anti-symmetric resonance. The simulations show that a refractive index of $n = -0.5 + 1.9i$ at $\lambda = 2.1\,\mu$m and FOM $= 0.26$ has been achieved. The negative refractive index obtained with the double-element structure is a so called "single-negative" refractive index, which means that only the real part of the permittivity is negative. Even though the real part of the permeability remains positive, the NIM condition is met.

An improvement of the FOM of the NIM could be achieved by further tuning the unit cell geometry. In order to increase the strength of the anti-symmetric resonance, the period in P_x direction could be decreased or the width of the cut-wires could be increased. However, pushing the parameters of the structure to the technological limits results in decreasing the quality of the structures. Moreover, the simulations have shown that the real part of the permeability of the double-element structure optimized for a wavelength of about $1.5\,\mu$m and made of gold remains positive. In this case the metamaterial is single-negative and the FOM dose not exceed 0.8. A significant enhancement of the structure's FOM at the telecommunication wavelength could be achieved by using silver instead of gold [27] due to silver's higher plasma frequency. Additionally, the geometry of the unit cell with separated elements offers the advantage that further optimization of the magnetic response can be achieved by breaking the vertical symmetry of the cut-wires (see chapter 5).

Chapter summary

In this chapter the design of the effective material parameters of NIMs using plasmonic nanostructures was discussed. It was demonstrated how the dielectric function of a NIM can be designed by adding metal in the form of continuous wires in its unit cell. The magnetic permeability of a NIM, in turn, can be affected by implementation of plasmonic double cut-wires supporting the antisymmetric mode associated with a magnetic moment. As a result, the combination of these two elements in the unit cell of a MM allows for the fulfillment of the NIM condition. Using numerical simulations, it has been shown how the frequency of the plasmonic resonances and as a result the target frequency where $n_{\mathrm{eff}} < 0$ can be tuned by varying the geometry of the plasmonic structures.

Further, the fabrication technology based on the electron-beam lithography and a lift-off process was presented and the main limitations of the processes were revealed. The study of thin MgO and gold layers was conducted to evaluate the fabrication accuracy regarding the thicknesses of the layers. The refractive index of fabricated MgO layers was determined using two approaches and the refractive index obtained by the "T,R method" was used for the further numerical simulations of NIMs. Additionally, it was shown that the dielectric function of fabricated gold nanostructures depends on the fabrication process. This dependence was accounted for by tuning the damping coefficient in the Drude-Sommerfeld model.

Using numerical simulations the sensitivity of the symmetric and antisymmetric resonances of a double-cut wire structure on the inaccuracy of the fabrication process was investigated. It was found that a variation of the parameters of the structure within the limits of the fabrication accuracy can cause a spectral shift of the antisymmetric resonance of up to 100 nm. Furthermore, simulations have shown that similar spectral shifts of the resonances can be caused by the variation of different parameters of the structure. As a result, this ambiguity prevents an accurate determination of the geometry of a fabricated structure using the comparison of the simulated and measured spectra. This, in turn, impairs the accuracy of the combined method for the determination of the MM's effective parameters.

The realization of a double-element metamaterial based on a combination of continuous wires and cut-wires has been demonstrated in the infrared region. The effective refractive index of the fabricated NIM, evaluated with the combined method, was $n = -0.5 + 1.9i$ at $\lambda = 2.1$ µm [129].

Chapter 4

Experimental method for the characterization of metamaterials

In this chapter an original experimental method for the measurements of complex transmission and reflection coefficients of a MM, required to evaluate its effective refractive index, is presented. The theoretical background of the white-light interferometric technique used for the phase measurements and the experimental setup are presented in the first section of the chapter. The experimental method was evaluated on two typical MMs: a plasmonic MM consisting of gold nanodisks (Sec. 4.2.1) and a fishnet NIM (Sec. 4.2.2).

Using the phase measurements a negative effective refractive index of a fishnet structure was experimentally verified. Furthermore, the experimental access to the phases of $t(\lambda)$ and $r(\lambda)$ allowed for the evaluation of the combined method usually used for the definition of $n_{\text{eff}}(\lambda)$. The accuracy of the methods is discussed in Sec. 4.2.3.

4.1 Experimental method

Spatial dispersion is the principal feature of MMs preventing the measurement of their optical properties using well established and precise methods developed for the characterization of thin films made of natural materials [123,130]. Due to the spatial dispersion inherent in MMs, their effective material parameters depend strongly on the angle of incidence. As a result, employing such a method as ellipsometry [130], combining the measurements of the far field response of a material performed under different angles of incidents, is prevented. Consequently, the development of an original method for the characterization of the effective material properties of MMs was necessary.
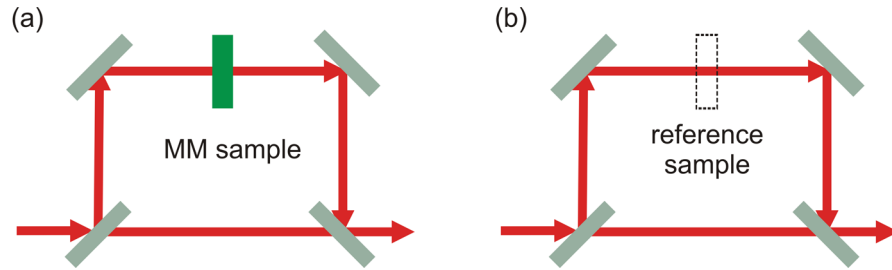
Figure 4.1: (a) - Illustrations of a MM and (b) - a reference sample arrangements in an interferometer during sample and reference measurements, respectively.

The general approach to assign effective parameters to the experimentally available MM films is similar to the one used for films made of conventional materials [131]. This approach described in Sec. 2.3.3 is based on the consideration of a single MM layer as an effective homogeneous one characterized by two complex effective parameters, namely the effective refractive index $n_{\text{eff}}(\lambda)$ and the effective impedance $z_{\text{eff}}(\lambda)$. According to Eq. (2.54) $n_{\text{eff}}(\lambda)$ for normal incidence can be retrieved from corresponding complex transmission $t(\lambda) = |t(\lambda)| \exp[i\phi_{\text{t}}(\lambda)]$ and reflection $r(\lambda) = |r(\lambda)| \exp[i\phi_{\text{r}}(\lambda)]$ coefficients.

While the measurements of the transmittance $T(\lambda) = |t(\lambda)|^2$ and reflectance $R(\lambda) = |r(\lambda)|^2$ can be realized using commercially available spectrometers, the phase measurements in transmission and reflection on thin films ($d < 100\,\text{nm}$) is still a challenging experimental problem. Therefore, an original experimental setup was developed for the phase measurements in transmission and reflection in the broad wavelength range from $\lambda = 0.65\,\mu\text{m}$ to $\lambda = 1.7\,\mu\text{m}$.

4.1.1 White-light spectral interferometry

The developed experimental method for the phase measurements is based on the white-light Fourier-transform spectral interferometric technique [132]. In this type of interferometric experiments a time delay τ is introduced between two beams of an interferometer using different geometrical lengths of its two arms (see Fig. 4.1). The complex transmission coefficients of the sample $t_{\text{sam}}(\omega)$ and reference $t_{\text{ref}}(\omega)$ arms of an interferometer can be written as

$$t_{\text{ref}}(\omega) = A_{\text{ref}}(\omega) \exp[i\phi_{\text{ref}}(\omega)],$$
$$t_{\text{sam}}(\omega) = A_{\text{sam}}(\omega) \exp[i(\phi_{\text{sam}}(\omega) + \phi_{\text{MM}}(\omega) + \omega\tau)], \quad (4.1)$$

where $A_{\text{ref}}(\omega)$ and $A_{\text{sam}}(\omega)$ are the amplitudes of the transmission coefficients. $\phi_{\text{ref}}(\omega)$ is the phase delay in the reference arm induced by dispersive optical ele-

ments placed in the arm. The phase delay in the sample arm is divided into three contributions: the term $\phi_{\text{sam}}(\omega)$ corresponding to the phase delay due to the dispersive optical elements, the term $\phi_{\text{MM}}(\omega)$ describing the phase delay in a MM sample, and the term $\omega\tau$ accounting for the geometrical length difference between the two arms. Therefore, the fields in each arm of the interferometer can be written as follows

$$
\begin{aligned}
E_{\text{ref}}(\omega) &= A_{\text{ref}}(\omega) \exp[i\phi_{\text{ref}}(\omega)] E_{\text{in}}(\omega), \\
E_{\text{sam}}(\omega) &= A_{\text{sam}}(\omega) \exp[i(\phi_{\text{sam}}(\omega) + \phi_{\text{MM}}(\omega) + \omega\tau)] E_{\text{in}}(\omega),
\end{aligned}
\tag{4.2}
$$

where $E_{\text{in}}(\omega)$ is the complex amplitude of the incident field. The interference of the fields $E_{\text{ref}}(\omega)$ and $E_{\text{sam}}(\omega)$ gives rise to the measured optical signal in the frequency domain

$$
\begin{aligned}
I(\omega) = |E_{\text{sam}}(\omega) + E_{\text{ref}}(\omega)|^2 &= \\
= |E_{\text{sam}}(\omega)|^2 + |E_{\text{ref}}(\omega)|^2 &+ \\
+ \, 2\, |E_{\text{sam}}(\omega)|\, |E_{\text{ref}}(\omega)| \cos(i(\phi_{\text{sam}}(\omega) &+ \phi_{\text{MM}}(\omega) + \omega\tau - \phi_{\text{ref}}(\omega))).
\end{aligned}
\tag{4.3}
$$

An example of the interference signal measured in the experiment (as a function of the wavelength) is shown in Fig. 4.2(a). The argument of the cosine function in the interference term contains the phase delay due to the MM sample $\phi_{\text{MM}}(\omega)$. Extraction of this interference term can be easily realized in the time domain. The signal in the time domain $S(t)$ obtained by Fourier transformation of $I(\omega)$ is

$$
\begin{aligned}
S(t) = FT\,[I(\omega)] &= \\
= E_{\text{sam}}(t) \otimes E_{\text{sam}}^*(-t) &+ E_{\text{ref}}(t) \otimes E_{\text{ref}}^*(-t) + \\
+ \, E_{\text{sam}}(t+\tau) \otimes E_{\text{ref}}^*(t) &+ E_{\text{sam}}^*(t-\tau) \otimes E_{\text{ref}}(t),
\end{aligned}
\tag{4.4}
$$

where $\otimes$ denotes the operation of convolution. In Eq. (4.4) the first two terms are the autocorrelation functions of the individual fields appearing as peaks at $t = 0$ in $S(t)$, which is shown in Fig. 4.2(b). The third and the fourth term in Eq. (4.4) are the correlation functions of two fields corresponding to the peaks at $t = \tau$ and $t = -\tau$ in Fig. 4.2(b). If the time delay τ is sufficiently large, the correlation and autocorrelation terms do not overlap and one of the correlation terms can be extracted by applying a finite time window. In the experimental realization of the method, the maximum value of the time delay τ is restricted, because τ is inversely
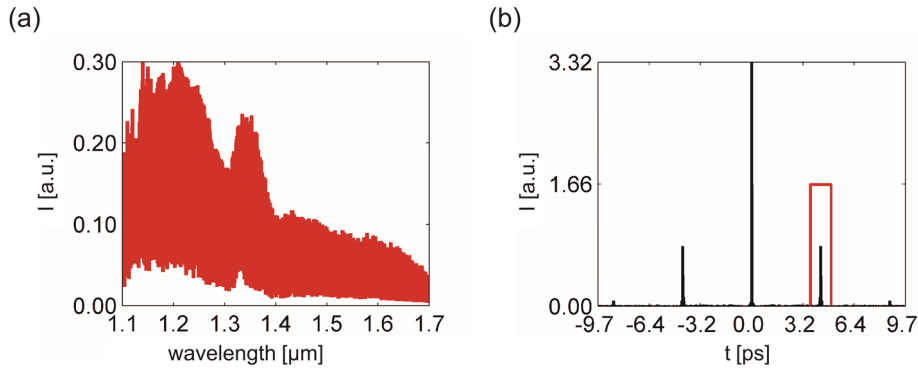
Figure 4.2: Intensity of the interference signal (a) - in the wavelength and (b) - in the time domain. The red rectangle in (b) represents a numerical filter used to separate the desired correlation term.

proportional to the period of the interference pattern

$$\Delta\nu = \frac{1}{c\tau}. \tag{4.5}$$

Here c is the light velocity in vacuum. Accordingly, large time delays correspond to small periods of the interference pattern and can make it impossible to fulfill the criterion of the Nyquist – Shannon sampling theorem [133] for the data sampling.

An example of a rectangular filter applied to $S(t)$,

$$\text{rect}(t, \tau, \delta\tau) = \begin{cases} 0, & t < \tau - \delta\tau \\ 1, & \tau - \delta\tau \leq t \leq \tau + \delta\tau \\ 0, & t \geq \tau + \delta\tau \end{cases} \tag{4.6}$$

is shown in Fig. 4.2(b). The inverse Fourier transformation of the signal after filtering gives the interference term in the frequency domain

$$E_{\text{int}}(\omega) = FT^{-1}\left[\text{rect}(t, \tau, \delta\tau)S(t)\right]. \tag{4.7}$$

The argument of the interference term is

$$\arg\left[E_{\text{int}}(\omega)\right] = \phi_{\text{sam}}(\omega) + \phi_{\text{MM}}(\omega) - \phi_{\text{ref}}(\omega) = \Delta\phi. \tag{4.8}$$

and represents the phase delay between the signals passing the two arms of the interferometer. The phase difference as given in Eq. (4.8) contains $\phi_{\text{MM}}(\omega)$ and the phase difference introduced by the dispersive elements in the arms of the interferometer. Therefore, a reference measurement is required for the extraction of $\phi_{\text{MM}}(\omega)$. For the reference measurement the MM sample is replaced with a reference sample (see Fig. 4.1(b)), for instance air in the case of transmission measurements or a

mirror in the case of reflection measurements. If $\phi_{\text{ref.sam.}}$ is the phase delay due to a known reference object, the phase difference measured and retrieved in the reference measurement is

$$\Delta\phi_{\text{ref}} = \phi_{\text{sam}}(\omega) + \phi_{\text{ref.sam.}}(\omega) - \phi_{\text{ref}}(\omega). \tag{4.9}$$

If the dispersion and thickness of the reference sample are known, $\phi_{\text{MM}}(\omega)$ can be extracted from Eqs. (4.8) and (4.9) as

$$\phi_{\text{MM}}(\omega) = \Delta\phi - \Delta\phi_{\text{ref}}(\omega). \tag{4.10}$$

In the general case the retrieved phase bears an ambiguity of 2π and additional information is required to obtain the absolute phase delay. The measured phase ϕ_{MM} of a single layer MM with thicknesses d less than 100 nm can be safely assumed to be $-\pi < \phi_{\text{MM}} < \pi$ at the wavelength of interest. For the retrieval of the effective parameters as outlined in Eq. (2.54) this implies that the assumption $m = 0$ is made. However, for thicker MMs made of a larger number of functional layers, cases where $m \neq 0$ have to be considered. Here, the choice of an appropriate value of m is made according to the knowledge of the refractive index at lower frequencies, where no resonances occur and a MM can be characterized with $\epsilon_{\text{eff}}(\omega)$ and $\mu_{\text{eff}}(\omega) = 1$. In this spectral range, one of the standard techniques developed for natural materials can be used [123] to determine the refractive index of the MM.

The presented approach for measurements of ϕ_{MM} can be implemented if the multiple reflection at the surfaces of a thin film is negligible, which is the case of MMs possessing strong absorption. If a material with weak absorption is under investigation additional interference terms due to the multiple reflection in a film have to be accounted for [134].

4.1.2   Interferometric setup

The developed interferometric setup was based on the Jamin-Lebedeff scheme [135]. The original interferometer was modified to provide simultaneous measurements in transmission and reflection [136]. The interferometric measurements were performed with a supercontinuum light source SuperK Versa from NTK Photonics (operating spectral range is from $\lambda = 0.4\,\mu\text{m}$ to $\lambda = 1.7\,\mu\text{m}$). The broad band generation of this source is based on the supercontinuum generation in an optical fiber [137].

The principal scheme of the interferometer is presented in Fig. 4.3. The linear polarizer P1 (operating spectral range is from $\lambda = 0.65\,\mu\text{m}$ to $\lambda = 2\,\mu\text{m}$) served
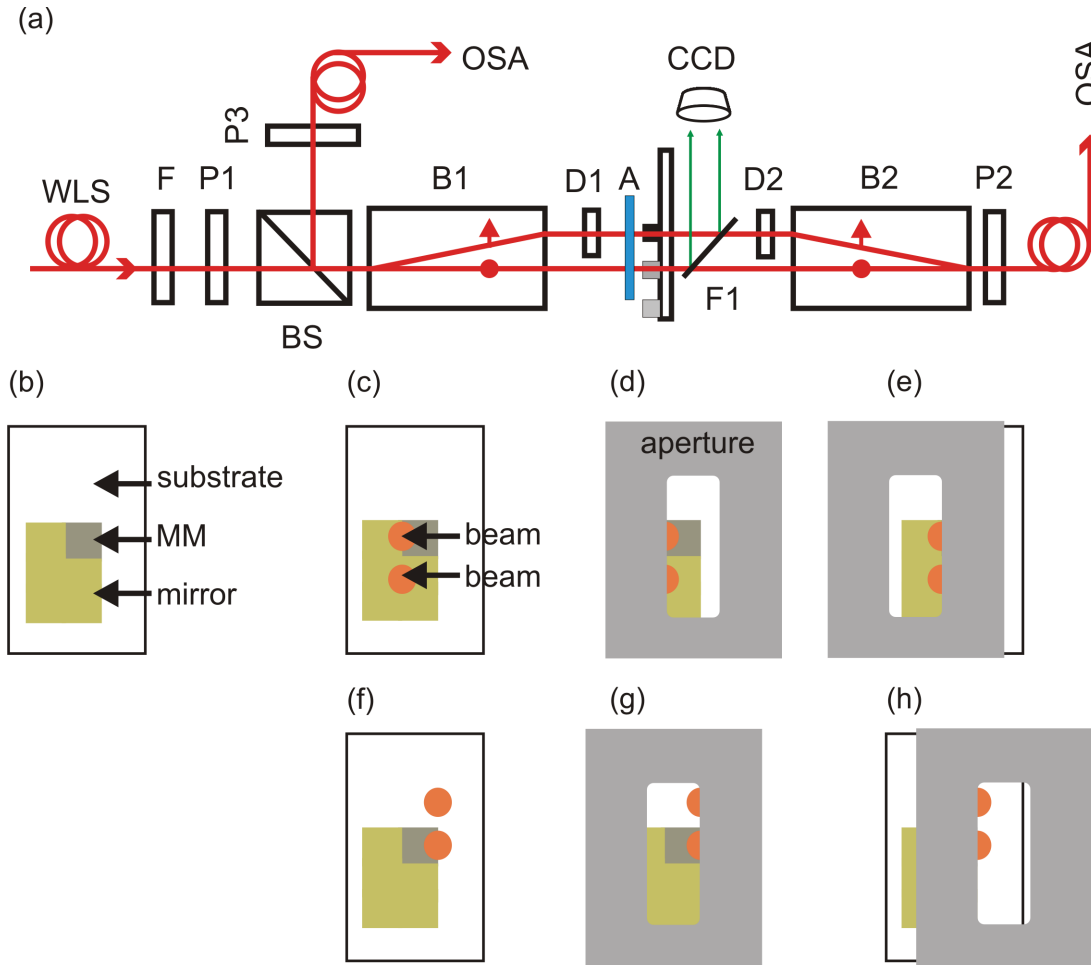
Figure 4.3: (a) - Interferometric setup. F - Low pass filter. P1, P2, P3 - Polarizers. B1, B2 - Beam displacers. D1, D2 - Delay elements. F1 - Filter. A - Aperture. (b) - Sample layout. (c) and (f) - The arrangement of the beams for measurements in reflection and transmission, respectively. (d) and (g) - Position of the aperture during sample measurements in reflection and transmission, respectively. (e) and (h) - Position of the aperture during reference measurements in reflection and transmission, respectively.

to control the polarization state of the input light. In the first birefringent beam displacer B1 (operating spectral range from $\lambda = 0.35\,\mu m$ to $\lambda = 2.3\,\mu m$) linear polarized light was split into two orthogonally polarized beams forming the two arms of the interferometer. The intensity distribution between the sample and reference arms was controlled by the rotation of the linear polarizer P1. The second beam displacer B2, which served to recombine the two beams, was followed by the linear polarizer P2, providing interference of the sample and reference beams. The recombined beam was coupled into a photonic crystal fiber (single mode for $\lambda > 0.6\,\mu m$). The analysis of the interference signal was performed with an optical spectral analyzer (OSA) Yokogawa AQ6370B, which was a grating spectrometer. The OSA provided a spectral resolution up to 20 pm in the spectral range from $\lambda = 0.6\,\mu m$ to $\lambda = 1.7\,\mu m$. The optical spectrum analyzer used the first diffraction

order in the spectral range from $\lambda = 0.6\,\mu m$ to $\lambda = 0.8\,\mu m$ and the second diffraction order in the range from $\lambda = 0.8\,\mu m$ to $\lambda = 1.7\,\mu m$. To avoid spatial overlapping of the higher diffraction orders of smaller wavelengths with the second diffraction order of larger wavelengths, an optical low pass filter F was used during the measurements in the VIS spectral range.

Measurements of the phase in reflection were realized with the beam splitter BS (operating spectral range is from $\lambda = 0.42\,\mu m$ to $\lambda = 1.7\,\mu m$). The sample and reference beams reflected from the sample were recombined in the first calcite beam displacer B1 and were guided to the part of the setup for the reflection measurements with a polarizing beam splitter BS.

The mirror symmetrical arrangement of the beam displaceres caused an optical path difference of about 4 mm between the interferometer arms. The very small period of the interference pattern (0.25 nm around $\lambda = 1\,\mu m$) corresponded to this path difference. Therefore, the optical length difference between the arms was decreased to a value of 1 mm to enable a high sampling rate of the interference signal. This was realized by placing compensating plates D1 and D2 made of BK7, each 2.3 mm thick, in the sample arm of the interferometer. The period of the corresponding interference pattern was about 2 nm at $\lambda = 1\,\mu m$.

4.1.3 The measurement procedure

Above, it was shown that two types of measurements (sample and reference) are required to define the phases of $t(\lambda)$ and $r(\lambda)$. As experimental MM films have typical thicknesses of about 100 nm, any misalignment of the sample on the nanometer scale between the sample and reference measurements would cause a critical error in the resulting absolute phase [136, 138]. Therefore, the sample and reference measurements were performed as follows. Instead of moving the sample between the measurements a movable aperture A placed in front of the sample was used (see Fig. 4.3(a)) [139]. The position of the aperture was controlled with a camera collecting the light reflected from the filter F1 placed after the sample. A sample containing reference fields (see Fig. 4.3(b)) was adjusted as it is shown in Figs. 4.3(c) and (f) for the measurements in reflection and transmission, respectively. During the sample measurements the aperture was arranged to screen one half of either of the two beams. The corresponding positions of the aperture for the reflection and transmission measurements are shown in Figs. 4.3(d) and (g). During the reference measurements the aperture blocked the other half of the beams as it is shown for reflection and transmission in Figs. 4.3(e) and (h), respectively.

Additionally, a normalization of a parasitic phase delay between the sample and

reference measurements occurring due to the diffraction of the beams on the aperture had to be performed. For this purpose, two measurements without any sample were performed while the aperture was blocking the left and the right halves of the beams, respectively. Without a sample the two measured phases ($\phi_1(\lambda)$ and $\phi_2(\lambda)$) had to be equal. However, due to the diffraction of the beams on the aperture the measured phases were different $\phi_1(\lambda) \neq \phi_2(\lambda)$. Subtraction of the phases obtained from the two measurements gave the normalization value $\phi_n(\lambda) = \phi_1(\lambda) - \phi_2(\lambda)$ which was later subtracted from the phases measured on the samples (ϕ_{MM}).

4.1.4 Numerical treatment of the signal

In Sec. 4.1.1 it was described how the phase of the interference signal can be retrieved using the Fourier transformation of the registered interference signal and the subsequent filtering of the correlation term in the time domain. As the measurements of signals were done in the wavelength domain, the measured signal had to be transformed to the frequency domain ($\omega = 2\pi c/\lambda$) and regularly sampled. The influence of the data interpolation, required to transform the spectra, on the accuracy of the phase definition was investigated in Ref. [140]. It was shown that, if the sampling rate of a signal is close to the Nyquist limit, linear interpolation of the signal causes a noisy background in the retrieved phase. In the experiment, in the VIS spectral range the period of the interference pattern was about 0.5 nm at $\lambda = 0.7\,\mu\text{m}$. To provide an appropriate signal to noise ratio, the signal acquisition was done with a resolution of 0.1 nm. To increase the sampling rate a so-called zero-fitting procedure [140] was applied to the signal. This technique is based on the Fourier transformation of the spectra from the wavelength space to an inverse space γ. Then the window size N is increased by adding additional points with zero amplitudes. In the experiments the window size was increased by a factor $4N$. The backward Fourier transformation gives the initial spectrum with an increased sampling rate. In Fig. 4.4(a) several periods of a test interference pattern are shown. The spectral phase retrieved for this data set is presented in Fig. 4.4(b) with a green line, while the original spectral phase is shown with a blue line. For a better visualization the curves were vertically shifted by Δ. It is seen that increasing the data set with the zero shift method allows for decreasing the noise in the spectral phase, which is shown in Fig. 4.4(b) with a red curve. Thereafter, the spectrum was linearly interpolated and the Fourier transformation could be performed.
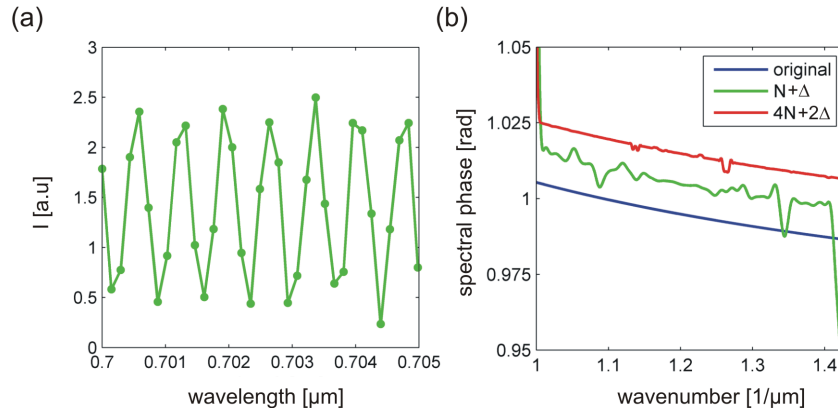
Figure 4.4: (a) - Several periods of a test signal with a low sampling rate. (b) - The spectral phases. The original, retrieved for a low sampling rate (N), and for the sampling rate $4 * N$ are shown with the blue, green, and red curves, respectively.

4.1.5 Transmittance and reflectance measurements

Transmittance and reflectance measurements were performed with a commercially available Perkin Elmer Lambda 950 spectrometer (double beam, double monochromator spectrophotometer with accessible spectral range from $\lambda = 0.17\,\mu\text{m}$ to $\lambda = 3\,\mu\text{m}$). As a light source a halogen lamp for the VIS/NIR and a deuterium lamp for the UV spectral range were used. The registration of the signal was realized with a photomultiplier and an InGaAs detector in the UV/VIS and NIR spectral ranges, respectively. The polarization state of the light was controlled with a Glan Thompson Polarizer. The measurements in transmission were performed in the sample chamber of the spectrometer under 0° angle of incidence using a home made sample holder.

The standard accessory for the reflection measurements was a 150 mm integration sphere, where the measurements under an angle of incidence of 8°could be performed. The measurements under normal incidence were realized with a specially designed setup, which could be integrated in the spectrometer. A home made aperture with a diameter of 1.5 mm was used for the measurements on MMs, having a typical area of 2 x 2 mm. To provide an appropriate signal to noise ratio, the measurements on MM samples were performed in the VIS spectral range with a spectral resolution of 2 nm and in the NIR with a spectral resolution of 5 nm.
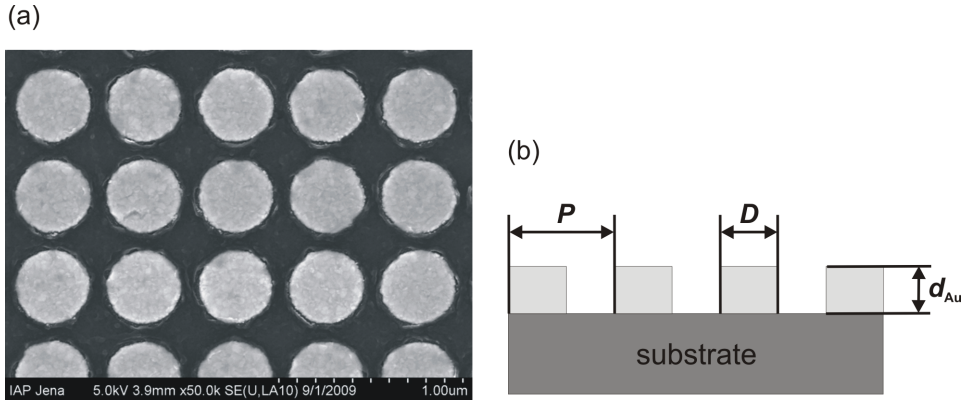
(a)

(b)

Figure 4.5: (a) - Top view image of an array of nanodisks. (b) - The side view of the nanodisks geometry with the period $P = 500\,\mathrm{nm}$, the diameter $D = 350\,\mathrm{nm}$, and the height $d_{\mathrm{Au}} = 30\,\mathrm{nm}$.

4.2 Verification of the methods for the characterization of NIMs

4.2.1 Gold nanodisk structure

The verification of the experimental and combined methods was done firstly with a simple plasmonic structure representing a layer of periodically arranged gold nanodisks. An SEM top view image of the structure is shown in Fig. 4.5(a). The period P of the nanodisks was 500 nm, the diameter D and height d_{Au} of the disks were 350 nm and 30 nm, respectively (see Fig. 4.5(b)). Based on the SEM images, a model accounting for the true size of the disks was constructed to be used in the numerical simulations. The optimization of the model was performed by fine tuning of the geometry to provide the best agreement of the measured and simulated spectra. However, it should be noted that in FMM simulations only periodic structures consisting of identical elements can be treated. Thus, effects such as an inhomogeneous broadening of the plasmon resonances occurring due to a slightly different form of the disks can not be reproduced in the simulations. A similar spectral response, however, can be achieved by varying the geometry of an ideally shaped disk.

The simulated and measured transmittance and reflectance spectra are presented in Fig. 4.6(a). The simulated and measured data have the indices "FMM" and "Exp.", respectively. In Fig. 4.6(b) and (c) the simulated and measured phases of the transmission and reflection coefficients are presented. The investigated nanodisk structure shows a plasmon resonance at the wavelength $\lambda = 0.95\,\mu\mathrm{m}$ corresponding to a minimum in the transmittance and a maximum in the reflectance. The phase of the transmission coefficient undergoes a phase jump close to π at the wavelengths
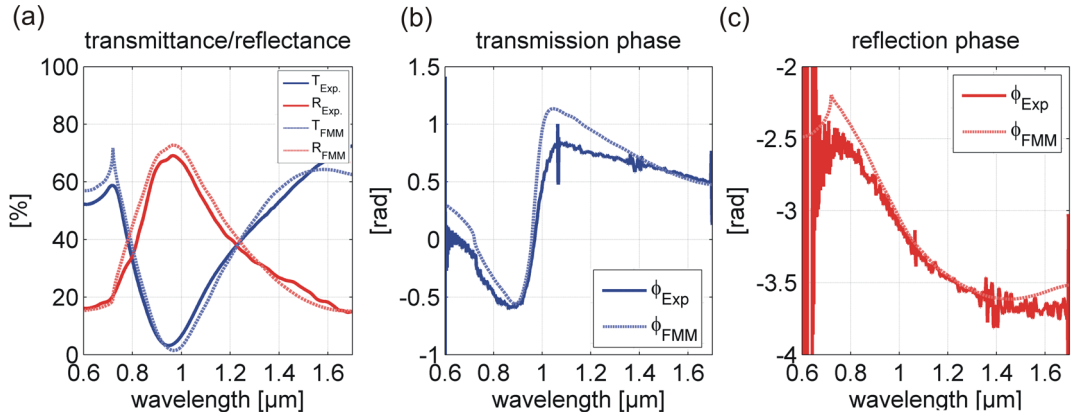
Figure 4.6: (a) - The measured and simulated transmittance and reflectance of the layer of nanodisks shown in Fig. 4.5. (b) - The phase of transmission and (c) - the phase of reflection coefficients. The measured and simulated data have the index "Exp." and "FMM", respectively.
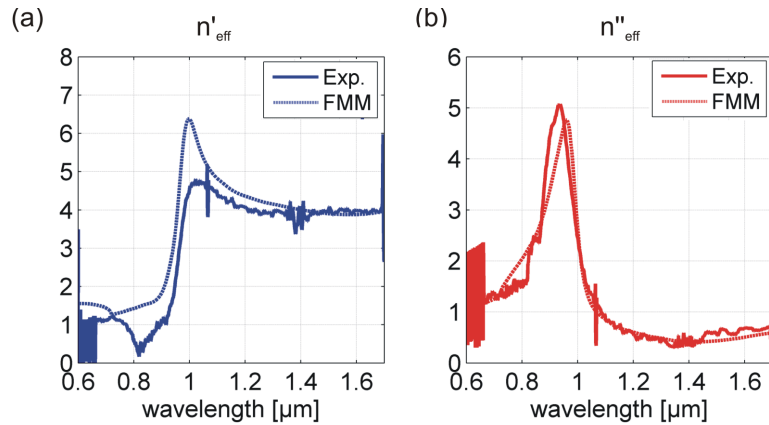

Figure 4.7: (a) - Real and (b) - imaginary parts of the effective refractive index of the nanodisk layer. The solid and dotted lines show results obtained using the experimental and combined methods, respectively.

around $\lambda = 0.95\,\mu$m, where the amplitude of the transmission coefficient has a minimum. An effective refractive index can be assigned to this layer and calculated according to Eq. (2.54). In Fig. 4.7 the effective refractive indices calculated using the simulated and experimental data are shown. The real and imaginary parts of the refractive indices are presented in Figs. 4.7(a) and (b), respectively. In Fig. 4.6(a) on can see that even for such a simple plasmonic MM a perfect agreement of the simulated and measured spectra could not be achieved. The comparison of the measured and simulated spectra shows that the position of the plasmon resonance is shifted in the simulations by about $\Delta\lambda = 20$ nm relative to the measured one. The difference in the width at half maximum of the resonance was estimated to be about 40 nm. One can see that these slight deviations in the resonance position and the resonance width between the measured and simulated spectra result in a difference
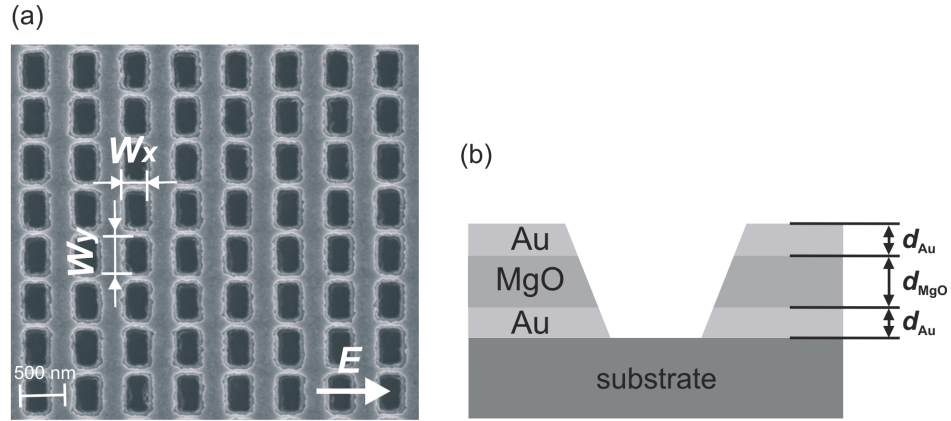
(a)

(b)

Figure 4.8: (a) - Top view image of the fishnet structure with $W_x = 180\,\text{nm}$ and $W_y = 380\,\text{nm}$; the vector $\boldsymbol{E}$ shows the resonant polarization. (b) - The side view of the unit cell geometry with a thickness of the Au layers $d_{\text{Au}} = 19\,\text{nm}$ and the MgO layer $d_{\text{MgO}} = 35\,\text{nm}$.

of the phases, which reach values up to $\Delta\phi = 0.5\,\text{rad}$ at a wavelength around $\lambda = 1\,\mu\text{m}$. As a result the effective refractive index obtained from experimental and simulated data deviates up to 30% in the real part at the wavelegth around the plasmon resonance.

4.2.2 Negative index metamaterial

A fishnet based NIM was designed to realize a negative effective refractive index at $\lambda = 1.4\,\mu\text{m}$. An SEM top view image of the fabricated structure and the side view of the unit cell are shown in Figs. 4.8(a) and (b). To obtain the best agreement between the simulated and measured structure, a fine tuning of the geometry of the structure in the simulations was undertaken. The obtained resulting parameters of the structure were as follows: $P_x = P_y = 500\,\text{nm}$, $W_x = 180\,\text{nm}$, $W_y = 380\,\text{nm}$, $d_{\text{Au}} = 19\,\text{nm}$, $d_{\text{MgO}} = 35\,\text{nm}$. In Fig. 4.9, the measured and simulated spectra and phases are presented for the polarization state of the incident light shown in Fig. 4.8(a). Under these illumination conditions, the symmetric and antisymmetric resonances at the wavelengths around $\lambda = 0.8\,\mu\text{m}$ and $\lambda = 1.4\,\mu\text{m}$ are excited. At the wavelengths of the antisymmetric resonance a dip in the phase of the transmission appears that evidences that the effective refractive index decreases. Indeed, at these wavelengths the real part of the effective refractive index becomes negative as it is seen in Fig. 4.10(a). At the wavelengths around $1.1\,\mu\text{m}$, where $n'(\omega)$ approaches unity the reflectance passes the zero point and the phase of the reflection undergos a phase jump close to π. Results of the comparison of the pure experimental and combined methods are presented in Fig. 4.11. In Figs. 4.11(a)
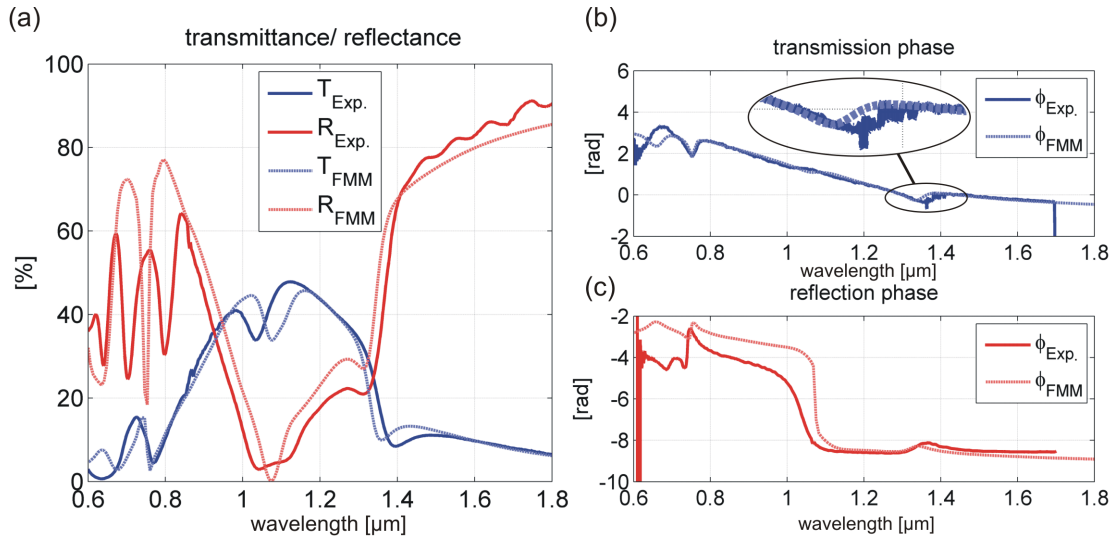
Figure 4.9: (a) - The measured and simulated transmittance and reflectance of the fishnet structure shown in Fig. 4.8. (b) - The phase of transmission and (c) - the phase of reflection coefficients. The measured and simulated data have index "Exp." and "FMM", respectively.

and (b) the difference between measured and simulated data is shown for transmittance $|\Delta T| = |T_{\text{Exp.}} - T_{\text{FMM}}|$ and reflectance $|\Delta R| = |R_{\text{Exp.}} - R_{\text{FMM}}|$. The differences in the transmission phase $|\Delta\phi_t| = |\phi_{t,\text{Exp.}} - \phi_{t,\text{FMM}}|$ and reflection phase $|\Delta\phi_r| = |\phi_{r,\text{Exp.}} - \phi_{r,\text{FMM}}|$ are shown in Fig. 4.11(c) and (d). The resulting errors in the real $|\Delta n'| = |n'_{\text{Exp.}} - n'_{\text{FMM}}|$ and imaginary $|\Delta n''| = |n''_{\text{Exp.}} - n''_{\text{FMM}}|$ parts of the effective refractive index are presented in Fig. 4.11(e) and (f). It is seen, that at $\lambda = 1.38\,\mu\text{m}$ the deviations in the real and imaginary parts of the effective refractive index reach values up to 0.6. However, as one can see in Fig. 4.10, the dramatic difference at $\lambda = 1.38\,\mu\text{m}$ is caused by a relative shift of the curves, while their shapes generally match.

4.2.3   Accuracy of the experimental and combined methods

A complex effective refractive index $n(\lambda) = n'(\lambda) + in''(\lambda)$ is an indirectly measured quantity depending on the modulus of the transmission coefficient $|t(\lambda)|$, the phase of the transmission coefficient $\arg t(\lambda)$, the modulus of the reflection coefficient $|r(\lambda)|$, and the phase of the reflection coefficient $\arg r(\lambda)$. Following the definition of the root mean square error of an indirectly measured quantity $f(x)$

$$\sigma = \sqrt{\sum_{i=1}^{n} \left(\frac{\partial f(x)}{\partial x_i} \sigma_{x_i} \right)^2}, \tag{4.11}$$
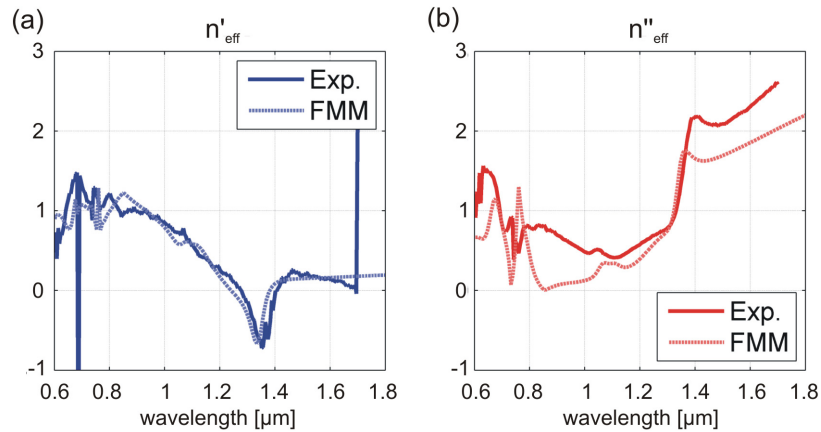
Figure 4.10: (a) - Real and (b) - imaginary parts of the effective refractive index of the fishnet MM. The solid and dotted lines show results obtained using the experimental and combined methods, respectively.
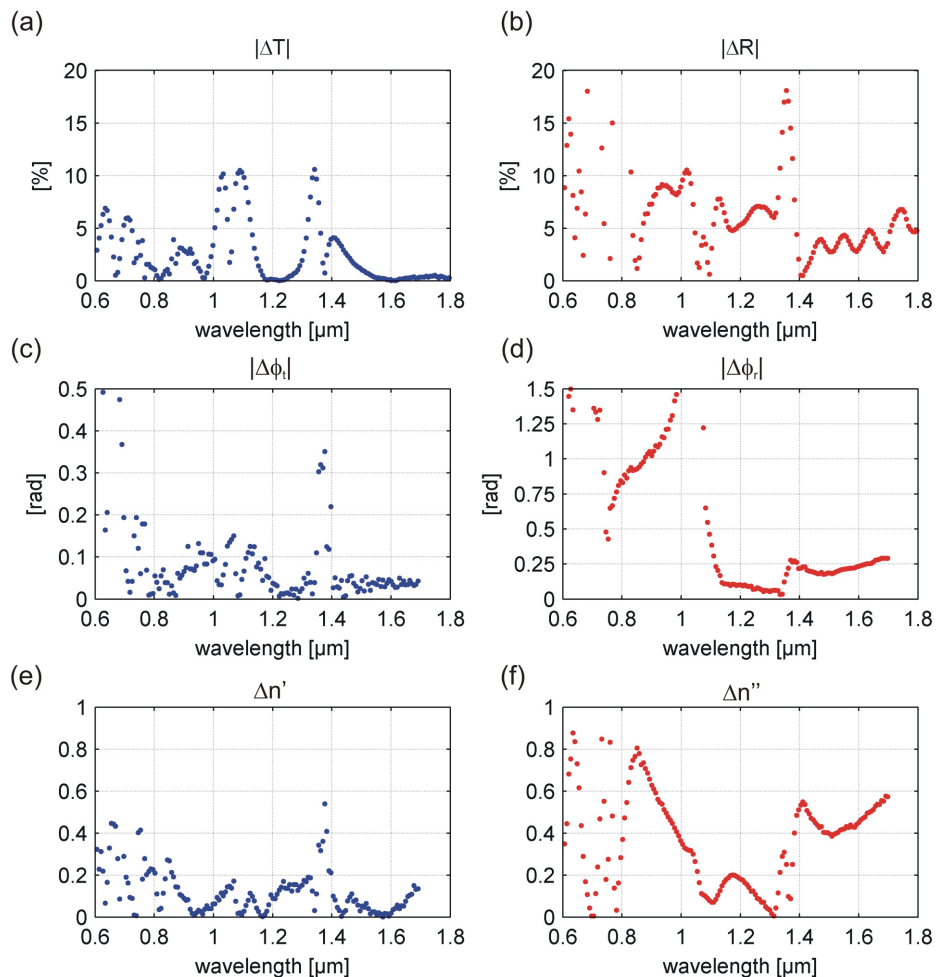

Figure 4.11: Difference between the measured and simulated (a) - transmittance, (b) - reflectance, (c) - transmission phase, (d) - reflection phase, (e) - real and (f) - imaginary parts of the effective refractive index.

the root mean square error can be calculated for the real and the imaginary parts of the effective refractive index obtained from measured data. The quantities $\sigma_{|t|}$, $\sigma_{\arg t}$, $\sigma_{\arg r}$, $\sigma_{|r|}$ are the root mean square errors of the measured parameters

$$\sigma_x = \frac{\sqrt{\sum\limits_{i=1}^{n} (\bar{x} - x_i)^2}}{n}, x \in \{|t|, \arg t, |r|, \arg r\}, \tag{4.12}$$

which all depend on the wavelength. In Tab. 4.1 the values of $\sigma_{|t|}$, $\sigma_{\arg t}$, $\sigma_{\arg r}$, $\sigma_{|r|}$ at $\lambda = 1.38\,\mu m$ obtained in the measurements of the fishnet NIM are given.

The partial derivatives of $n'_{\text{eff}}(\lambda)$ and $n''_{\text{eff}}(\lambda)$ with respect to $|t(\lambda)|$, $\arg t(\lambda)$, $|r(\lambda)|$, and $\arg r(\lambda)$ for the fishnet NIM are shown in Fig. 4.12. The real parts of the respective derivatives are depicted by blue lines, and the imaginary parts by red lines. The values of the partial derivatives for the fishnet structure at a wavelength of $1.38\,\mu m$ where n' has its minimum are given in Tab. 4.2. The values in Tab. 4.1 were obtained from the experimental data. Taking the accuracy of the transmittance and reflectance measurements from Tab. 4.1 and the experimental values for the derivatives we obtain $\sigma_{n'} = 0.04$ and $\sigma_{n''} = 0.07$ for the fishnet structures at $\lambda = 1.38\,\mu m$.

To estimate the accuracy of the combined method, let us consider the derivatives of n with respect to $|t|$, $|r|$, $\arg t$, and $\arg r$ presented in Fig. 4.12. Here one can see that in the region where the negative refractive index becomes negative (around $\lambda = 1.38\ \mu m$) the real part of the effective refractive index depends strongly on the phases of the transmission and reflection coefficients. The dependence on the absolute values of t and r, in turn, is weak. On the contrary, the imaginary part of the effective refractive index depends mainly on the absolute values of t and r and not on their phases. This means that if the simulated and measured transmittance and reflectance have a good agreement at $\lambda = 1.38\ \mu m$, no conclusions can be made about the accuracy of determination of n'_{eff} at this wavelength. This issue, namely the neccessity of phase measurements for the correct effective refractive index retrieval was discussed in Ref. [24]. Nevertheless, the combined method can be applied to define $n_{\text{eff}}(\lambda)$ if a good agreement between measured and simulated $T(\lambda)$

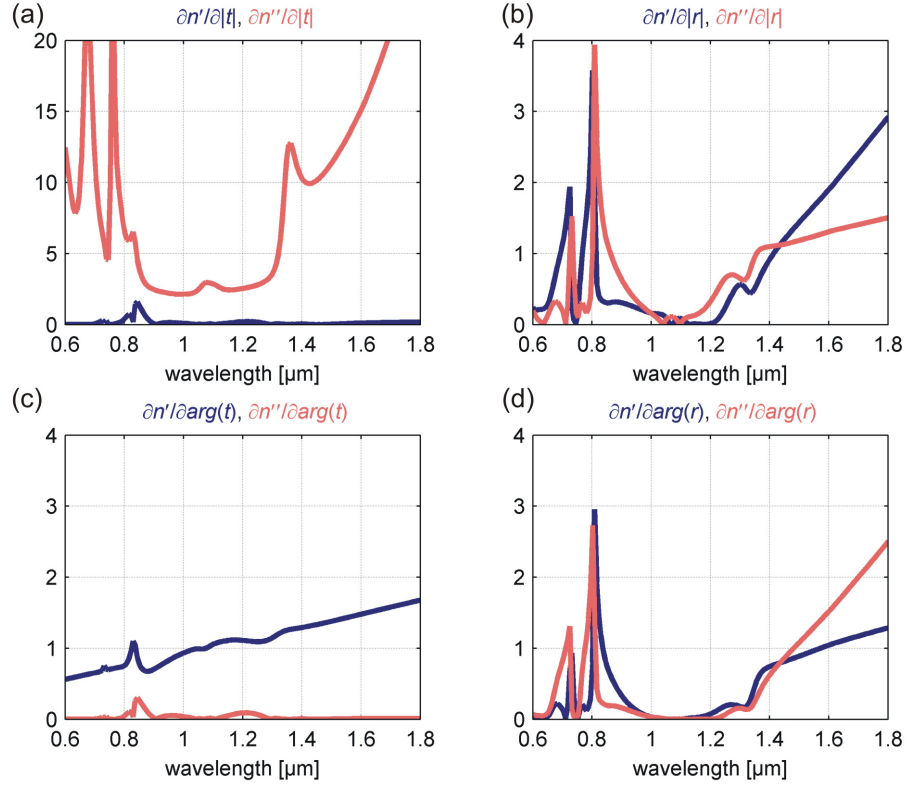| $\sigma_{|t|}$	$\sigma_{|r|}$	$\sigma_{\arg t}$	$\sigma_{\arg r}$
0.01	0.007	0.02	0.02

Table 4.1: Root mean square errors

Figure 4.12: Partial derivatives of the real and imaginary parts of the effective refractive index with respect to (a) - $|t|$, (b) - $|r|$, (c) - $\arg t$, and (d) - $\arg r$. The partial derivatives of the real and imaginary partes are represented by blue and red lines, respectively.

and $R(\lambda)$ is achieved in a broad spectral range. Indeed, it is known that the phase shift in transmission or reflection of a thin film is related to the transmittance and reflectance in the whole spectral range [141]. For a complex transmission coefficient $t(\lambda) = |t(\lambda)| \exp\left[i\phi_{\mathrm{t}}(\lambda)\right]$ one can write

$$\ln t(\lambda) = \ln |t(\lambda)| + i\phi_{\mathrm{t}}(\lambda). \tag{4.13}$$

According to Ref. [141] the Kramers-Kronig relation for the real and imaginary parts of the function $\ln t(\lambda)$ gives

$$\phi_{\mathrm{t}}(\omega) = \frac{-2\omega}{\pi} P \int_0^\infty \frac{\ln |t(\omega')|}{\omega'^2 - \omega^2} d\omega', \tag{4.14}$$

$\lambda\,[\mu m]$	$\frac{\partial n'}{\partial |t|}$	$\frac{\partial n'}{\partial |r|}$	$\frac{\partial n'}{\partial \arg t}$	$\frac{\partial n'}{\partial \arg r}$	$\frac{\partial n''}{\partial |t|}$	$\frac{\partial n''}{\partial |r|}$	$\frac{\partial n''}{\partial \arg t}$	$\frac{\partial n''}{\partial \arg r}$
λ_{exp}=1.38 µm	0.14	0.17	2.52	0.69	4.88	2.18	0.06	0.05

Table 4.2: Partial derivatives for the fishnet structure

where P signifies the principle value of the integral and $\omega = 2\pi c/\lambda$. The same relation can be written for the reflection coefficient $r = |r| \exp[i\phi_r]$. The Kramers-Kronig transformation method based on the relation expressed with Eq. (4.14) is widely used for the determination of the material parameters of thin films [141–145]. Direct implementation of the Kramers-Kronig transformation method for MMs is prevented, because at high frequencies the MMs can not be considered as homogeneous media and the integration in Eq. (4.14) can not be conducted for $\omega \to \infty$. The development of an appropriate model which would extend $n_{\mathrm{eff}}(\omega)$ for higher frequencies would eliminate this limitation.

However, the general statement that the phase shift in transmission or reflection at a certain wavelength is connected with the amplitude of the respective coefficient (transmission or reflection) holds for MMs. Thus, only the good agreement of simulated and measured transmittances and reflectances in a broad spectral range allows for using simulated phases of t and r to determine $n_{\mathrm{eff}}(\lambda)$.

In Sec. 4.2.2 it was demonstrated that it is difficult to introduce an adequate quantitative criterion for the accuracy of the combined method relying on spectral differences of measured and simulated transmittances and reflectances. Consequently, the combined method can be used only for a preliminary estimation of the effective refractive index of a MM, and resorting to the experimental method is required to determine $n_{\mathrm{eff}}(\lambda)$ precisely.

Chapter summary

In this chapter an experimental method for the characterization of the effective refractive index of MMs was presented [136]. The phases of the complex transmission and reflection coefficients required for the calculations of $n_{\mathrm{eff}}(\lambda)$ were measured using the developed interferometric technique based on the white-light spectral interferometry. The interferometric setup was a modified Jamin-Lebedeff interferometer for measurements in transmission and reflection. Using this method phase measurements in the spectral range from $\lambda = 0.65\,\mu\mathrm{m}$ to $\lambda = 1.7\,\mu\mathrm{m}$ with an accuracy of the phase definition of ± 0.02 rad in transmission and reflection were enabled. The measurements of the transmittance and reflectance were performed with a commercially available Lambda 950 spectrometer.

Verification of the experimental and combined methods was conducted with a MM consisting of gold nanodisks and a fishnet NIM. It was demonstrated that the combined method can be used to determine $n_{\mathrm{eff}}(\lambda)$ only if a good agreement between the measured and simulated spectra in a broad spectral range is achieved. However, even in the case of MMs with a simple geometry of the unit cell, a perfect agreement between the measured and simulated spectra is hard to achieve. Thus,

the combined method is suitable only for the preliminary estimation of the effective refractive index and the implementation of the experimental method is required to determine $n_{\text{eff}}(\lambda)$ precisely.

The developed method allows for the characterization of effective parameters of MMs in the spectral range from $\lambda = 0.65\,\mu\text{m}$ to $\lambda = 1.7\,\mu\text{m}$ under normal incidence. Using this method a negative effective refractive index $n_{\text{eff}} = -0.97 \pm 0.04 + i(1.76 \pm 0.07)$ at $\lambda = 1.38\,\mu\text{m}$ was experimentally demonstrated for a fishnet NIM.

Chapter 5

Magnetic properties of asymmetric double-wire structures

In the previous chapters it was shown that the excitation of the antisymmetric mode in a plasmonic double cut-wire structure gives rise to the charge dynamics in the system, associated with a non-zero magnetic moment. Additionally, it has been demonstrated how the magnetic response of double cut-wires can be designed by tuning the geometry of symmetric metaatoms. It is evident, however, that the symmetry of the structure itself can be a powerful tool for the design of magnetic properties of MMs. In this chapter the influence of asymmetry on the magnetic response of double cut-wires is considered. The investigations of the magnetic response of asymmetric double cut-wires were conducted experimentally and theoretically using numerical simulations and the analytical multipole model from Ref. [59]. The system under investigation was the double cut-wire elongated infinitely in one of the directions. Such a two dimensional geometry is further referred to as a double-wire system. The asymmetry was introduced into the system by varying the length of the cut-wires in the direction where the plasmonic resonances are excited. To provide the analytical description of the systems, an extension of the theoretical multipole model [59] to the case of asymmetric double-wire structures has been undertaken. The extended model is presented in Sec. 5.1. For the further development of the analytical approach, the description of the coupling between double-wires based on a model of two interacting point dipoles was considered (Sec. 5.1.2). The extended analytical model was used to investigate the magnetization of systems of double-wires with different degrees of asymmetry. The charge and current dynamics as well as the magnetic properties of the system are discussed in Sec. 5.3. The chapter is closed with Sec. 5.4, where results of experimental investigations on the magnetic properties of asymmetric double-wires are presented.
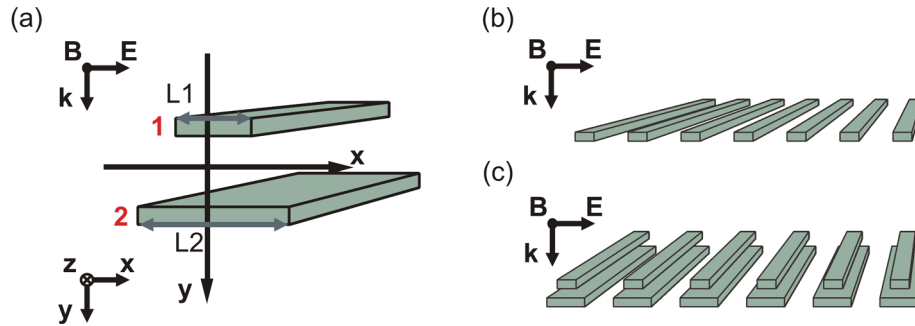
Figure 5.1: (a) - Arrangement of the structure used in the analytical model. (b) - Single-wire structure. (c) - Double-wire structure.

5.1 Multipole model for asymmetric structures

In this study, the general case of double cut-wires, which are infinitely extended in the z direction (Fig. 5.1.) was considered. The two dimensional configuration was chosen to relax the requirements on the computational resources for the numerical simulations of the system. The obtained results, however, can be easily transferred to the case of wires of finite length.

To control the asymmetry of the structure, the length $L_{1,2}$ of the wires in x direction (see Fig. 5.1(a)) was used. This type of asymmetry can be easily realized using the step-by-step lithographic technology presented in Sec. 3.3. To characterize the asymmetry of the structures quantitatively, the parameter $\Delta L = L_1 - L_2$ was introduced. The length of the first wire ranged from $L_1^{\min} = 200\,\text{nm}$ to $L_1^{\max} = 300\,\text{nm}$, while the length of the second one ranged from $L_2^{max} = 300\,\text{nm}$ to $L_2^{\min} = 200\,\text{nm}$ providing the conservation of the amount of metal in the structure ($L_1 + L_2 = \text{constant}$). For the simulations, the wires were placed in air with a separation distance of 40 nm between them. This was a simplification compared to the common experimental arrangement, where structures are placed on a substrate and are separated with a dielectric. The presence of a substrate breaks the symmetry of the structure even for wires of the same length [146, 147]. Therefore, to concentrate on the effects caused by the asymmetry of the wires only, the systems were considered in a symmetric environment. Nevertheless, the simplified model qualitatively describes the effects observed in the experimental system as will be shown in Sec. 5.4.

As it was shown in Ref. [59] and discussed in Sec. 2.3.2, the system of double-wires can be described by a set of two coupled oscillators, each of which is associated with the fundamental dipole mode of a wire

$$\begin{aligned}
\ddot{x}_1(t) + \gamma_1 \dot{x}_1(t) + \omega_{01}^2 x_1(t) - \sigma x_2(t) &= \frac{q_1}{m} E_{1x}(y - y_1, t), \\
\ddot{x}_2(t) + \gamma_2 \dot{x}_2(t) + \omega_{02}^2 x_2(t) - \sigma x_1(t) &= \frac{q_2}{m} E_{2x}(y + y_1, t),
\end{aligned} \tag{5.1}$$

where the amplitudes x_1 and x_2 correspond to the elongations of the negatively charged carrier densities driven by the electric field; ω_{01}, ω_{02} are the eigenfrequencies of the oscillators; γ_1, γ_2 are the damping constants; q_1, q_2 are the effective charges; m is the mass of the effective carrier; σ is the coupling constant; $-y_1$ and y_1 are the positions of the carriers along the y coordinate.

The solution of the system (5.1) can be easily found in the Fourier domain under the assumption that $x_{1,2}(t) = \tilde{x}_{1,2}(\omega)\exp(-i\omega t)$

$$\tilde{x}_1(\omega) = \frac{a_1\left(\omega_{02}^2 - \omega^2 - i\gamma_2\omega\right)\tilde{E}_{1x}(y - y_1,\omega) + \sigma a_2\tilde{E}_{2x}(y + y_1,\omega)}{\left(\omega_{01}^2 - \omega^2 - i\gamma_1\omega\right)\left(\omega_{02}^2 - \omega^2 - i\gamma_2\omega\right) - \sigma^2},\qquad(5.2)$$

$$\tilde{x}_2(\omega) = \frac{a_2\left(\omega_{01}^2 - \omega^2 - i\gamma_1\omega\right)\tilde{E}_{2x}(y + y_1,\omega) + \sigma a_1\tilde{E}_{1x}(y - y_1,\omega)}{\left(\omega_{01}^2 - \omega^2 - i\gamma_1\omega\right)\left(\omega_{02}^2 - \omega^2 - i\gamma_2\omega\right) - \sigma^2},\qquad(5.3)$$

$$a_1 = \frac{q_1}{m},\ a_2 = \frac{q_2}{m}.\qquad(5.4)$$

The interaction of a EM wave with the material is described with the electric polarizability $\tilde{P}(y,\omega)$, the quadrupole tensor $\tilde{Q}(y,\omega)$, and the magnetization $\tilde{M}(y,\omega)$, whose non-zero elements can be written as

$$\tilde{P}_x(y,\omega) = -2\eta\left[q_1\tilde{x}_1(\omega) + q_2\tilde{x}_2(\omega)\right],\qquad(5.5)$$

$$\tilde{Q}_{xy}(y,\omega) = y_1\eta\left[q_2\tilde{x}_2(\omega) - q_1\tilde{x}_1(\omega)\right],\qquad(5.6)$$

$$\tilde{M}_z(y,\omega) = i\omega y_1\eta\left[q_2\tilde{x}_2(\omega) - q_1\tilde{x}_1(\omega)\right],\qquad(5.7)$$

where η is the density of the metaatoms (double-wires). The electromagnetic moments were introduced in Sec. 2.3.1, see Eqs. (2.47) and (2.48). Having calculated the dipole, quadrupole and magnetic dipole contributions, the wave equation

$$\frac{\partial^2\tilde{E}_x(y,\omega)}{\partial y^2} = \omega^2\mu_0\left[\epsilon_0\tilde{E}_x(y,\omega) + \tilde{P}_x(y,\omega) - \frac{\partial\tilde{Q}_{xy}(y,\omega)}{\partial y}\right] + i\omega\mu_0\frac{\partial\tilde{M}_z(y,\omega)}{\partial y}\quad(5.8)$$

can be solved, and the dispersion relation $k(\omega)$ is

$$k_y^2(\omega) = 2\frac{\omega^2}{c^2}\frac{R_1R_2 - \sigma^2 + A\left(a_1R_2 + a_2R_1 - 2\sigma\sqrt{a_1a_2}\right)}{2\left(R_1R_2 - \sigma^2\right) - \frac{\omega^2}{c^2}Ay_1^2\left(a_1R_2 + a_2R_1 - 3\sigma\sqrt{a_1a_2}\right)},\qquad(5.9)$$

where

$$R_1 = \left(\omega_{01}^2 - \omega^2 - i\gamma_1\omega\right),\ R_2 = \left(\omega_{02}^2 - \omega^2 - i\gamma_2\omega\right).\qquad(5.10)$$

In order to connect the model with the simulated system, the characteristic parameters of the oscillators (ω_{01}, ω_{02}, γ_1, γ_2, a_1, a_2) have to be found. For this purpose,

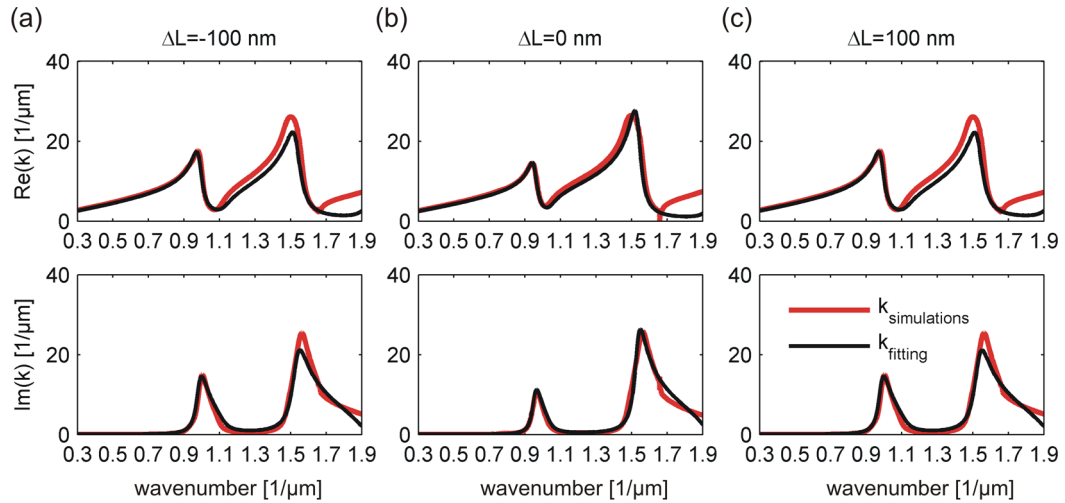(a) $\Delta L = -100$ nm (b) $\Delta L = 0$ nm (c) $\Delta L = 100$ nm

Figure 5.2: In the columns (a), (b), (c) - are the data for the structures with $\Delta L = 100$ nm, $\Delta L = 0$ nm, and $\Delta L = -100$ nm, respectively. Red curves represent wave vectors obtained from the rigorous numerical simulations. Black lines represent wave vectors obtained from the fitting procedure.

the complex transmission and reflection coefficients of corresponding layers of MMs were calculated using FMM. The dispersion relations were found with the modified retrieval algorithm from Ref. [148], which was developed to treat MMs with strongly inhomogeneous unit cells. Then the parameters of the oscillators were found from the fitting of the numerically and analytically calculated dispersion relations.

In this section, the angular frequency representation ω was used in all formulas to derive the dispersion relation of a MM based on asymmetric double-wires. In the following diagrams the wavenumber representation ($\widetilde{\nu} = 2\pi c/\omega$) of the spectral data is used to facilitate the conversion of the data to the wavelength domain.

5.1.1 Parameters of harmonic oscillators

For the analytical description of the double-wire structure the parameters of the oscillators (ω_{0i}, γ_i, a_i) and the coupling constant (σ) corresponding to the systems under consideration have to be defined. This problem is reduced to finding the connection between ω_{0i}, γ_i, a_i and the length L of a wire. This dependence is the same for the two wires. Additionally, σ has to be found for each asymmetric system (for each value of ΔL). The parameters of the oscillators can be found from the simulations of single-wire (Fig. 5.1(b)) and double-wire (Fig. 5.1(c)) structures. To demonstrate the accuracy of the fitting procedure, the wave vectors obtained from the fitting procedure (black curves) and from rigorous numerical calculations (red curves) for double-wire structures are shown in Fig. 5.2. The wave vectors from the numerical simulations were calculated with the retrieval algorithm from Ref. [148],
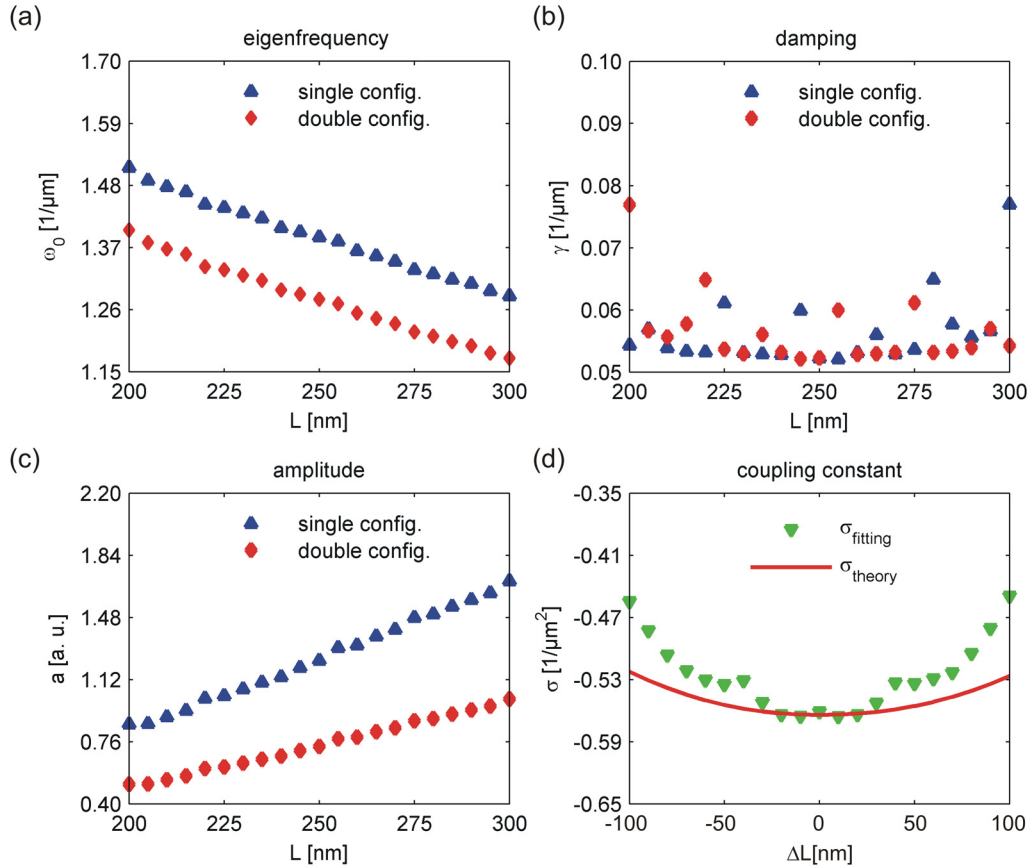
Figure 5.3: (a), (b), and (c) - Parameters of the oscillators as functions of the length L of the corresponding wire (L reads as L_1 for the first oscillator and as L_2 for the second one). Blue triangle marks and red diamond marks correspond to the parameters obtained from the single-wire configurations and double-wire configurations, respectively. In (d) - the red line represents coupling constant obtained from the theoretical expression Eq. (5.18), the green triangles show the results of the fitting to the rigorous numerical results.

using complex transmission and reflection coefficients from the FMM simulations.

The parameters providing the best fit of the analytically calculated dispersions to the numerically calculated ones for the single-wire structures are shown in Fig. 5.3(a)-(c) with blue triangle marks. The eigenfrequency of the oscillator (Fig. 5.3(a)) is inversely proportional to the length of the wire, the amplitude (Fig. 5.3(c)) is proportional to the length, while the damping constant (Fig. 5.3(b)) in a first approximation does not depend on the length of the wire.

The same set of parameters extended by σ was calculated for the double-wire configuration in a similar manner from the fitting of the theoretical dispersion relations to the numerical ones. The parameters obtained from the double-wire system (shown in Fig. 5.3, red diamond marks) have the same dependence on the length of the wire, however the eigenfrequencies and amplitudes are shifted relative to the
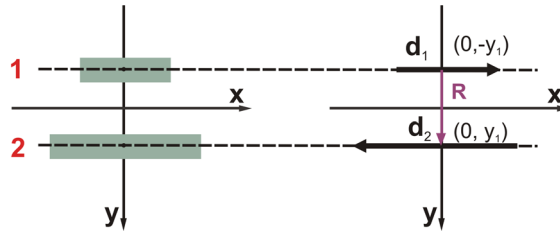
Figure 5.4: Arrangement of the point dipoles associated with the double-wire system.

values obtained for the single-wire configuration. This deviation appears due to the interaction of the wires with the neighbors in the lateral direction, which is different for the single- and double-wire configurations. This interaction is not included in the theoretical model, however unavoidably appears in the FMM simulations and in the experiment, where the wires have a periodical arrangement with a small period. Hence, the results obtained from the simulations of single-wire structures can be used only for a qualitative estimation of the parameters. Nevertheless, the effect of the interaction can be taken into account by assuming that the oscillators have a larger effective mass in the double-wire arrangement in comparison with the single-wire configuration.

5.1.2 Analytical model for the coupling constant

The coupling between the double-wires can be qualitatively described using the hybridization model (see Sec. 2.2.2). For the quantitative description of the interaction, an analytical expression for the coupling constant σ as a function of the parameter of asymmetry ΔL has to be known. Resorting to such an analytical model would allow for a significant reduction of the number of numerical calculations required to match the oscillator model with the real structure. A simple approximation of the wire system providing the analytical description of the interaction is a system of two point dipoles. The two dipoles are placed in the points with coordinates $(0, y_1)$ and $(0, -y_1)$, shown in Fig. 5.4, and have dipole moments $\boldsymbol{d}_1 = q_1 x_1$ and $\boldsymbol{d}_2 = q_2 x_2$. According to the results of the numerical simulations presented in Fig. 5.3(c), the charge of each dipole can be assumed to be proportional to the length of the corresponding wire $q = \alpha L$.

The coupling constant σ can be expressed as a function of the dipole moments $\boldsymbol{d}_1$ and $\boldsymbol{d}_2$, by taking into account that the interaction term in each equation of motion in the system presented in Eq. (5.1) is the force acting on one oscillator from the other one. Based on the assumption of dipole character of the interaction between the wires, this force can be derived from the potential energy U of two dipoles [149].

For the first oscillator the force is

$$\boldsymbol{F_1} = -\frac{\partial U}{\partial \boldsymbol{r}_1} = -\frac{\partial U}{\partial x_1} \tag{5.11}$$

and for the second one it reads

$$\boldsymbol{F_2} = -\frac{\partial U}{\partial \boldsymbol{r}_2} = -\frac{\partial U}{\partial x_2}. \tag{5.12}$$

The potential energy of two point dipoles with dipole moments $\boldsymbol{d_1}$ and $\boldsymbol{d_2}$ at a distance $\boldsymbol{R}$ [65] is

$$U = \frac{\boldsymbol{d_1}\boldsymbol{d_2}R^2 - 3(\boldsymbol{d_1}\boldsymbol{R})(\boldsymbol{d_2}\boldsymbol{R})}{R^5}. \tag{5.13}$$

As the considered dipoles are arranged parallel to the x-axis the potential energy takes the form

$$U = \frac{-2(\boldsymbol{d_1}\boldsymbol{d_2})}{R^3} = \frac{-2q_1x_1q_2x_2}{R^3}. \tag{5.14}$$

Eqs. (5.11) and (5.12) can be written as

$$\boldsymbol{F_1} = -\frac{\partial U}{\partial x_1} = \frac{-2q_1q_2x_2}{R^3} = -\sigma x_2, \tag{5.15}$$

$$\boldsymbol{F_2} = -\frac{\partial U}{\partial x_2} = \frac{-2q_1q_2x_1}{R^3} = -\sigma x_1, \tag{5.16}$$

where the coupling constant σ is introduced as

$$\sigma = \frac{-2q_1q_2}{R^3}. \tag{5.17}$$

Now, using the assumption that the charge of each dipole is proportional to the length of the wire ($q = \alpha L$), we obtain an analytical expression for the coupling constant

$$\sigma = \frac{-\alpha^2}{R^3}\frac{(S^2 - \Delta L^2)}{2}, \tag{5.18}$$

$$S = L_1 + L_2. \tag{5.19}$$

The coupling constant depends on the parameter of asymmetry ΔL and on the total length of the wire system. The coefficient of proportionality α can be defined using σ obtained from the fitting procedure for the symmetric case ($\Delta L = 0$). Comparison of σ from Eq. (5.18) (Fig. 5.3(d), red line) with the coupling constant from the fitting procedure (Fig. 5.3(d), green triangles) shows that the model of two coupled dipoles
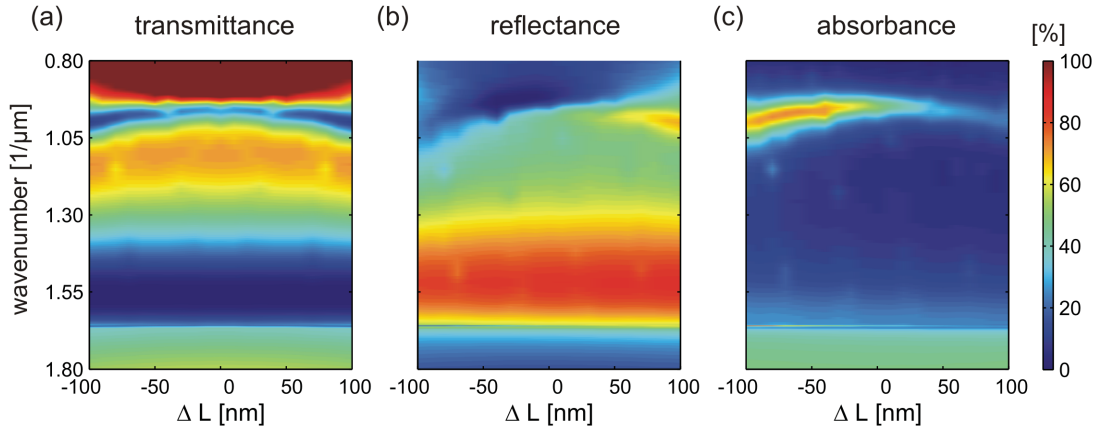
Figure 5.5: (a) - Transmittance, (b) - reflectance, and (c) - absorbance spectra in dependence on the structural asymmetry (ΔL) calculated using rigorous numerical simulations.

qualitatively describes the interaction between the wires. However, a more realistic model is required to provide an accurate description of the interaction between the wires.

5.2 Eigenmodes of asymmetric double-wire structures

A symmetric double-wire structure possesses two modes with frequencies separated due to the interaction between the wires [22, 71, 129]. One of the modes has a symmetric field profile and the other an antisymmetric one. In a system of two different wires the field profiles of the corresponding modes are no longer purely symmetric or antisymmetric. Nevertheless, for the sake of conciseness, the notation of "symmetric" and "antisymmetric" mode for asymmetric structures is used further in the text.

According to the coupled mode theory, the stronger the wires couple, the larger is the frequency splitting of the modes. Obviously, the coupling between wires is maximal if the wires have the same lengths and it becomes weaker if the length difference increases. The dependence of the frequency splitting on the length difference ΔL can be extracted from the spectra presented in Fig. 5.5(a)-(c), where the resonances corresponding to the excitation of the two modes can be easily identified. Both resonances appear in the spectra as minima of the transmittance - see Fig. 5.5(a). The antisymmetric mode is associated with a carrier distribution having a pronounced quadrupole moment. Therefore, excitation of the antisymmetric mode is accompanied by an increase of absorption, which is enhanced by its non-radiating character - see Fig. 5.5(c). The symmetric mode, in contrast, has the radiating

property of a dipole and appears as high reflectance in the spectra - see Fig. 5.5(b). Thus, we observe that the resonances in Fig. 5.5 indeed have the largest spectral separation in the symmetric case ($\Delta L = 0$ nm) and approach the eigenfrequencies of the uncoupled wires if the difference of their lengths increases.

5.3 Magnetic response of double-wire systems

5.3.1 Dynamics of currents

To understand the influence of the asymmetry on the orientation of the magnetic moment of the double-wires, the dynamics of the currents in the system have to be analyzed. Further the dynamics of the system will be considered in the two limiting cases $\Delta L = 100$ nm and $\Delta L = -100$ nm.

Data corresponding to the system with $\Delta L = 100$ nm are presented in Fig. 5.6(a)-(g), where the phase information for the amplitudes $x_{1,2}$ (Fig. 5.6(b)) and the currents $j_1 = q_1 \dot{x}_1$ and $j_2 = q_2 \dot{x}_2$ (Fig. 5.6(d)) are given with respect to the phase of the electric field in the center of the unit cell. It is seen, that at frequencies around the eigenfrequency of the antisymmetric mode (0.9 μm^{-1} - 1.1 μm^{-1}, see Fig. 5.6(a)), the first oscillator x_1 has a larger amplitude than the second one x_2. The reasons are the larger size and the top position of the first wire, which is affected by the incoming wave first. In this case, according to Eq. (5.1), the first oscillator, which is the largest one, dominates over the second one, whereas the influence of x_2 on the dynamics of x_1 is negligible. Indeed, out of the resonance, at frequencies lower than the eigenfrequency of the antisymmetric mode (1.05 μm^{-1}) the first oscillator follows the electric field almost in phase (Fig. 5.6(b)). The second oscillator is mostly driven by the first one and acquires a phase shift of about π with respect to x_1 at frequencies close to the eigenfrequency of the antisymmetric mode. In the resonance both oscillators undergo a phase jump close to π; as a result for frequencies higher than the resonance frequency, x_1 oscillates out of phase and x_2 oscillates in phase with the electric field. The currents j_1 and j_2 associated with these oscillations are presented in Figs. 5.6(c) and (d).

For the structure with $\Delta L = -100$ nm (see Fig. 5.6(h)-(n)) the situation should be inverse, as the larger oscillator is x_2, which is below the first one. However, the excitation conditions for x_2 are not optimal, due to the first oscillator, which screens the lower one from the exciting electric field. As a result, the amplitudes of oscillators x_1 and x_2 are of the same order and smaller than in the case $\Delta L = 100$ nm. Nevertheless, the phase of the larger oscillator x_2 is closer to the phase of the electric
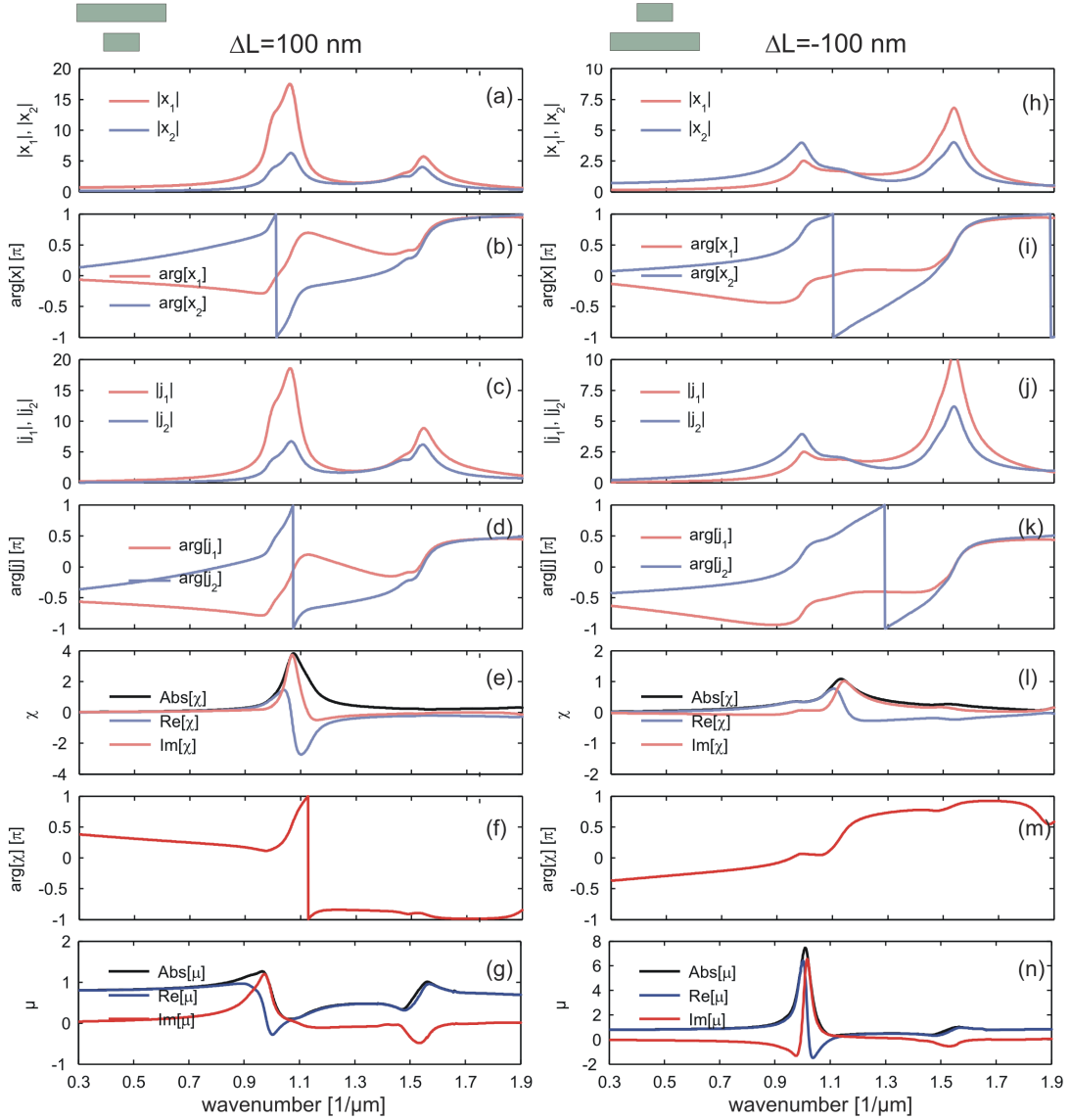
Figure 5.6: In the left column - plots (a)-(g) are the data for the structure with $\Delta L = 100\,\text{nm}$, in the right column - plots (h)-(n) are the data for the structure with $\Delta L = -100\,\text{nm}$. (a), (h) - Absolute values and (b), (i) - phases of the amplitudes of the oscillators. (c), (j) - Absolute values and (d), (k) - the phases of the currents. (e), (l) - Absolute values, the real, and the imaginary parts and (f), (m) - phases of the parameter χ. (g), (n) - Absolute values, real and imaginary parts of the effective magnetic permeability.
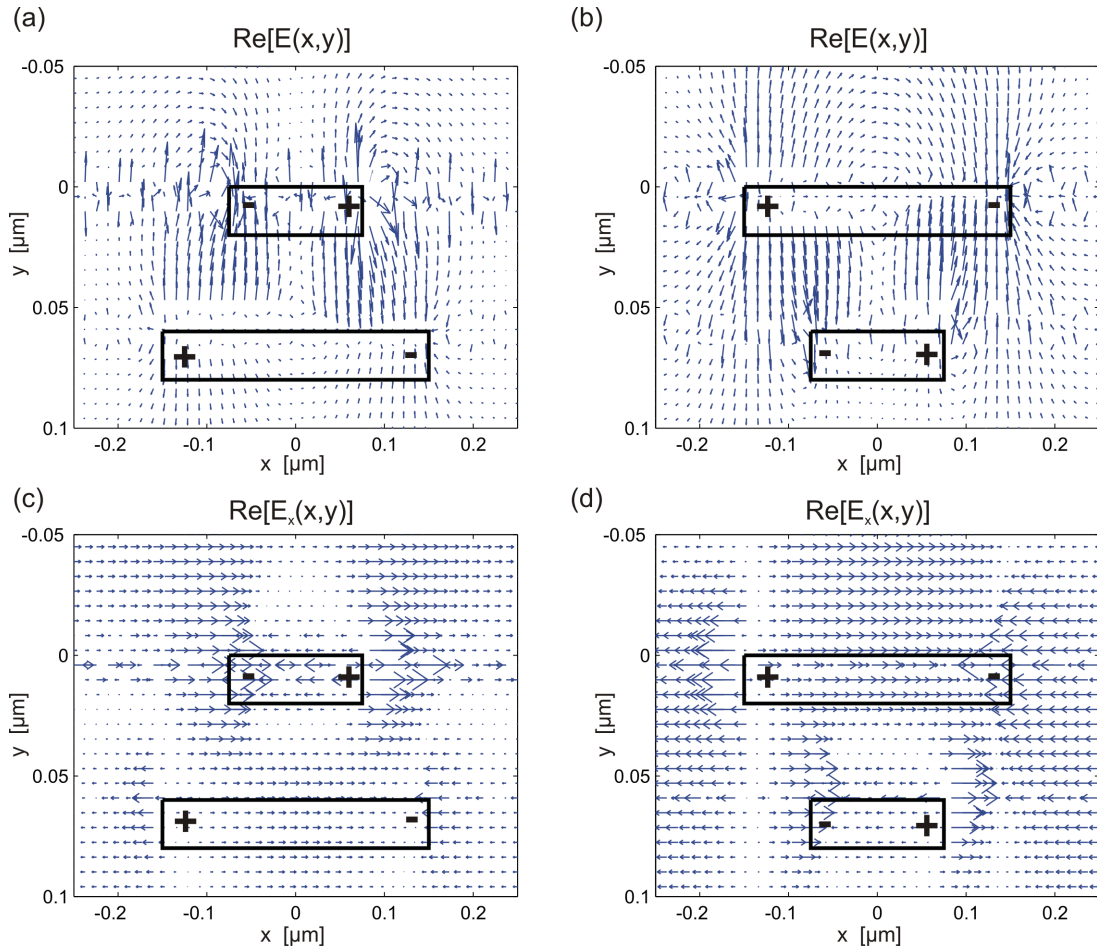
Figure 5.7: (a) and (b) - The electric field distributions for the structures with $\Delta L = -100\,\mathrm{nm}$ and $\Delta L = 100\,\mathrm{nm}$ at the eigenfrequency of the antisymmetric mode ($1.05\ \mathrm{\mu m^{-1}}$). (c) and (d) - The spatial distribution of x component of the electric fields for the structures with $\Delta L = -100\,\mathrm{nm}$ and $\Delta L = 100\,\mathrm{nm}$, respectively.

field than the phase of the smaller one x_1, however, it deviates from the phase of the electric field, due to the stronger influence of the oscillator x_2. As a result, at frequencies below the frequency of the magnetic resonance, the loop current orientation is reversed with respect to that of the structure with $\Delta L = 100\,\mathrm{nm}$.

The electric field distributions obtained in the rigorous numerical simulations confirm the results on the carrier dynamics derived with the oscillator model. In Fig. 5.7 the electric field distributions for the structures with $\Delta L = -100\,\mathrm{nm}$ and $\Delta L = 100\,\mathrm{nm}$ at the frequency of the antisymmetric mode ($1.05\ \mathrm{\mu m^{-1}}$) are shown. The real parts of the electric fields are presented in Figs. 5.7(a) and (b). In Figs. 5.7(c) and (d) the real parts of the x components of the electric fields are shown. One can see that the field distributions in both cases correspond to the ones of two dipoles oscillating out of phase. The orientations of the dipoles correspond to those predicted by the oscillator model.
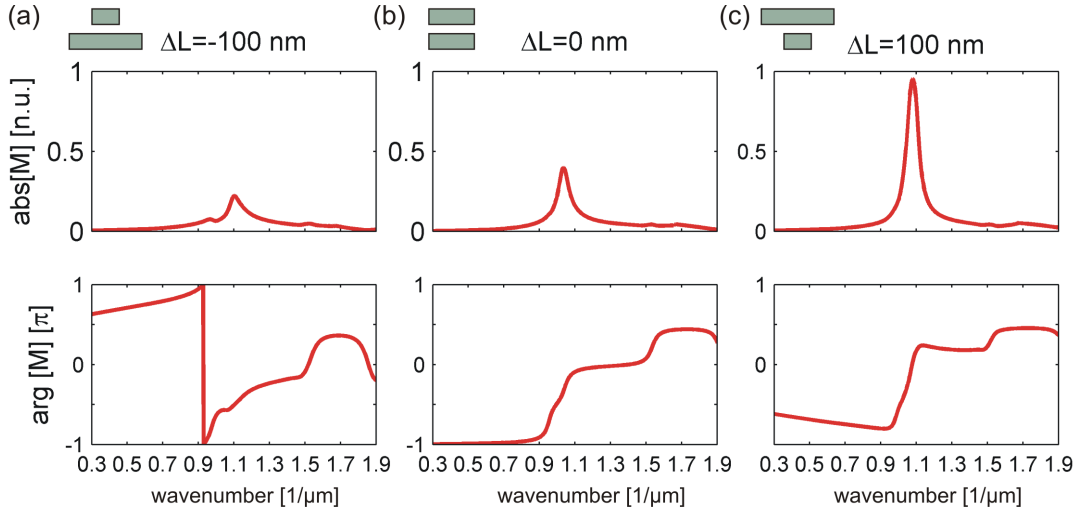
Figure 5.8: In the columns (a),(b),(c) - absolute values (in normalized unites) and phases of the magnetization for structures with $\Delta L = -100\,\text{nm}$, $\Delta L = 0\,\text{nm}$, and $\Delta L = 100\,\text{nm}$, respectively.

5.3.2 Magnetization of the double-wire MMs

The magnetizations for the structures with $\Delta L = -100\,\text{nm}$, $\Delta L = 0\,\text{nm}$, and $\Delta L = 100\,\text{nm}$ calculated according to Eq. (5.7) are shown in Fig. 5.8. The phase of the magnetization is given relative to the phase of the electric field of an incoming wave. It is seen that the absolute values and the phases of the magnetizations strongly depend on the asymmetry of the structure. The magnetization of the structure with $\Delta L = -100\,\text{nm}$ is smaller than the one of the structure with $\Delta L = 100\,\text{nm}$ and oscillates almost out of phase with respect to the electric field. The magnetization of the structure with $\Delta L = 100\,\text{nm}$, in turn, oscillates almost in phase with the electric field.

Though, the magnetic response of the double-wire structures is caused by the electric field of the incoming wave, it is reasonable to consider the magnetization with respect to the magnetic field of an incoming wave. This relation can be expressed introducing a complex coefficient $\chi\left(\omega\right) = \chi'\left(\omega\right) + i\chi''\left(\omega\right)$ which defines the relation between the magnetic field of the wave and the magnetization of a MM

$$\tilde{M}_z\left(y, \omega\right) = \chi\left(\omega\right) \tilde{B}_z\left(y, \omega\right). \tag{5.20}$$

The coefficient $\chi(\omega)$ can be easily derived from Eq. (5.7) using Eqs. (5.2) and (5.3) where the electric field is substituted with the expression

$$\widetilde{E}_x\left(y, \omega\right) = -\frac{\omega}{k_y(\omega)}\widetilde{B}_z(y, \omega), \tag{5.21}$$
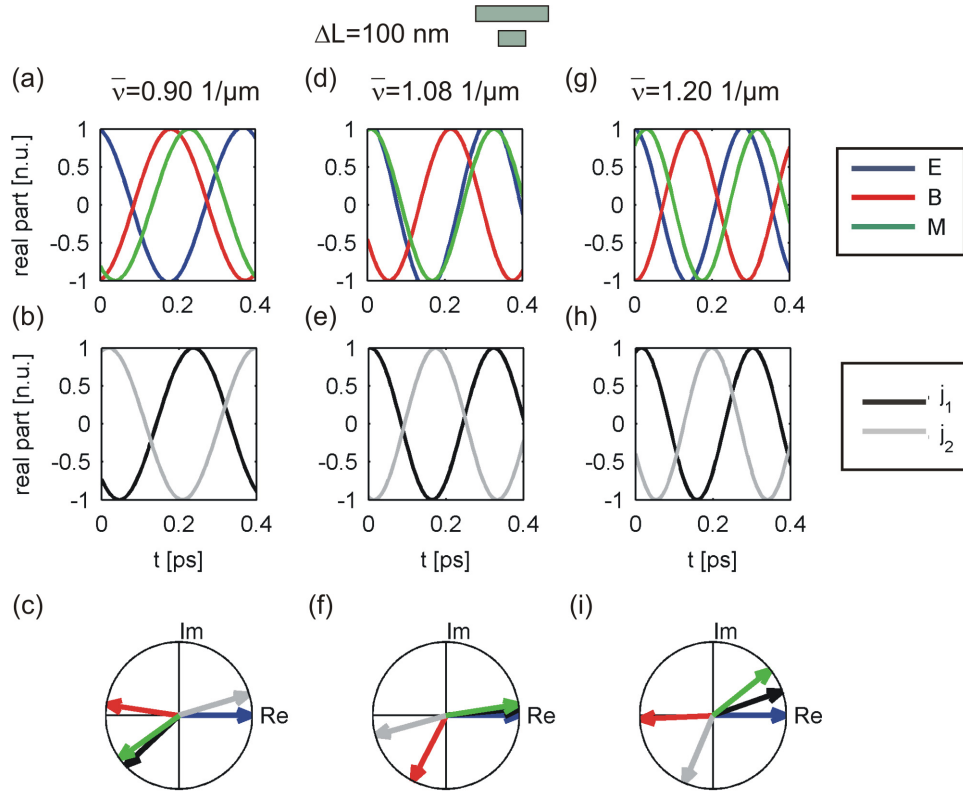
Figure 5.9: Phase relation between the electric field (blue), magnetic field (red), magnetization (green), current j_1 (black), and current j_2 (gray) are presented at the frequency 0.9 μm^{-1} in the left column (a)-(c), at 1.08 μm^{-1} in the central column (d)-(f), and at 1.2 μm^{-1} in the right column (g)-(i). Presented data is for the structure with $\Delta L = 100\,\text{nm}$.

describing the relation between the electric and magnetic fields in a plane wave.

The absolute value and the phase of χ for the structure with $\Delta L = 100\,\text{nm}$ are shown in Figs. 5.6(e) and (f). In the resonance the phase of χ is π (see Fig. 5.6(f)), i.e. the equivalent microscopic loop currents (Figs. 5.6(c) and (d)) produce a magnetization oscillating out of phase with the magnetic field. The phase relations between the fields, the magnetization and the currents at the frequencies below (0.9 μm^{-1}), at (1.08 μm^{-1}) and above (1.2 μm^{-1}) the resonance are illustrated in Fig. 5.9, where the normalized real parts of these quantities are shown. In Figs. 5.9(c),(f), and (i) the phase relations between the fields, the magnetization, and the currents are illustrated in phase diagrams. The absolute value and the phase of χ for the structure $\Delta L = -100\,\text{nm}$ is shown in Figs. 5.6(i) and (m). One can see that the microscopic currents of the structure with $\Delta L = -100\,\text{nm}$ produce a magnetization which is almost in phase with the magnetic field ($-\pi/2 < \arg(\chi) < \pi/2$), and only at frequencies above the resonance frequency the phase shift between the magnetization and the magnetic field becomes larger than $\pi/2$. The phase relations between the
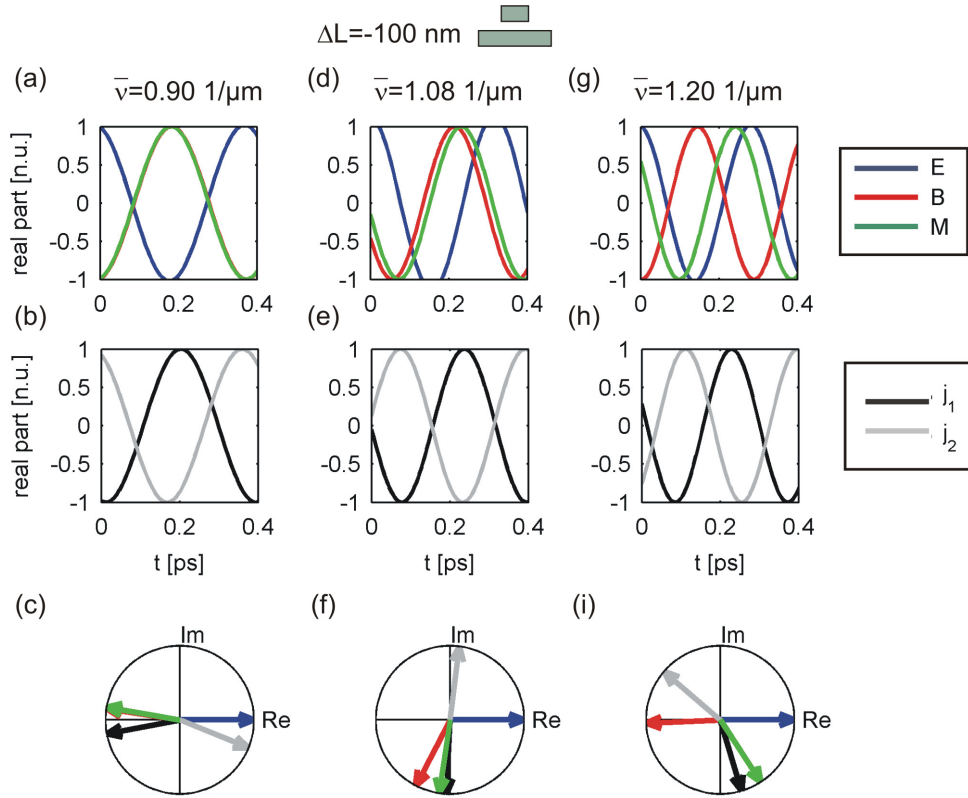
Figure 5.10: The same data as in Fig. 5.9 for the structure with $\Delta L = -100$ nm. Phase relation between the electric field (blue), magnetic field (red), magnetization (green), current j_1 (black), and current j_2 (gray) are presented at the frequency 0.9 μm^{-1} in the left column (a)-(c), at 1.08 μm^{-1} in the central column (d)-(f), and at 1.2 μm^{-1} in the right column (g)-(i).

fields, the magnetization and the currents at the frequencies below (0.9 μm^{-1}), at (1.08 μm^{-1}) and above (1.2 μm^{-1}) the resonance are shown in Fig. 5.10.

5.3.3 Effective magnetic permeability of the double-wire structures

The magnetic properties of materials are commonly described with the effective magnetic permeability $\mu_{\text{eff}}(\omega)$. The common definition of an effective magnetic permeability by

$$\widetilde{H}_z(\omega) = \frac{1}{\mu_0}\tilde{B}_z(\omega) - \tilde{M}_z(\omega) = \frac{1}{\mu_{\text{eff}}(\omega)\mu_0}\tilde{B}_z(\omega),$$

(5.22)

$$\mu_{\text{eff}}(\omega) = \frac{\tilde{B}_z(y,\omega)}{\tilde{B}_z(y,\omega) - \mu_0\tilde{M}_z(y,\omega)}$$

(5.23)

for plasmonic MMs has formal character only, because the magnetization of the structures is mainly caused by the electric field. The effective magnetic permeabilities calculated according to Eq. (5.23) for the structures with $\Delta L = 100$ nm and

$\Delta L = -100$ nm are shown in Fig. 5.6(g) and (n), respectively. It is seen that the larger the wire on the top, the lower the absolute value of the effective permeability. This may appear contradictory to the behavior of the magnetization shown in Fig. 5.8, where one can see that the absolute value of the magnetization grows with increasing the length of the upper wire. However, a thorough consideration of the relation between $\mu_{\text{eff}}(\omega)$ and the magnetization clears up this seeming discrepancy. According to Eq. (5.20) and Eq. (5.23) the absolute value of the permeability can be written as

$$|\mu_{\text{eff}}(\omega)|^2 = \frac{1}{(1 - \mu_0 \chi'(\omega))^2 + (\mu_0 \chi''(\omega))^2} \qquad (5.24)$$

and the real part as

$$Re\left[\mu_{\text{eff}}(\omega)\right] = \frac{(1 - \mu_0 \chi'(\omega))}{(1 - \mu_0 \chi'(\omega))^2 + (\mu_0 \chi''(\omega))^2}. \qquad (5.25)$$

Now one can see that, if the real parts of $\chi(\omega)$ increases, the sign of $\chi(\omega)$, i.e. the phase of the magnetization with respect to the magnetic field, defines whether $\mu_{\text{eff}}(\omega)$ increases or decreases.

Indeed, when the magnetization is in phase with the magnetic field $(\chi'(\omega) > 0)$ and grows, the absolute value of $\mu_{\text{eff}}(\omega)$ increases, as the denominator in Eq. (5.24) decreases. This is the case for structures with a negative ΔL, for which the phases of $\chi(\tilde{\nu})$ lie between $-\pi/2$ and $\pi/2$ (Fig. 5.6(m)). Further, if the magnetization increases and is out of phase with the magnetic field $(\chi'(\omega) < 0)$, $\mu_{\text{eff}}(\omega)$ decreases, as the denominator in Eq. (5.24) increases. This is the case for structures with positive ΔL, for which the phases of $\chi(\omega)$ lie between $\pi/2$ and $-\pi/2$ (Fig. 5.6(f)).

The real part of $\mu_{\text{eff}}(\omega)$ becomes negative if $\chi'(\omega)$ exceeds $1/\mu_0$, which means that the magnetization oscillates in phase with the magnetic field and is strong enough. Furthermore, if the magnetization is out of phase with the magnetic field the real part of $\mu_{\text{eff}}(\omega)$ is always positive.

5.4   Experimental verification

For experimental investigations of the magnetic properties of asymmetric double-wire structures, a set of samples was produced using the electron-beam lithography technique described in Sec. 3.3. An SEM image of one of the samples is shown in Fig. 5.11(a). The wires were made of gold $(d_{\text{Au}} = 20$ nm$)$ and separated by a MgO dielectric layer $(d_{\text{MgO}} = 30$ nm$)$ (see Fig. 5.11(b)). The period of the structure was 500 nm. Because of technological reasons, only the length L_1 of the upper wire was
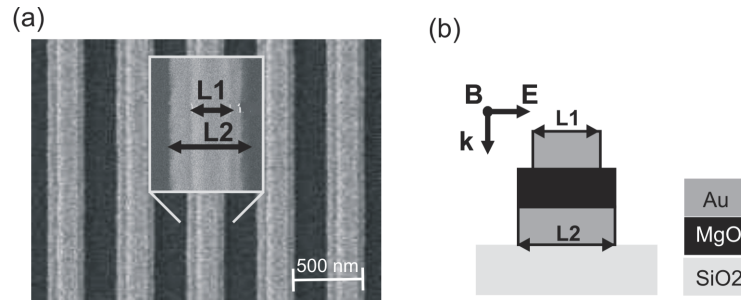
Figure 5.11: (a) - SEM image of the realized structure with $\Delta L = -40$ nm, (b) - arrangement of the structure in the experiment.
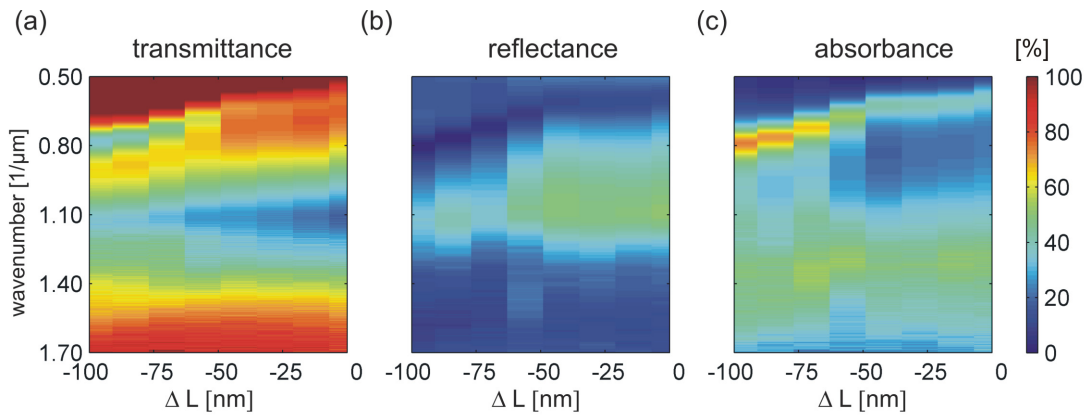

Figure 5.12: Measured transmittance, reflectance, and absorbance of a set of asymmetric double-wires. The wire at the bottom had the constant length ($L_2 = 260$ nm), whereas the length of the wire on the top ranged from 160 nm to 260 nm.

varied in the range from $L_1 = 160$ nm to $L_1 = 260$ nm, while the length of the wire L_2 on the bottom was kept at $L_2 = 260$ nm for all samples.

As the geometrical parameters of the structures can slightly vary along a wafer (due to technological inaccuracy), a set of ten samples on a compact area of 1 mm by 0.5 mm was produced, where the size of each sample was 1 mm x 50 μm. Such a compact arrangement of the samples assured that the observed effects were caused by the variation of the wire length only. The measurements of transmittance and reflectance spectra were performed using a Bruker Vertex 80 spectrometer combined with a Hyperion 2000 microscope. The light was focused on the set of the samples with an objective with NA = 0.4 and a certain sample was selected by an appropriate aperture setting.

The measured transmittance, reflectance, and absorbance spectra are shown in Fig. 5.12. As it was discussed in Sec. 5.2, symmetric and antisymmetric modes can be identified in the spectra by the maxima of reflectance and absorbance, respectively. In the absorbance the resonance corresponding to the excitation of the antisymmetric mode appears as a minimum at about 0.8 μm^{-1} and the symmetric mode as a
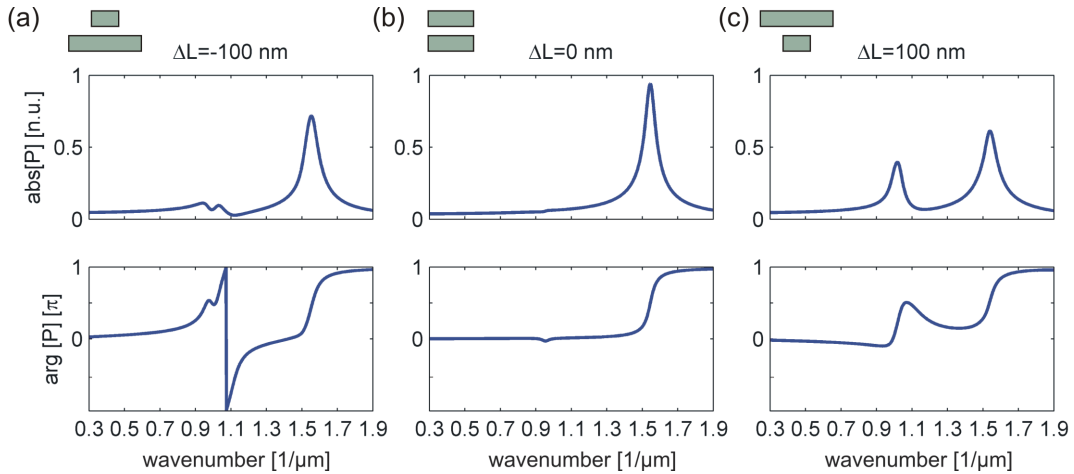
Figure 5.13: In the columns (a),(b),(c) - absolute values and phases of the polarization for structures with $\Delta L = -100$ nm, $\Delta L = 0$ nm, and $\Delta L = 100$ nm, respectively.

minimum at about 1.1 μm^{-1}. The difference in the absolute values of the resonance positions in the numerical simulations and in the experiment is due to the different refractive indices of the spacer and slightly different lengths of the wires. In addition, in the presence of the substrate the wire on the bottom becomes effectively longer. As a result, the spectral separation of the resonances for $\Delta L = 0$ nm is smaller for the experimental system with a substrate than for the system without a substrate considered earlier. Nevertheless, according to the predictions of the theory, splitting of the symmetric and antisymmetric modes becomes weaker when ΔL tends to -100 nm. It is interesting to note that in both experiment and simulation the absorption of the metamaterial at the antisymmetric resonance is maximal (Fig. 2(c) and Fig. 5.12(c)) for negative ΔL and decreases when ΔL becomes zero, whereas the reflectance of the metamaterial (Fig. 2(b) and Fig. 5.12(b)) increases. This behavior can be explained by the increase of the electric dipole moment of the double-wire structure as ΔL becomes positive (the length of the wire on the top increases). The polarization of the theoretically considered structures are shown in Fig. 5.13. Indeed, in the antisymmetric resonance, the polarization, which is proportional to the dipole moments of the double-wires, is larger for the structure with $\Delta L = 100$ nm than for the structure with $\Delta L = -100$ nm.

To access the effective magnetic permeabilities of the MM's layers, the combined method was employed. The experimental method based on the phase measurements could not be used, as the area of the samples was too small. Since the simulated transmittances and reflectances showed good agreement with the experimental ones, the effective parameters could be retrieved from the simulated complex transmission and reflection coefficients.
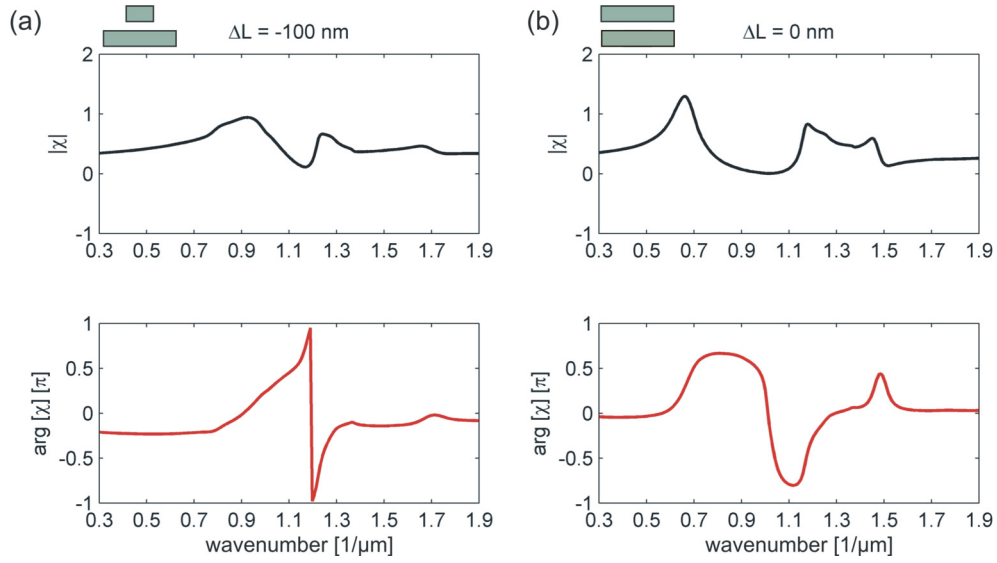
Figure 5.14: Absolute values and phases of χ for the experimental structures with $\Delta L = -100\,\text{nm}$ and $\Delta L = 0\,\text{nm}$.

The coefficients χ characterizing the magnetic moment of the structures can be expressed as a function of the effective magnetic permeability using Eq. (5.20) and Eq. (5.23). The absolute values and phases of the parameters χ for the structures with $\Delta L = 0\,\text{nm}$ and $\Delta L = -100\,\text{nm}$ are presented in Fig. 5.14. An interpretation of the absolute values of χ can be misleading, because the amount of metal in the experimental systems was not conserved (L_2=constant for all structures). Accordingly, the phase of the coefficients χ is a more appropriate parameter in this case. It is seen that for the structure with $\Delta L = -100\,\text{nm}$ the magnetic moment oscillates almost in phase with the magnetic field ($\arg[\chi] \approx 0$) at the eigenfrequency of the antisymmetric mode ($0.85\,\mu\text{m}^{-1}$). The phase delay increases when the length of the wire on the top becomes larger. For the structure with $\Delta L = 0\,\text{nm}$ the phase delay is about $\pi/4$ at the frequency $0.65\,\mu\text{m}^{-1}$. Thus, the orientation of the magnetic moment relative to the magnetic field in the experimental system corresponds to the predictions of the analytical model.

Chapter summary

In this chapter theoretical and experimental investigations of the influence of the asymmetry on the magnetic properties of double-wire structures were presented [102]. The analytical description of the structures required the extension of the multipole model presented in Ref. [59] to the asymmetric case. The connection between the parameters of the oscillators in the analytical model and the real geometry was found through fitting of the analytically obtained dispersions to the numerically calculated ones. The comparison of the parameters obtained from the simulations

of the single-wire and double-wire structures revealed an interaction between the neighboring wires in the lateral direction. This interaction is not directly included in the model. Nevertheless, it can be taken into account by increasing the effective mass of the oscillators in the double-wire configuration in comparison to that for the single-wire configuration. It was also shown that the interaction between the wires in a double-wire structure can be qualitatively described as the interaction of two coupled dipoles.

The investigation verified that the magnitude of the magnetization and the phase shift relative to the magnetic field depends strongly on the configuration of the system. In general, the dynamics of the system is dominated by the larger wire, where plasmon oscillations follow the external electric field. This defines the orientation of the effective micro currents in the double-wire structure and, as a result, the orientation and strength of the magnetic moment. In the system where the larger wire has the top position the magnetic moment of the system oscillates almost out of phase relative to the magnetic field of the exciting wave. In the system where the larger wire is on the bottom the resulting magnetic moment oscillates almost in phase relative to the magnetic field. In this case, the effective magnetic permeability of the MM becomes negative. These results obtained using the theoretical model were verified by the experiment.

Chapter 6

Conclusions and outlook

The main aim of this thesis was the design, realization, and characterization of optical NIMs. Due to the nanometer dimensions of the constitutive elements of optical MMs, their realization is a challenging technological task. Therefore, in the first years of the work the main efforts were dedicated to the establishment of the technological process for the sample fabrication. The contribution to the development of the fabrication process was made by providing the design, the optical characterization and the analysis of the optical properties of the MM samples. During this work the main design guidelines for the realization of double element NIMs using the electron-beam lithography incorporated in the layer-by-layer fabrication technique were formulated.

In the framework of the effective medium approach the optical response of the investigated NIMs is described using effective electric permittivity and permeability. Consequently, the condition of a negative index material derived for the permittivity and permeability of homogeneous materials can be used as a criterion for the NIM design. According to the condition of a NIM either the real part of the permittivity or permeability has to be negative. A negative real part of the effective permeability of fabricated NIMs was realized using continuous metallic wires possessing the EM response of a diluted metal. An effective magnetic permeability satisfying the condition of a NIM was designed employing plasmonic double cut-wires supporting an antisymmetric mode characterized with a nonzero magnetic moment in the unit cell of MMs.

Commonly, the main ideas about the layout of the unit cell are drawn from the analysis of the dependence of the localized plasmon polariton resonances on the geometry of the metallic particles of simple shapes. The eigenmodes of the cut-wires are qualitatively described employing the hybridization model for localized plasmon polaritons. Nevertheless, for a long time, the main tool to design metaatoms was the rigorous numerical modeling, since an analytical model describing the functionality

93

of plasmonic metaatoms has only been developed recently.

In this thesis rigorous numerical simulations based on FMM were used for the design and analysis of NIM's optical properties. The detailed study of the accuracy of the technological process and the sensitivity of the metaatom resonance to the precision of the geometry realization resulted in the design and fabrication of a double-element NIM at a wavelength of 2.2 μm. Additionally, it was found that tuning different geometrical parameters of the structures may result in a quite similar spectral behavior of the plasmonic resonances. This ambiguity complicates the fitting of the geometry assumed for the numerical simulations to reproduce the real fabricated structures. As a result, a good agreement of the simulated and measured spectra, required to employ the combined method for the determination of the effective refractive index of a NIM, is hard to achieve.

This was the motivation for the development of an experimental method enabling the characterization of the effective refractive index without resorting to simulations. The developed method allowed for measurements of the phases and amplitudes of the complex transmission and reflection coefficients of a MM film. An experimental technique based on the white-light spectral interferometry was realized and enabled phase measurements in transmission and reflection of MMs with an accuracy of ±0.02 rad. In parallel, the transmittance and reflectance measurements were conducted with a commercially available spectrometer. In comparison to the techniques developed by other groups to verify the effective refractive index, the developed method can be used as a routine technique for the determination of the effective refractive index in a broad spectral range from 0.65 μm to 1.7 μm. The experimental method allows for the determination of the effective refractive index with an accuracy of ±0.04 in the real part.

Additionally, the experimental access to the complex transmission and reflection coefficients enabled the verification of the combined method based on the combination of the simulated and measured data to determine the effective refractive index of a MM. It was shown that the combined method provides accurate values of the effective refractive index only when a good agreement between the measured and simulated spectra in a broad spectral range is achieved.

The later development of the multipole model providing insight into the internal dynamics of plasmonic metaatoms took the design of metaatoms to a qualitatively new level. The analytical model, providing a description of the cut-wire dynamics and facilitating its analysis, was employed to investigate magnetic properties of asymmetric double-wires. To perform this analysis, the multipole model was expanded to the case of an asymmetric system. The investigations have shown that the structural asymmetry influences the magnetic response of the double-wires sig-

nificantly. The magnetic response of a double-wire system is connected with the excitation of the antisymmetric resonance, where the carriers in each wire oscillate out of phase. In a system of double-wires of different lengths the carrier oscillations in the larger wire follow the electric field of the excitation. As a result, depending on the position of the large wire with respect to the exciting wave, the effective loop current in the system has different orientations. In the configuration where the larger wire has the top position, the effective loop current produces a magnetic moment that is opposite to the magnetic field of the exciting wave. In this configuration, the excitation conditions for the antisymmetric mode are optimal, which causes a strong magnetic moment. In the configuration where the larger wire lies on the bottom the resulting loop current gives rise to a magnetic moment which is almost parallel to the magnetic field of the exciting wave. However, the magnetic moment is weak, as the excitation conditions are not optimal. The effective permeability, in turn, becomes negative only in the case when the magnetization oscillates in phase with the magnetic field. Thus the configuration with the larger wire on the bottom is preferable for the realization of a NIM. The results obtained for the magnetization of the asymmetric double-wires were proved experimentally.

According to the results produced in this thesis, the following directions for further research can be formulated.

New designs of metaatoms should be developed to overcome the main drawbacks of the contemporary MMs, namely the inhomogeneity and high absorption. Improving the homogeneity of the MMs is connected to the reduction of the sizes of the metaatoms relative to the operating wavelength. For the metaatoms based on cut-wires, one of the possible ways to increase the homogeneity of the system would be decreasing the spacer thickness down to the nanometer scale. This will result in the decreasing of the eigenfrequency of the antisymmetric resonance, which can be tuned to a certain extend towards the operating frequency by the variation of the linear dimensions of the wires. The magnetic response of the system can be additionally improved by introducing asymmetry into the geometry of the system. The establishment of new fabrication techniques like atomic layer deposition (ALD) will allow the realization of spacer layers of several nanometers with atomic precision.

To improve the efficiency of the MMs several strategies can be followed. One of them is the reduction of the absorption in the metals by improving the quality of the crystallographic structure of thin metallic films. Also using plasmonic materials with high plasma frequency would increase the efficiency of NIMs. The other way to improve the efficiency of MMs is the use of active materials to compensate the

losses [45].

Regarding the experimental methods for the characterization of the optical properties of MMs, the work should be continued to provide experimental characterization of the complete dispersion relation of MMs. This, in turn, requires realization of angle resolved phase measurements in a broad spectral range. Furthermore, as the technological progress allows for the realization of complex three dimensional metaatoms providing new functionality of MMs, the development of new experimental techniques is urgent. The realization of chiral materials [150], for example, requires the development of methods for measurements of the complex Jones matrix [151]. The development of the experimental method for cross polarization phase measurements based on the technique presented in this work is ongoing.

Zusammenfassung

Die vorliegende Arbeit beschäftigt sich mit künstlichen nanostrukturierten optischen Materialien - Metamaterialien, welche optische Eigenschaften besitzen, die in natürlichen Materialien nicht vorkommen. Die Metamaterialien bestehen aus Elementarzellen deren Gröe kleiner als die Wellenlänge des Lichtes ist und können demzufolge als effektive Medien betrachtet werden. Dementsprechend werden die optischen Eigenschaften eines Metamaterials mit effektiven Parametern wie effektive Brechzahl und Impedanz oder effektive elektrische Permittivität und magnetische Permeabilität beschrieben. Die effektiven optischen Parameter vom Metamaterialien werden, in Analogie zu natürlichen Materialien, durch die elektromagnetischen Eigenschaften der Elementarzellen oder "Metaatome" bestimmt und können durch angepasstes Design gezielt verändert werden.

Das Ziel dieser Arbeit war die Formulierung von Designgrundsätzen für Metamaterialien mit einer negativen Brechzahl im optischen Spektralbereich und die Entwicklung experimenteller Methoden für die Charakterisierung ihrer optischen Eigenschaften. Die Designstrategien für doppelt-elementige Metamaterialien wurden anhand der Evaluierung der auf Elektronstrahllithographie basierenden Herstellungsmethode erarbeitet. In Rahmen dieser Arbeit wurde die Abhängigkeit der optischen Eigenschaften von Metamaterialien von Herstellungsungenauigkeiten experimentell und mittels rigoroser Simulationen untersucht. Dabei wurden alle durch den Herstellungsprozess bedingte Limitierungen berücksichtigt. Als Ergebnis wurde ein Metamaterial im nahinfraroten Spektralbereich mit einer negativen Brechzahl erfolgreich realisiert.

Die Möglichkeit zur weiteren Optimierung der optischen Eigenschaften der Metamaterialien durch Symmetriebrechung der Geometrie der Metaatome, wurde analytisch anhand eines Multipol-Modells und experimentell erforscht. Es konnte gezeigt werden, dass die Asymmetrie einen erheblichen Einfluss auf die magnetischen Eigenschaften der Metaatome hat und die Steuerung der effektiven magnetischen Permeabilität von Metamaterialien in weiten Bereichen erlaubt.

Für die vollständige und präzise Bestimmung der Brechzahl von Metamaterialien im optischen Spektralbereich wurde eine experimentelle Methode entwickelt, welche auf der interferometrischen Bestimmung der Transferfunktion eines optischen Metamaterials beruht. Für diesen Zweck wurde ein Aufbau für Phasenmessungen in Transmission und Reflexion im sichtbaren und nahinfraroten Spektralbereich entwickelt.

A. Bibliography

Bibliography

[1] V. G. Veselago, "The electrodynamics of substances with simultaneously negative values of permittivity and mermeability," Phys. Uspekhi **10**, 509–514 (1968).

[2] A. Schuster, *An Introduction to the Theory of Optics* (Arnold, London, 1904).

[3] H. Lamb, "On group-velocity," Proc. Lond. Math. Soc. **1**, 473479 (1904).

[4] L. I. Mandelshtam, "Group velocity in a crystal lattice," Zh. Eksp. Teor. Fiz. **15**, 475478 (1945).

[5] J. Pendry, A. Holden, D. Robbins, and W. Stewart, "Magnetism from conductors and enhanced nonlinear phenomena," IEEE Trans. Microw. Theory Tech. **47**, 2075 –2084 (1999).

[6] D. R. Smith, W. J. Padilla, D. C. Vier, S. C. Nemat-Nasser, and S. Schultz, "Composite medium with simultaneously negative permeability and permittivity," Phys. Rev. Lett. **84**, 4184–4187 (2000).

[7] J. B. Pendry, A. J. Holden, W. J. Stewart, and I. Youngs, "Extremely low frequency plasmons in metallic mesostructures," Phys. Rev. Lett. **76**, 4773–4776 (1996).

[8] R. A. Shelby, D. R. Smith, and S. Schultz, "Experimental Verification of a Negative Index of Refraction," Science **292**, 77–79 (2001).

[9] J. B. Pendry, "Negative Refraction Makes a Perfect Lens," Phys. Rev. Lett. **85**, 3966–3969 (2000).

[10] J. T. Shen and P. M. Platzman, "Near field imaging with negative dielectric constant lenses," Appl. Phys. Lett. **80**, 3286–3288 (2002).

[11] D. R. Smith, D. Schurig, M. Rosenbluth, S. Schultz, S. A. Ramakrishna, and J. B. Pendry, "Limitations on subdiffraction imaging with a negative refractive index slab," Appl. Phys. Lett. **82**, 1506–1508 (2003).

[12] P. Kolinko and D. Smith, "Numerical study of electromagnetic waves interacting with negative index materials," Opt. Express **11**, 640–648 (2003).

[13] J. Zhu and G. V. Eleftheriades, "Experimental verification of overcoming the diffraction limit with a volumetric veselago-pendry transmission-line lens," Phys. Rev. Lett. **101**, 013 902 (2008).

[14] J. B. Pendry, D. Schurig, and D. R. Smith, "Controlling electromagnetic fields," Science **312**, 1780–1782 (2006).

[15] U. Leonhardt, "Optical Conformal Mapping," Science **312**, 1777–1780 (2006).

[16] D. Schurig, J. J. Mock, B. J. Justice, S. A. Cummer, J. B. Pendry, A. F. Starr, and D. R. Smith, "Metamaterial Electromagnetic Cloak at Microwave Frequencies," Science **314**, 977–980 (2006).

[17] S. Linden, C. Enkrich, M. Wegener, J. Zhou, T. Koschny, and C. M. Soukoulis, "Magnetic Response of Metamaterials at 100 Terahertz," Science **306**, 1351–1353 (2004).

[18] J. Zhou, T. Koschny, M. Kafesaki, E. N. Economou, J. B. Pendry, and C. M. Soukoulis, "Saturation of the magnetic response of split-ring resonators at optical frequencies," Phys. Rev. Lett. **95**, 223 902 (2005).

[19] N. Johnson, A. Khokhar, H. Chong, R. De La Rue, T. Antosiewicz, and S. McMeekin, "A review of size and geometrical factors influencing resonant frequencies in metamaterials," Opto-Electron. Rev. **14**, 187–191 (2006).

[20] N. P. Johnson, A. Z. Khokhar, H. M. H. Chong, and S. McMeekin, "Characterisation at infrared wavelengths of metamaterials formed by thin-film metallic split-ring resonator arrays on silicon," Electron. Lett. **42**, 1117 (2006).

[21] V. A. Podolskiy, A. K. Sarychev, and V. M. Shalaev, "Plasmon modes in metal nanowires and left-handed materials," J. Nonlin. Opt. Phys. Mater. **11**, 6574 (2002).

[22] V. M. Shalaev, W. Cai, U. K. Chettiar, H.-K. Yuan, A. K. Sarychev, V. P. Drachev, and A. V. Kildishev, "Negative index of refraction in optical metamaterials," Opt. Lett. **30**, 3356–3358 (2005).

[23] G. Dolling, C. Enkrich, M. Wegener, J. F. Zhou, C. M. Soukoulis, and S. Linden, "Cut-wire pairs and plate pairs as magnetic atoms for optical metamaterials," Opt. Lett. **30**, 3198–3200 (2005).

[24] A. V. Kildishev, W. Cai, U. K. Chettiar, H.-K. Yuan, A. K. Sarychev, V. P. Drachev, and V. M. Shalaev, "Negative refractive index in optics of metaldielectric composites," J. Opt. Soc. Am. B **23**, 423–433 (2006).

[25] S. Zhang, W. Fan, N. C. Panoiu, K. J. Malloy, R. M. Osgood, and S. R. J. Brueck, "Experimental demonstration of near-Infrared negative-Index metamaterials," Phys. Rev. Lett. **95**, 137 404 (2005).

[26] G. Dolling, C. Enkrich, M. Wegener, C. M. Soukoulis, and S. Linden, "Simultaneous negative phase and group velocity of light in a metamaterial," Science **312**, 892–894 (2006).

[27] G. Dolling, C. Enkrich, M. Wegener, C. M. Soukoulis, and S. Linden, "Low-loss negative-index metamaterial at telecommunication wavelengths," Opt. Lett. **31**, 1800–1802 (2006).

[28] U. K. Chettiar, A. V. Kildishev, H.-K. Yuan, W. Cai, S. Xiao, V. P. Drachev, and V. M. Shalaev, "Dual-band negative index metamaterial: double negative at 813 nm and single negative at 772 nm," Opt. Lett. **32**, 1671–1673 (2007).

[29] G. Dolling, M. Wegener, C. M. Soukoulis, and S. Linden, "Negative-index metamaterial at 780 nm wavelength," Opt. Lett. **32**, 53–55 (2007).

[30] J. Valentine, S. Zhang, T. Zentgraf, E. Ulin-Avila, D. A. Genov, G. Bartal, and X. Zhang, "Three-dimensional optical metamaterial with a negative refractive index," Nature **455**, 376–379 (2008).

[31] N. Liu, H. Guo, L. Fu, S. Kaiser, H. Schweizer, and H. Giessen, "Three-dimensional photonic metamaterials at optical frequencies," Nat. Mater. **7**, 31–37 (2008).

[32] C. M. Soukoulis and M. Wegener, "Optical MetamaterialsMore Bulky and Less Lossy," Science **330**, 1633–1634 (2010).

[33] V. Drachev, W. Cai, U. Chettiar, H. Yuan, A. Sarychev, A. Kildishev, G. Klimeck, and V. Shalaev, "Experimental verification of an optical negativeindex material," Laser Phys. Lett. **3**, 49–55 (2006).

[34] V. M. Agranovich and Y. N. Gartstein, "Spatial dispersion and negative refraction of light," UFN **176**, 10511068 (2006).

[35] A. I. Căbuz, D. Felbacq, and D. Cassagne, "Spatial dispersion in negative-index composite metamaterials," Phys. Rev. A **77**, 013 807 (2008).

[36] C. Rockstuhl, C. Menzel, T. Paul, T. Pertsch, and F. Lederer, "Light propagation in fishnet structure metamaterials," Phys. Rev. B **78**, 155 101 (2008).

[37] C. R. Simovski, "Bloch material parameters of magneto-dielectric metamaterials and the concept of Bloch lattices," Metamaterials **1**, 62 – 80 (2007).

[38] C. R. Simovski and S. A. Tretyakov, "Local constitutive parameters of metamaterials from an effective-medium perspective," Phys. Rev. B **75**, 195 111 (2007).

[39] C. R. Simovski and S. A. Tretyakov, "On effective electromagnetic parameters of artificial nanostructured magnetic materials," Photonic. Nanostruct. **8**, 254 – 263 (2010).

[40] D. R. Smith, "Analytic expressions for the constitutive parameters of magnetoelectric metamaterials," Phys. Rev. E **81**, 036 605 (2010).

[41] J. Yang, C. Sauvan, T. Paul, C. Rockstuhl, F. Lederer, and P. Lalanne, "Retrieving the effective parameters of metamaterials from the single interface scattering problem," Appl. Phys. Lett. **97** (2010).

[42] C. Menzel, T. Paul, C. Rockstuhl, T. Pertsch, S. Tretyakov, and F. Lederer, "Validity of effective material parameters for optical fishnet metamaterials," Phys. Rev. B **81**, 035 320 (2010).

[43] C. Menzel, C. Helgert, J. Üpping, C. Rockstuhl, E.-B. Kley, R. B. Wehrspohn, T. Pertsch, and F. Lederer, "Angular resolved effective optical properties of a Swiss cross metamaterial," Appl. Phys. Lett. **95**, 131 104 (2009).

[44] S. Wuestner, A. Pusch, K. L. Tsakmakidis, J. M. Hamm, and O. Hess, "Overcoming losses with gain in a negative refractive index metamaterial," Phys. Rev. Lett. **105**, 127 401 (2010).

[45] S. Xiao, V. P. Drachev, A. V. Kildishev, X. Ni, U. K. Chettiar, H.-K. Yuan, and V. M. Shalaev, "Loss-free and active optical negative-index metamaterials," Nature **466**, 735–738 (2010).

[46] A. Boltasseva and H. A. Atwater, "Low-Loss Plasmonic Metamaterials," Science **331**, 290–291 (2011).

[47] J. Zhou, L. Zhang, G. Tuttle, T. Koschny, and C. M. Soukoulis, "Negative index materials using simple short wire pairs," Phys. Rev. B **73**, 041 101 (2006).

[48] K. Guven, M. D. Caliskan, and E. Ozbay, "Experimental observation of left-handed transmission in a bilayer metamaterial under normal-to-plane propagation," Opt. Express **14**, 8685–8693 (2006).

[49] K. Guven, A. O. Cakmak, M. D. Caliskan, T. F. Gundogdu, M. Kafesaki, C. M. Soukoulis, and E. Ozbay, "Bilayer metamaterial: analysis of left-handed transmission and retrieval of effective medium parameters," J. Opt. A-Pure Appl. Op. **9**, S361–S365 (2007).

[50] T. F. Gundogdu, N. Katsarakis, M. Kafesaki, R. S. Penciu, G. Konstantinidis, A. Kostopoulos, E. N. Economou, and C. M. Soukoulis, "Negative index short-slab pair and continuous wires metamaterials in the far infrared regime," Opt. Express **16**, 9173–9180 (2008).

[51] B. Kanté, S. N. Burokur, A. Sellier, A. de Lustrac, and J.-M. Lourtioz, "Controlling plasmon hybridization for negative refraction metamaterials," Phys. Rev. B **79**, 075 121 (2009).

[52] D. A. Powell, M. Lapine, M. V. Gorkunov, I. V. Shadrivov, and Y. S. Kivshar, "Metamaterial tuning by manipulation of near-field interaction," Phys. Rev. B **82**, 155 128 (2010).

[53] R. Singh, I. A. I. Al-Naib, M. Koch, and W. Zhang, "Asymmetric planar terahertz metamaterials," Opt. Express **18**, 13 044–13 050 (2010).

[54] Z.-G. Dong, H. Liu, M.-X. Xu, T. Li, S.-M. Wang, J.-X. Cao, S.-N. Zhu, and X. Zhang, "Role of asymmetric environment on the dark mode excitation in metamaterial analogue of electromagnetically-induced transparency," Opt. Express **18**, 22 412–22 417 (2010).

[55] K. Aydin, I. M. Pryce, and H. A. Atwater, "Symmetry breaking and strong coupling in planar optical metamaterials," Opt. Express **18**, 13 407–13 417 (2010).

[56] M. Decker, S. Linden, and M. Wegener, "Coupling effects in low-symmetry planar split-ring resonator arrays," Opt. Lett. **34**, 1579–1581 (2009).

[57] T. Pakizeh, A. Dmitriev, M. S. Abrishamian, N. Granpayeh, and M. Kaell, "Structural asymmetry and induced optical magnetism in plasmonic nanosandwiches," J. Opt. Soc. Am. B **25**, 659–667 (2008).

[58] B. Lahiri, A. Z. Khokhar, R. M. De La Rue, S. G. McMeekin, and N. P. Johnson, "Asymmetric split ring resonators for optical sensing of organic materials," Opt. Express **17**, 1107–1115 (2009).

[59] J. Petschulat, C. Menzel, A. Chipouline, C. Rockstuhl, A. Tünnermann, F. Lederer, and T. Pertsch, "Multipole approach to metamaterials," Phys. Rev. A **78**, 043 811 (2008).

[60] J. Petschulat, *The Multipole Description of Complex Plasmonic Nanoparticle*, Ph.D. thesis, Friedrich-Schiller-Universitt Jena (2011).

[61] R. A. Depine and A. Lakhtakia, "A new condition to identify isotropic dielectric-magnetic materials displaying negative phase velocity," Microw. Opt. Techn. Lett. **41**, 315–316 (2004).

[62] C. Rockstuhl, T. Zentgraf, E. Pshenay-Severin, J. Petschulat, A. Chipouline, J. Kuhl, T. Pertsch, H. Giessen, and F. Lederer, "The origin of magnetic polarizability in metamaterials at optical frequencies - an electrodynamic approach," Opt. Express **15**, 8871–8883 (2007).

[63] N.-H. Shen, S. Foteinopoulou, M. Kafesaki, T. Koschny, E. Ozbay, E. N. Economou, and C. M. Soukoulis, "Compact planar far-field superlens based on anisotropic left-handed metamaterials," Phys. Rev. B **80**, 115 123 (2009).

[64] S. F. Maier, *Plasmonics: Fundamental and Applications* (Springer, 2007).

[65] J. D. Jackson, *Classical Electrodynamics* (Wiley, New York, 1975).

[66] C. F. Bohren and D. R. Huffman, *Absorption and Scattering of Light by Small Particles* (Wiley-VCH, 1998).

[67] P. Nordlander, C. Oubre, E. Prodan, K. Li, and M. I. Stockman, "Plasmon Hybridization in Nanoparticle Dimers," Nano Lett. **4**, 899–903 (2004).

[68] L. Chuntonov and G. Haran, "Trimeric Plasmonic Molecules: The Role of Symmetry," Nano Lett. **11**, 24402445 (2011).

[69] E. Prodan, C. Radloff, N. Halas, and P. Nordlander, "A hybridization model for the plasmon response of complex nanostructures," Science **302**, 419–422 (2003).

[70] H. Wang, Y. Wu, B. Lassiter, C. L. Nehl, J. H. Hafner, P. Nordlander, and N. J. Halas, "Symmetry breaking in individual plasmonic nanoparticles," P. Natl. Acad. Sci. **103**, 10 856–10 860 (2006).

[71] N. Liu, H. Guo, L. Fu, S. Kaiser, H. Schweizer, and H. Giessen, "Plasmon hybridization in stacked cut-wire metamaterials," Adv. Mat. **19**, 3628 (2007).

[72] H. Guo, N. Liu, L. Fu, T. P. Meyrath, T. Zentgraf, H. Schweizer, and H. Giessen, "Resonance hybridization in double split-ring resonator metamaterials," Opt. Express **15**, 12 095–12 101 (2007).

[73] C. Tserkezis, N. Papanikolaou, G. Gantzounis, and N. Stefanou, "Understanding artificial optical magnetism of periodic metal-dielectric-metal layered structures," Phys. Rev. B **78**, 165 114 (2008).

[74] H. Liu, Y. M. Liu, T. Li, S. Wang, S. Zhu, and X. Zhang, "Coupled magnetic plasmons in metamaterials," Phys. Stat. Sol. **246**, 1521–3951 (2009).

[75] P. B. Johnson and R. W. Christy, "Optical constants of the noble metals," Phys. Rev. B **6**, 4370–4379 (1972).

[76] D. W. Lynch and W. Hunter, *Handbook of Optical Constants of Solids* (Academic Press Inc, 1997).

[77] M. J. Weber, *Handbook of optical materials* (CRC: New York, 2003).

[78] D. Beaglehole, M. De Crescenzi, M. L. Thèye, and G. Vuye, "Dielectric constant of gold, copper, and gold-copper alloys between 18 and 35 eV," Phys. Rev. B **19**, 6303–6314 (1979).

[79] H. Hövel, S. Fritz, A. Hilger, U. Kreibig, and M. Vollmer, "Width of cluster plasmon resonances: Bulk dielectric functions and chemical interface damping," Phys. Rev. B **48**, 18 178–18 188 (1993).

[80] A. Pinchuk, U. Kreibig, and A. Hilger, "Optical properties of metallic nanoparticles: influence of interface effects and interband transitions," Surf. Sci. **557**, 269 – 280 (2004).

[81] K.-P. Chen, V. P. Drachev, J. D. Borneman, A. V. Kildishev, and V. M. Shalaev, "Drude Relaxation Rate in Grained Gold Nanoantennas," Nano Lett. **10**, 916–922 (2010).

[82] S. Link and M. A. El-Sayed, "Spectral Properties and Relaxation Dynamics of Surface Plasmon Electronic Oscillations in Gold and Silver Nanodots and Nanorods," J. Phys. Chem. B **103**, 8410–8426 (1999).

[83] U. Kreibig and C. v. Fragstein, "The limitation of electron mean free path in small silver particles," Z. Phys. A-Hadron. Nucl. **224**, 307–323 (1969).

[84] U. Kreibig, "Kramers Kronig analysis of the optical properties of small silver particles," Z. Phys. A-Hadron. Nucl. **234**, 307–318 (1970).

[85] U. Kreibig and L. Genzel, "Optical absorption of small metallic particles," Surf. Sci. **156**, 678 – 700 (1985).

[86] S. Link, C. Burda, Z. L. Wang, and M. A. El-Sayed, "Electron dynamics in gold and gold–silver alloy nanoparticles: The influence of a nonequilibrium electron distribution and the size dependence of the electron–phonon relaxation," J. Chem. Phys. **111**, 1255–1264 (1999).

[87] S. L. Logunov, T. S. Ahmadi, M. A. El-Sayed, J. T. Khoury, and R. L. Whetten, "Electron Dynamics of Passivated Gold Nanocrystals Probed by Subpicosecond Transient Absorption Spectroscopy," J. Phys. Chem. B **101**, 3713–3719 (1997).

[88] N. Del Fatti, C. Flytzanis, and F. Valle, "Ultrafast induced electronsurface scattering in a confined metallic system," Appl. Phys. B **68**, 433–437 (1999).

[89] V. P. Drachev, U. K. Chettiar, A. V. Kildishev, H.-K. Yuan, W. Cai, and V. M. Shalaev, "The Ag dielectric function in plasmonic metamaterials," Opt. Express **16**, 1186–1195 (2008).

[90] H.-K. Yuan, U. K. Chettiar, W. Cai, A. V. Kildishev, A. Boltasseva, V. P. Drachev, and V. M. Shalaev, "A negative permeability material at red light," Opt. Express **15**, 1076–1083 (2007).

[91] R. Landauer, "Electrical transport properties in inhomogeneous media," Sol. Cells **1**, 297 – 297 (1980).

[92] D. A. G. Bruggeman, "Berechnung verschiedener physikalischer Konstanten von heterogenen Substanzen. I. Dielektrizittskonstanten und Leitfhigkeiten der Mischkrper aus isotropen Substanzen," Ann. Phys. **416**, 636–664 (1935).

[93] L. D. Barron, *Molecular Light Scattering and Optical Activity* (University Press: Cambridge, 1982).

[94] A. D. Buckingham and P. J. Stiles, "Magnetic multipoles and the pseudo-contact chemical shift," Molec. Phys. **24**, 0026–8976 (1972).

[95] R. E. Raab, "Magnetic multipole moments," Molec. Phys. **29**, 1323–1331 (1975).

[96] S. d. Groot and L. Suttorp, *Foundations of electrodynamics* (North-Holland Publishing Company, 1972).

[97] P. Mazur and B. Nijboer, "On the statistical mechanics of matter in an electromagnetic field. I: Derivation of the maxwell equations from electron theory," Physica **19**, 971 – 986 (1953).

[98] J. Schwinger, L. L. Deraad, K. A. Milton, and W. Tsai, *Classical Electrodynamics* (Perseus Books, Reading, 1998).

[99] G. Russakoff, "A derivation of the macroscopic Maxwell equations," Am. J. of Phys. **38**, 1188–1195 (1970).

[100] J. Petschulat, A. Chipouline, A. Tünnermann, T. Pertsch, C. Menzel, C. Rockstuhl, T. Paul, and F. Lederer, "Simple and versatile analytical approach for planar metamaterials," Phys. Rev. B **82**, 075 102 (2010).

[101] J. Petschulat, J. Yang, C. Menzel, C. Rockstuhl, A. Chipouline, P. Lalanne, A. Tuennermann, F. Lederer, and T. Pertsch, "Understanding the electric and magnetic response of isolated metaatoms by means of a multipolar field decomposition," Opt. Express **18**, 14 454–14 466 (2010).

[102] E. Pshenay-Severin, A. Chipouline, J. Petschulat, U. Hübner, A. Tünnermann, and T. Pertsch, "Optical properties of metamaterials based on asymmetric double-wirestructures," Opt. Express **19**, 6269–6283 (2011).

[103] D. Smith, S. Schultz, P. Markos, and C. Soukoulis, "Determination of effective permittivity and permeability of metamaterials from reflection and transmission coefficients," Phys. Rev. B **65**, 195 104 (2002).

[104] T. Tamir, *Guided Wave Optoelectronics* (Springer, 1990), 2 edn.

[105] C. Menzel, C. Rockstuhl, T. Paul, F. Lederer, and T. Pertsch, "Retrieving effective parameters for metamaterials at oblique incidence," Phys. Rev. B **77**, 195 328 (2008).

[106] G. Dolling, M. Wegener, and S. Linden, "Realization of a three-functional-layer negative-index photonic metamaterial," Opt. Lett. **32**, 551–553 (2007).

[107] S. Zhang, W. Fan, K. J. Malloy, S. Brueck, N. C. Panoiu, and R. M. Osgood, "Near-infrared double negative metamaterials," Opt. Express **13**, 4922–4930 (2005).

[108] A. Andryieuski, C. Menzel, C. Rockstuhl, R. Malureanu, F. Lederer, and A. Lavrinenko, "Homogenization of resonant chiral metamaterials," Phys. Rev. B **82**, 235 107 (2010).

[109] N. A. Mortensen, M. Yan, O. Sigmund, and O. Breinbjerg, "On the unambiguous determination of effective optical properties of periodic metamaterials: a one-dimensional case study," J. Europ. Opt. Soc. Rap. Public. **5**, 10 010 (2010).

[110] C. Rockstuhl, T. Paul, F. Lederer, T. Pertsch, T. Zentgraf, T. P. Meyrath, and H. Giessen, "Transition from thin-film to bulk properties of metamaterials," Phys. Rev. B **77**, 035 126 (2008).

[111] C. Helgert, C. Rockstuhl, C. Etrich, C. Menzel, E.-B. Kley, A. Tünnermann, F. Lederer, and T. Pertsch, "Effective properties of amorphous metamaterials," Phys. Rev. B **79**, 233 107 (2009).

[112] M. G. Moharam and T. K. Gaylord, "Coupled-wave analysis of reflection gratings," Appl. Opt. **20**, 240–244 (1981).

[113] P. Lalanne and G. M. Morris, "Highly improved convergence of the coupled-wave method for TM polarization," J. Opt. Soc. Am. A **13**, 779–784 (1996).

[114] L. Li, "New formulation of the Fourier modal method for crossed surface-relief gratings," J. Opt. Soc. Am. A **14**, 2758–2767 (1997).

[115] A. Taflove and S. Hagness, *Computational Electrodynamics: The Finite-Difference Time-Domain Method* (Artech House, Boston, 2005), 3 edn.

[116] J. Turunnen and F. Wyrowski, *Diffractive Optics* (Akademie Verlag, Berlin, 1997).

[117] W. M. Gang Bao, Lawrence Cowsar, *Mathematical modeling in optical science* (Frontiers in applied mathematics, 2001).

[118] T. Koschny, P. Markoš, D. R. Smith, and C. M. Soukoulis, "Resonant and antiresonant frequency dependence of the effective parameters of metamaterials," Phys. Rev. E **68**, 065 602 (2003).

[119] A. Alù, "Restoring the physical meaning of metamaterial constitutive parameters," Phys. Rev. B **83**, 081 102 (2011).

[120] M. Kafesaki, I. Tsiapa, N. Katsarakis, T. Koschny, C. M. Soukoulis, and E. N. Economou, "Left-handed metamaterials: The fishnet structure and its variations," Phys. Rev. B **75**, 235 114 (2007).

[121] U. Hübner, J. Petschulat, E. Pshenay-Severin, A. Chipouline, T. Pertsch, C. Rockstuhl, and F. Lederer, "Negative-index materials: Two approaches for nanofabricated metamaterials," Microelectron. Eng. **86**, 1138 – 1141 (2009).

[122] C. Helgert, C. Menzel, C. Rockstuhl, E. Pshenay-Severin, E.-B. Kley, A. Chipouline, A. Tünnermann, F. Lederer, and T. Pertsch, "Polarization-independent negative-index metamaterial in the near infrared," Opt. Lett. **34**, 704–706 (2009).

[123] O. Stenzel, *The physics of thin film optical spectra* (Spring, 2005).

[124] R. Swanepoel, "Determination of the thicness and optical-constants of amorphous-silicon," J. Phys. E Sci. Instrum. **16**, 1214–1222 (1983).

[125] J. M. del Pozo and L. Díaz, "Method for the determination of optical constants of thin films: dependence on experimental uncertainties," Appl. Opt. **31**, 4474–4481 (1992).

[126] K. Lamprecht, W. Papousek, and G. Leising, "Problem of ambiguity in the determination of optical constants of thin absorbing films from spectroscopic reflectance and transmittance measurements," Appl. Opt. **36**, 6364–6371 (1997).

[127] J. Rodriguez-Fernandez, A. M. Funston, J. Perez-Juste, R. A. Alvarez-Puebla, L. M. Liz-Marzan, and P. Mulvaney, "The effect of surface roughness on the plasmonic response of individual sub-micron gold spheres," Phys. Chem. Chem. Phys. **11**, 5909–5914 (2009).

[128] A. Trügler, J.-C. Tinguely, J. R. Krenn, A. Hohenau, and U. Hohenester, "Influence of surface roughness on the optical properties of plasmonic nanoparticles," Phys. Rev. B **83**, 081 412 (2011).

[129] E. Pshenay-Severin, U. Hübner, C. Menzel, C. Helgert, A. Chipouline, C. Rockstuhl, A. Tünnermann, F. Lederer, and T. Pertsch, "Double-element metamaterial with negative index at near-infrared wavelengths," Opt. Lett. **34**, 1678–1680 (2009).

[130] R. M. A. Azzam and N. M. Bashara, *Ellipsometry and Polarized Light* (North Holland, 1988).

[131] W. J. Anderson and W. N. Hansen, "Optical characterization of thin films," J. Opt. Soc. Am. **67**, 1051–1058 (1977).

[132] L. Lepetit, G. Chériaux, and M. Joffre, "Linear techniques of phase measurement by femtosecond spectral interferometry for applications in spectroscopy," J. Opt. Soc. Am. B **12**, 2467–2474 (1995).

[133] R. Marks, *Handbook of Fourier analysis and its applications* (Oxford University Press, 2009).

[134] L. Duvillaret, F. Garet, and J.-L. Coutaz, "A reliable method for extraction of material parameters in terahertz time-domain spectroscopy," IEEE J. Sel. Top. Quant. **2**, 739 –746 (1996).

[135] M. Francon and S. Mallick, *Polarization interferometers: applications in microscopy and macroscopy* (Wiley-Interscience, New York,, 1971).

[136] E. Pshenay-Severin, F. Setzpfandt, C. Helgert, U. Hübner, C. Menzel, A. Chipouline, C. Rockstuhl, A. Tünnermann, F. Lederer, and T. Pertsch, "Experimental determination of the dispersion relation of light in metamaterials by white-light interferometry," J. Opt. Soc. Am. B **27**, 660–666 (2010).

[137] G. Genty, S. Coen, and J. M. Dudley, "Fiber supercontinuum sources," J. Opt. Soc. Am. B **24**, 1771–1785 (2007).

[138] A. Pashkin, M. Kempa, H. Nemec, F. Kadlec, and P. Kuzel, "Phase-sensitive time-domain terahertz reflection spectroscopy," Rev. Sci. Instr. **74**, 4711–4717 (2003).

[139] M. Falkner, *Methods for characterization of effective parameters of nanostructured optical materials*, Diploma thesis, Friedrich-Schiller-Universität Jena (2010).

[140] C. Dorrer, N. Belabas, J.-P. Likforman, and M. Joffre, "Spectral resolution and sampling issues in Fourier-transform spectral interferometry," J. Opt. Soc. Am. B **17**, 1795–1802 (2000).

[141] S. Maeda, G. Thyagarajan, and P. N. Schatz, "Absolute Infrared Intensity Measurements in Thin Films. II. Solids Deposited on Halide Plates," J. Chem. Phys. **39**, 3474–3481 (1963).

[142] J. S. Plaskett and P. N. Schatz, "On the Robinson and Price (Kramers-Kronig) Method of Interpreting Reflection Data Taken through a Transparent Window," J. Chem. Phys. **38**, 612–617 (1963).

[143] K. Kozima, W. Suëtaka, and P. N. Schatz, "Optical Constants of Thin Films by a Kramers-Kronig Method," J. Opt. Soc. Am. **56**, 181–184 (1966).

[144] K. Yamamoto and H. Ishida, "Kramers-Kronig analysis applied to reflection-absorption spectroscopy," Vib. Spectrosc. **15**, 27 – 36 (1997).

[145] R. H. Young, "Validity of the Kramers-Kronig transformation used in reflection spectroscopy," J. Opt. Soc. Am. **67**, 520–522 (1977).

[146] A. Minovich, D. N. Neshev, D. A. Powell, and Y. S. Kivshar, "Influence of the substrate on negative index fishnet metamaterials," Optics Communications **283**, 4770 – 4774 (2010).

[147] D. A. Powell and Y. S. Kivshar, "Substrate-induced bianisotropy in metamaterials," **97**, 091 106 (2010).

[148] D. R. Smith, D. C. Vier, T. Koschny, and C. M. Soukoulis, "Electromagnetic parameter retrieval from inhomogeneous metamaterials," Phys. Rev. E **71**, 036 617 (2005).

[149] L. D. Landau and E. M. Lifshitz, *Mechanics*, Vol. 1 (Butterworth-Heinemann, 1976), 3 edn.

[150] C. Menzel, C. Helgert, C. Rockstuhl, E.-B. Kley, A. Tünnermann, T. Pertsch, and F. Lederer, "Asymmetric Transmission of Linearly Polarized Light at Optical Metamaterials," Phys. Rev. Lett. **104**, 253 902 (2010).

[151] C. Menzel, C. Rockstuhl, and F. Lederer, "Advanced Jones calculus for the classification of periodic metamaterials," Phys. Rev. A **82**, 053 811 (2010).

B. Acknowledgment

This work would have never been possible without several people supporting me during the years of my work. I would like to thank

for the help regarding LaTeX; Falk Eilenberger for sharing his opinion about almost all questions and for proofreading of the work; Reinhard Geiss for help in the laboratory; Matthias Kroll for his advices concerning an uncountable number of issues; Benny Walther for care about the climate in our office and the proofreading of the work.

- Matthias Falkner for patience to be my student; for his enthusiastic work on the development of the interferometric setup and the excellent results; for the automation of almost all electronic devices in the lab.

- Frank Setzpfandt for his being and for supporting me in all highs and lows of my PhD work; for the proofreading of this work and an incredible number of documents especially in German.

- my parents and my brother for faith in me.

- anybody I may have forgotten unintentionally.

C. Curriculum Vitae

Name:	Ekaterina Pshenay-Severin
Date of birth:	18.02.1981
Place of birth:	Leningrad
Nationality:	Russian

EDUCATION

07/1997 - 07/2003	St.-Petersburg State Polytechnical University, Radiophysical Science and Engineering Faculty, Department of Physical Electronics, Laboratory of Holography.

DEGREES

05/2001	Bachelor's degree
	Title of Bachelor's thesis: 'Application of coherent optics methods in medicine'.
05/2003	Master's degree of physics
	Specialization: Physics of medicine technologies
	Title of Master's thesis: 'Synthesis of holographic fan-out elements'.

EMPLOYMENT

09/2003-08/2005	Research assistant at St.-Petersburg State Polytechnical University, Russia.
since 09/2005	Ph.d. student at Friedrich-Schiller-Universität Jena, Germany.

ACHIEVEMENTES

10/2004 - 07/2005	Russian Federation President Scholarship for study abroad: Fraunhofer Institut für Angewandte Optik und Feinmechanik, Jena

D. Publications

Journal publications

- E. Pshenay-Severin, A. Chipouline, J. Petschulat, U. Hübner, A. Tünnermann, and T. Pertsch, "Optical properties of metamaterials based on asymmetric double-wire structures," Opt. Express **19**, 6269–6283 (2011).

- I. Bergmair, B. Dastmalchi, M. Bergmair, A. Saeed, W. Hilber, G. Hesser, C. Helgert, E. Pshenay-Severin, T. Pertsch, E. B. Kley, U. Huebner, N. H. Shen, R. Penciu, M. Kafesaki, C. M. Soukoulis, K. Hingerl, M. Muehlberger, and R. Schoeftner, "Single and multilayer metamaterials fabricated by nanoimprint lithography," Nanotechnology **22**, 325 301 (2011).

- I. Bergmair, M. Muehlberger, K. Hingerl, E. Pshenay-Severin, T. Pertsch, E. B. Kley, H. Schmidt, and R. Schoeftner, "3D materials made of gold using Nanoimprint Lithography," Microelectron. Eng. **87**, 1008 –1010 (2010).

- E. Pshenay-Severin, U. Hübner, C. Menzel, C. Helgert, A. Chipouline, C. Rockstuhl, A. Tünnermann, F. Lederer, and T. Pertsch, "Double-element metamaterial with negative index at near-infrared wavelengths," Opt. Lett. **34**, 1678–1680 (2009).

- U. Hübner, J. Petschulat, E. Pshenay-Severin, A. Chipouline, T. Pertsch, C. Rockstuhl, and F. Lederer, "Negative-index materials: Two approaches for nanofabricated metamaterials," Microelectron. Eng. **86**, 1138 – 1141 (2009).

- C. Helgert, C. Menzel, C. Rockstuhl, E. Pshenay-Severin, E.-B. Kley, A. Chipouline, A. Tünnermann, F. Lederer, and T. Pertsch, "Polarization-independent negative-index metamaterial in the near infrared," Opt. Lett. **34**, 704–706 (2009).

- C. Rockstuhl, T. Zentgraf, E. Pshenay-Severin, J. Petschulat, A. Chipouline, J. Kuhl, T. Pertsch, H. Giessen, and F. Lederer, "The origin of magnetic polarizability in metamaterials at optical frequencies - an electrodynamic approach," Opt. Express **15**, 8871–8883 (2007).

- J. Duparre, P. Schreiber, A. Matthes, E. Pshenay-Severin, A. Brauer, A. Tunnermann, R. Volkel, M. Eisner, and T. Scharf, "Microoptical telescope compound eye," Opt. Express **13**, 889–903 (2005).

Conference proceedings

- F. Setzpfandt, M. Falkner, R. Schiek, F. Eilenberger, E. Pshenay-Severin, and T. Pertsch, "Bandstructure measurements of lithium niobate waveguide arrays," QELS Baltimore, Maryland USA, Digest p. QMD3 (2011).

- E. Pshenay-Severin, A. Chipouline, J. Petschulat, U. Hübner, A. Tünnermann, and T. Pertsch, "Optical properties of metamaterials based on asymmetric double-wire structures," Proc. SPIE **8070**, 80 700P (2011).

- E. Pshenay-Severin, A. Chipouline, J. Petschulat, U. Hübner, F. Eilenberger, F. Setzpfandt, T. Pertsch, and A. Tünnermann, "Magnetic properties of asymmetric double-wire structures," QELS Baltimore, Maryland USA, Digest p. QTuD7 (2011).

- M. Falkner, E. Pshenay-Severin, C. Helgert, and T. Pertsch, "Interferometric method for the characterization of optically active metamaterials," EQEC Munich Germany, Digest p. EJP9 (2011).

- F. Eilenberger, S. Minardi, E. Pshenay-Severin, Y. Kartashov, A. Szameit, U. Roepke, J. Kobelke, K. Schuster, L. Torner, S. Nolte, F. Lederer, A. Tünnermann, and T. Pertsch, "Observation of nonlinear Light Bullets in waveguide arrays," QELS Baltimore, Maryland USA, Digest p. QMD5 (2011).

- J. Petschulat, A. Chipouline, E. Pshenay-Severin, A. Tünnermann, T. Pertsch, C. Menzel, C. Rockstuhl, T. Paul, and F. Lederer, "Analytical modelling of linear and nonlinear properties of metamaterials based on multipole expansion," Proc. SPIE **7353**, 73 530D (2009).

- C. Helgert, C. Menzel, C. Rockstuhl, E. Pshenay-Severin, J. Üpping, E.-B. Kley, F. Lederer, and T. Pertsch, "Measuring Angular Dependent Effective Properties of Metamaterials," IQEC Baltimore, Maryland USA, Digest p. JThF2 (2009).

- C. Rockstuhl, C. Menzel, T. Paul, C. Helgert, E. Pshenay-Severin, J. Petschulat, A. Chipouline, T. Pertsch, and F. Lederer, "Bulk properties of metamaterials," Proc. SPIE **6987**, 69 871O (2008).

- C. Rockstuhl, E. Pshenay-Severin, J. Petschulat, T. Pertsch, F. Lederer, T. Zentgraf, T. P. Meyrath, and H. Giessen, "Nanoaperture Based Metamaterials," Photonic Metamaterials: From Random to Periodic, Digest p. TuB16 (2007).

- E. Pshenay-Severin, F. Garwe, J. Petschulat, C. Rockstuhl, U. Hübner, C. Helgert, E.-B. Kley, T. Pertsch, A. Tünnermann, and F. Lederer, "A double cell metamaterial for independent tuning of the magnetic and electric response," IQEC Munich Germany, Digest p. JSII4 (2007).

- J. Dorfmüller, C. Rockstuhl, T. Zentgraf, E. Pshenay-Severin, C. Etrich, J. Kuhl, R. Vogelgesang, K. Kern, H. Giessen, T. Pertsch, and F. Lederer, "Near-field Investigation of Split-Ring-Resonator Eigenmodes," NanoMeta Seefeld, Austria, Digest (2007).

- F. Garwe, C. Rockstuhl, U. Hübner, E. Pshenay-Severin, A. Chipouline, U. Bauerschäfer, T. Pertsch, and F. Lederer, "Engineering resonances and losses in negative index metamaterials," NanoMeta Seefeld, Austria, Digest (2007).

- C. Rockstuhl, T. Zentgraf, E. Pshenay-Severin, C. Etrich, A. Chipouline, J. Kuhl, H. Giessen, T. Pertsch, and F. Lederer, "Plasmonic Eigenmodes of Split-Ring-Resonators at Optical Frequencies," NanoMeta Seefeld, Austria, Digest (2007).

- C. Rockstuhl, T. Scharf, E. Pshenay-Severin, J. Petschulat, A. Chipouline, T. Pertsch, and F. Lederer, "Meta-Meta-Materials a bottom-up approach for magnetic resonances in the visible," NanoMeta Seefeld, Austria, Digest (2007).

- E. Pshenay-Severin, C. Chen, T. Pertsch, M. Augustin, A. Chipouline, and A. Tünnermann, "Photonic Crystal Lens for Photonic Crystal Waveguide Coupling," CLEO Long Beach, California USA, Digest p. CThK3 (2006).

- E. A. Pshenay-Severin and S. N. Gulyaev, "Holographic fan-out elements synthesized by the repeated recording process," Proc. SPIE **5400**, 170 (2004).

Conference contributions

- (oral) <u>Falk Eilenberger</u>, S. Minardi, E. Pshenay-Severin, Y. Kartashov, A. Szameit, U. Roepke, J. Kobelke, K. Schuster, L. Torner, S. Nolte, F. Lederer, A. Tünnermann, and T. Pertsch, "Observation of nonlinear Light Bullets in waveguide arrays," Quantum Electronics and Laser Science Conference, Baltimore USA, May 1 (2011).

- (poster) <u>Matthias Falkner</u>, E. Pshenay-Severin, C. Helgert, and T. Pertsch, "Interferometric method for the characterization of optically active metamaterials," CLEO Europe and EQEC Conference, Munich Germany, May 22 (2011).

- (oral) E. Pshenay-Severin, F. Setzpfandt, C. Helgert, U. Hübner, C. Menzel, C. Rockstuhl, A. T'unnerman, F. Lederer, and <u>T. Pertsch</u>, "Direct experimental optical characterization of metamaterials," META2010, Cairo Egypt (2010).

- (oral) <u>E. Pshenay-Severin</u>, A. Chipouline, J. Petschulat, U. Hübner, F. Eilenberger, F. Setzpfandt, T. Pertsch, and A. Tünnermann, "Magnetic properties of asymmetric double-wire structures," Quantum Electronics and Laser Science Conference, Baltimore, May 1 (2011).

- (oral) <u>E. Pshenay-Severin</u>, A. Chipouline, J. Petschulat, U. Hübner, A. Tünnermann, and T. Pertsch, "Optical properties of metamaterials based on asymmetric double-wire structures," Days on diffraction, St.-Petersburg Russia, May 30 (2011).

- (oral) <u>Frank Setzpfandt</u>, M. Falkner, R. Schiek, F. Eilenberger, E. Pshenay-Severin, and T. Pertsch, "Bandstructure measurements of lithium niobate waveguide arrays," Quantum Electronics and Laser Science Conference, Baltimore, May 1 (2011).

- (oral) <u>Christian Helgert</u>, C. Menzel, C. Rockstuhl, E. Pshenay-Severin, J. üpping, E.-B. Kley, F. Lederer, and T. Pertsch, "Measuring Angular Dependent Effective Properties of Metamaterials," Lasers and Electro-Optics/International Quantum Electronics Conference, Baltimore USA, May 31 (2009).

- (poster) <u>J. Petschulat</u>, A. Chipouline, E. Pshenay-Severin, A. Tünnermann, T. Pertsch, C. Menzel, C. Rockstuhl, T. Paul, and F. Lederer, "Analytical modelling of linear and nonlinear properties of metamaterials based on multipole expansion," NanoMeta, Seefeld Austria, January 2 (2009).

- (oral) <u>C. Rockstuhl</u>, C. Menzel, T. Paul, C. Helgert, E. Pshenay-Severin, J. Petschulat, A. Chipouline, T. Pertsch, and F. Lederer, "Bulk properties of metamaterials," Metamaterials III, Pamplona Spain, September 21 (2008).

- (oral) <u>E. Pshenay-Severin</u>, U. Hübner, J. Petschulat, C. Rockstuhl, T. Pertsch, F. Lederer, and A. Tünnermann, "Double elements metamaterial with negative refractive index at infrared wavelength," META2008, NATO advanced research workshop, Marrakesh Morocco (2008).

- (oral) <u>C. Rockstuhl</u>, T. Scharf, E. Pshenay-Severin, J. Petschulat, A. Chipouline, T. Pertsch, and F. Lederer, "Meta-Meta-Materials a bottom-up approach for magnetic resonances in the visible," NanoMeta, Seefeld Austria, January 2 (2007).

- (oral) <u>C. Rockstuhl</u>, T. Zentgraf, E. Pshenay-Severin, C. Etrich, A. Chipouline, J. Kuhl, H. Giessen, T. Pertsch, and F. Lederer, "Plasmonic Eigenmodes of Split-Ring-Resonators at Optical Frequencies," NanoMeta, Seefeld Austria, January 2 (2007).

- (poster) <u>J. Dorfmüller</u>, C. Rockstuhl, T. Zentgraf, E. Pshenay-Severin, C. Etrich, J. Kuhl, R. Vogelgesang, K. Kern, H. Giessen, T. Pertsch, and F. Lederer, "Near-field Investigation of Split-Ring-Resonator Eigenmodes," NanoMeta, Seefeld Austria, January 2 (2007).

- (oral) <u>T. Pertsch</u>, F. Garwe, C. Rockstuhl, U. Hübner, C. Etrich, C. Menzel, E. Pshenay-Severin, A. Shipulin, J. Petschulat, A. Tünnermann, and F. Lederer, "Impact of Plasmonic Resonances for Negative Index Materials," Symposium on Progress in Electromagnetics Research, Beijing China, March 26 (2007).

- (poster) Carsten Rockstuhl, E. Pshenay-Severin, <u>Jörg Petschulat</u>, T. Pertsch, F. Lederer, T. Zentgraf, T. P. Meyrath, and H. Giessen, "Nanoaperture Based Metamaterials," Photonic Metamaterials: From Random to Periodic Digest, Jackson Hole USA, June 4 (2007).

- (oral) F. Garwe, <u>C. Rockstuhl</u>, U. Hübner, E. Pshenay-Severin, A. Chipouline, U. Bauerschäfer, T. Pertsch, and F. Lederer, "Engineering resonances and losses in negative index metamaterials," NanoMeta, Seefeld Austria, January 2 (2007).

- (oral) E. Pshenay-Severin, C. Chen, T. Pertsch, M. Augustin, <u>A. Chipouline</u>, and A. Tünnermann, "Photonic Crystal Lens for Photonic Crystal Waveguide Coupling," Lasers and Electro-Optics/Quantum Electronics and Laser Science Conference, Long Beach California, May 21 (2006).

- (oral) <u>E. A. Pshenay-Severin</u> and S. N. Gulyaev, "Holographic fan-out elements synthesized by the repeated recording process," Seventh International Workshop on Nondestructive Testing and Computer Simulations in Science and Engineering, St.-Petersburg Russia, March 20 (2004).

Ehrenwörtliche Erklärung

Ich erkläre hiermit ehrenwörtlich, dass ich die vorliegende Arbeit selbständig, ohne unzulässige Hilfe Dritter und ohne Benutzung anderer als der hier genannten Hilfsmittel und Literatur angefertigt habe. Die aus anderen Quellen direkt oder indirekt übernommenen Daten und Konzepte sind unter Angabe der Quellen gekennzeichnet. Die Arbeit wurde bisher weder in In- noch im Ausland in gleicher oder ähnlicher Form einer anderen Prüfungsbehörde vorgelegt. Die geltende Promotionsordnung der Physikalisch - Astronomischen Fakultät ist mir bekannt. Ich versichere ehernwörtlich, dass ich nach bestem Wissen die reine Wahrheit gesagt und nichts verschwiegen habe.

Jena, 19.09.2011   Ekaterina Pshenay-Severin